Design of a High Performance Soft X-Ray Emission Spectrometer for the REIXS Beamline at the Canadian Light Source

A Thesis Submitted to the
College of Graduate Studies and Research
in Partial Fulfillment of the Requirements
for the degree of Master of Science
in the Department of Physics and Engineering Physics
University of Saskatchewan
Saskatoon

By
David Muir

Permission to Use

In presenting this thesis in partial fulfilment of the requirements for a Postgraduate degree from the University of Saskatchewan, I agree that the Libraries of this University may make it freely available for inspection. I further agree that permission for copying of this thesis in any manner, in whole or in part, for scholarly purposes may be granted by the professor or professors who supervised my thesis work or, in their absence, by the Head of the Department or the Dean of the College in which my thesis work was done. It is understood that any copying or publication or use of this thesis or parts thereof for financial gain shall not be allowed without my written permission. It is also understood that due recognition shall be given to me and to the University of Saskatchewan in any scholarly use which may be made of any material in my thesis.

Requests for permission to copy or to make other use of material in this thesis in whole or part should be addressed to:

Head of the Department of Physics and Engineering Physics
116 Science Place
University of Saskatchewan
Saskatoon, Saskatchewan
Canada
S7N 5E2

Abstract

The optical design of a soft X-ray (90-1100 eV) emission spectrometer for the Resonant Elastic and Inelastic X-ray Scattering (REIXS) beamline to be implemented at the CLS is presented. An overview of soft X-ray optical theory as it relates to diffraction gratings is given. The initial constraints and the process that led to this design are outlined. Techniques and software tools that were developed, using ray-tracing and diffraction grating efficiency calculations, are discussed. The analysis completed with these tools to compare existing soft X-ray emission spectrometer designs is presented. Based on this analysis, a new design with superior performance for this application is proposed and reviewed. This design employs Rowland circle geometry to achieve a resolving power in excess of 2,500 in the range of interest. In addition, a novel design is proposed for a larger extremely high resolution spectrometer which will provide resolving powers exceeding 10,000 throughout the higher end of this range. A review is given of research into the components, manufacturing techniques and tolerances that will be required to produce this spectrometer.

Acknowledgements

I would like to gratefully acknowledge the support and guidance of my supervisors, Dr. Alexander Moewes and Dr. Mikhail Yablonskikh. The encouragement, camaraderie and input of all the members of the Beamteam has been greatly appreciated. I would like to give special thanks to Mark Boots, whose contribution to this project was significant and invaluable.

I would also like to acknowledge the input of Dr. Giacomo Ghiringhelli who was willing to share his experience and the lessons he learned in designing his own soft X-ray emission spectrometer.

I am grateful to Dr. Doug Degenstein and Dr. George Sofko for the constructive criticism and encouragement that they provided in the writing of this document. Their input in the final revision of this document was indispensable.

On a personal note, I would like to thank my family for their support, both financial and moral, which has been without limits throughout my life. Finally, I would like to especially thank Jennifer, who has been by my side throughout the course of this degree. This course was made a great deal easier by her loving company and persistent encouragement.

This project was supported by funding from the National Science and Engineering Research Council (NSERC) and the Canada Research Chair program.

Contents

List of Tables

List of Figures

List of Abbreviations

ALS	Advanced Light Source
BL	Beamline
CLS	Canadian Light Source
CCD	Charge Coupled Device
XHEG	Extremely High Energy Grating
HRHEG	High Resolution High Energy Grating
HRMEG	High Resolution Medium Energy Grating
IMP	Impurity Grating
LEG	Low Energy Grating
MEG	Medium Energy Grating
MCP	Multi Channel Plate
RAE	Resistive Anode Encoder
RP	Resolving Power
REIXS	Resonant Elastic ad Inelastic X-ray Scattering
UHV	Ultra High Vacuum
VLS	Variable Line Space
XAS	X-ray Absorption Spectroscopy
XES	X-ray Emission Spectroscopy

Part I

Background

Chapter 1

Introduction

Material science is a rapidly growing field of research, driven by the demand for novel materials for applications in electronics, optics, biosciences and other fields. The ability to synthesize, characterize and model the behavior of materials is key to their application in these fields. To this end, X-ray Absorption and Emission Spectroscopy (XAS and XES) are invaluable tools for probing the electronic structure of matter. The demand for greater availability and capability of XAS and XES experimental stations is ever increasing as these techniques become more advanced and more widely known. The advent of the CLS as a world class synchrotron has provided a local source for the intense soft X-rays required for these techniques. Our group is positioned to develop a cutting-edge soft X-ray spectrometer to help meet the demand for XES and XAS experimentation. The goal of this project was to select or design an appropriate spectrometer to make our REIXS (Resonant Elastic and Inelastic X-ray Scattering) beamline at the CLS a leader in its field.

1.1 Project Overview

The objective of this project was to develop a powerful X-ray emission spectrometer with optimal efficiency and high resolving power E/ΔE (above 2000) in the energy range 90 - 1100 eV for the recently funded REIXS beamline at the Canadian Light Source. To accomplish this, the first task was to complete a survey of existing commercially available and custom built systems to determine if any of them would meet our needs. There is no standardized method of quantifying the performance of these instruments, making any kind of meaningful comparison of published specifications impractical. As a result, we opted to perform a computational analysis of these systems and implement our own criteria to quantify their performance, allowing for meaningful and impartial comparison. The results of this analysis, as laid out in this document, led to the second phase of the project which was to design a spectrometer with superior performance by developing four key strengths:

1. superior optimization of our design to the specific spectral windows of interest, allowing optimal analysis of materials containing Si ($L_{2,3}$ emission edge, 92 eV), C ($K_{1,2}$ emission edge, 280 eV), N ($K_{1,2}$ emission edge, 400 eV) and O ($K_{1,2}$ emission edge, 525 eV) while maintaining acceptable performance for bound state transitions in lanthanides and transition metals ($M_{3,4}$ & $N_{4,5}$ edges, 600 eV - 1100 eV);

2. a focus on best possible performance instead of a compact, mechanically simple or budget design;

3. a mechanical design allowing for superior alignment and calibration;

4. an optical design using not only ray-traced optical analysis but also analytical diffraction efficiency to allow careful balancing and optimization of all important design parameters simultaneously.

This design philosophy, along with the understanding gained in the process of analyzing existing systems, allowed for the design of an optical system that exceeds the initial goals. The proposed spectrometer design boasts a resolving power of 2500 or greater at all points of interest with good efficiency. An additional efficiency optimized grating was incorporated, which gives the user a choice between high resolution and high efficiency throughout much of the spectral range. A novel design exploiting higher diffraction orders has also been proposed, providing resolving powers in excess of 10,000 through the high end of the spectral range of this design. The optical design has been completed and is presented in this thesis, along with the research, analysis and design process leading to it. Also presented are the preliminary results of research into the selection of suitable components for this spectrometer to ensure its predicted performance is realized.

1.2 Document Layout

This document is divided into three main sections. In this **Background** section, an overview of the project has been given. The remainder of the section is given over to a discussion of the theory behind X-ray optical systems and diffraction spectrometers.

The second section, **Analysis and Design**, discusses the analysis of existing soft

X-ray spectrometers and the knowledge gained from that analysis. The specifications of the new optical design that has been completed for our spectrometer are outlined and an overview of the design process that led to this design is given. The results of an external review of this design conducted by an expert in soft X-ray optics are summarized. Finally, our investigations into the tolerances and sensitivities of the design variables and machining parameters are discussed.

In the final section, **Component Selection and Manufacture**, various grating manufacturing techniques are discussed and their advantages and disadvantages are compared and contrasted. The options for a detector technology are reviewed and compared. Some of the issues that will have to be addressed in completing the mechanical design of the spectrometer are also discussed.

Chapter 2

Theory

2.1 Soft X-Ray Emission Spectroscopy

The purpose of a spectrometer is to analyze the spectral distribution of the radiation (be it visible light, X-rays, infrared, etc) emitted by a source. This information can be used to understand the composition of, and processes taking place within, that source. For the purpose of this thesis, we will consider only soft X-ray spectroscopy, in the range of 90-1100 eV ($\sim$ 1-15 nm). Soft X-rays are well suited to the study of the electronic structure of materials because the energy range of the radiation is matched to the characteristic binding energies of the s and p electrons of many elements. By exciting a sample with radiation of a given energy and monitoring the soft X-rays emitted as the sample relaxes, details of the electronic structure of an element within a system can be revealed. Figure. 2.1 shows such an emission spectra from a sample of Er_2O_3 as measured on beamline 8.0.1 of the Advanced Light Source. This figure demonstrates the need for high resolving powers in soft X-ray spectroscopy. The ALS spectrometer performs exceptionally well around 170 eV where this data was collected (see Section 3.1.2). This allowed for a detailed comparison of the

experimental data to calculated data. Few, if any, spectrometers are able to perform this well at the higher end of the energy range being considered.

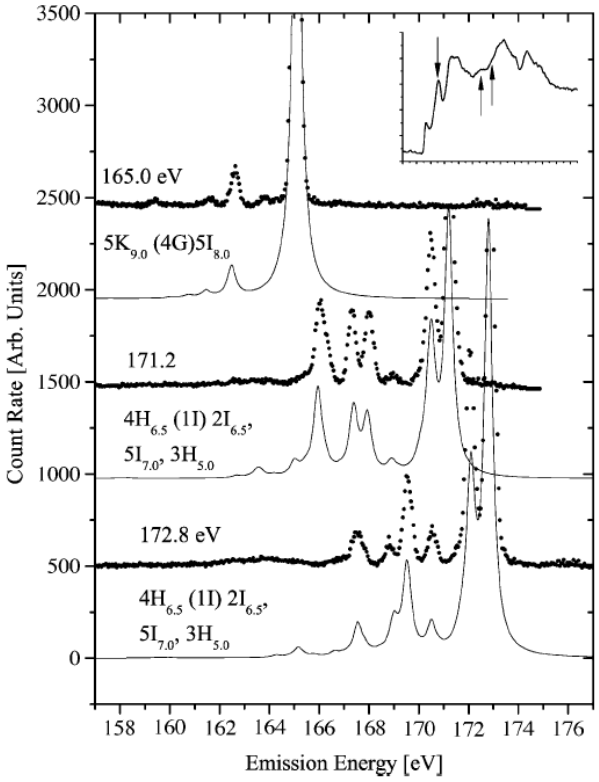

Figure 2.1: An example of a soft X-ray emission spectroscopy data showing selected Resonant Inelastic X-ray Scattering (RIXS) spectra displayed against calculated Raman scattering curves.[1]

The important characteristics of the photons emitted from a sample being studied are their energy (or wavelength) and relative number. A spectrometer provides a way to collect emitted photons, to count them and to determine their energies. The exact method of doing so is determined primarily by the energy range of the photons being studied. These instruments can range in complexity from simple glass prisms to dispersive solid state germanium detector arrays.

For this design, the choice is limited by the fact that, at normal incidence, soft X-rays are quickly absorbed by all materials, even gases. As a result it is necessary to

work in ultra-high vacuum environments and use carefully designed grazing incidence diffraction gratings to reflect and disperse the photons of different energies in different directions. These photons can then be focused onto an area detector to count them and determine their energy based on their spatial position on the detector. The imaging characteristics of such a system can be modeled using geometric optics.

2.2 X-Ray Optical Systems

In designing any optical system, especially one to be operated in the soft X-ray regime, there are a number of complications that must be overcome to create a system that produces a high quality image. In the case on soft X-rays, there are significant difficulties to be overcome to create a system that is capable of producing any image at all. The most significant of these issues and the general approaches used to overcome them are discussed here.

2.2.1 Reflectivity and Grazing Incidence Optics

The most significant challenge in designing optical systems for the X-ray regime is overcoming the extremely low reflectivity of available materials. The efficiency, or fraction of incident photons that are successfully focused onto the detector, can be difficult to maintain at usable levels. At normal incidence soft X-rays are typically absorbed due to the fact that the X-rays are sufficiently energetic to ionize electrons from all materials. This high absorption of soft X-rays that most materials exhibit rules out refractive optics and requires grazing angles be used for reflective optics.

Acceptable efficiency can be achieved by exploiting the fact that, in this energy range, the index of refraction of matter is below that of vacuum (for example, 0.914 for Au at 100 eV and 0.993 for Ni at 400 eV)[2]. This allows for reasonably high reflectance by setting up a total external reflection[3]. This phenomenon is identical to total internal reflection, with the exception of the fact that the vacuum index of refraction is higher than the index of refraction of the medium, resulting in the total reflection taking place external to the medium (in this case, the optical element). Examples of critical angles for common optical element coatings in the soft X-ray region are: $\theta_c \approx 66^\circ$ for Au at 100 eV and $\theta_c \approx 83^\circ$ for Ni at 400 eV. By selecting appropriate materials for coating the optical elements and optimizing the incidence angles, efficient soft X-ray optical systems can be designed using reflective elements.

2.2.2 Optical Aberrations

While grazing incidence optics work well to compensate for the problems associated with low reflectivity, they introduce a new set of problems that must be addressed. Grazing incidence optical elements suffer from increasing optical aberrations as the source and image plane are moved away from the normal of an optical element. Significant astigmatism, coma and spherical aberration[4] are all present in the image formed by a spherical grazing incidence mirror or grating. Fig. 2.2 illustrates these aberrations. Spherical aberration, Fig. 2.2 top, results from the fact that a spherical optical element is not perfectly shaped to focus an incident plane wave to a point. As a result, regions of the optical element at different distances from the optical axis have slightly different focal lengths. Coma, Fig. 2.2 middle, occurs when the source

is not located directly on the optical axis of the element. Rays that are incident on different regions of the optical element will focus to different locations on the focal plane, causing the image to be blurred out along the direction of the incident plane in the characteristic 'carrot' shape shown. Astigmatism, Fig. 2.2 bottom, results when the geometry of the optical element and system cause rays along the meridional plane (the vertical plane in the figure) to focus at different distances than those along the sagittal plane (the horizontal plane in the figure). This results in blurring in one direction or the other, depending on the focal distance chosen.

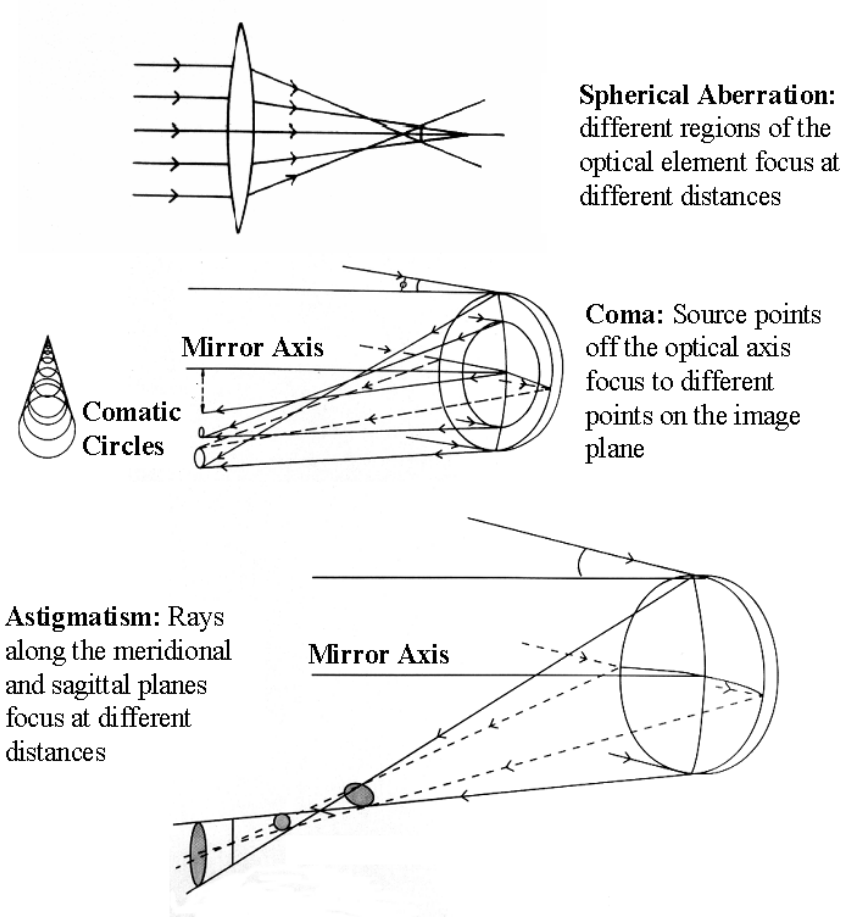

Figure 2.2: Common imaging aberrations[5]

It is possible to correct for some of these aberrations by using aspheric elements,

additional corrective optics or, in the case of gratings, varying the line spacing across the element. These solutions, however, depend strongly on the specific energy of the incident photons, which greatly limits the effective energy range and can result in reduced efficiency. The spherical aberration and astigmatic coma, of greatest significance, can be partially compensated for with image post processing. The remaining aberrations can be reduced through careful design and therefore tolerated[6].

2.2.3 Three Element Spectrometers

Even with grazing incidence optics, the obtainable reflection efficiencies are still well below unity. Because of this, it is necessary to minimize the number of optical components in a system. The standard approach is to use three optical elements, a source or entrance slit, a spherical diffraction grating and an area sensitive X-ray detector. Such a design is illustrated in Fig. 2.3. The source for the spectrometer is either a fluorescing spot on a sample or an entrance slit between the sample and the rest of the spectrometer that allows more rigorous control over the size and position of the source within the optical system. These designs employ spherical diffraction gratings which disperse the incident photons of different energies and focus them to different locations (along a so called focal curve) using only one optical element. Finally, a movable area detector, positioned at the appropriate location along this focal curve, is used to collect a cross-section of the dispersed photons of the desired energy.

Due to the energy dependence of the optical characteristics and materials used to create these diffraction gratings, it is usually necessary to design several interchange-

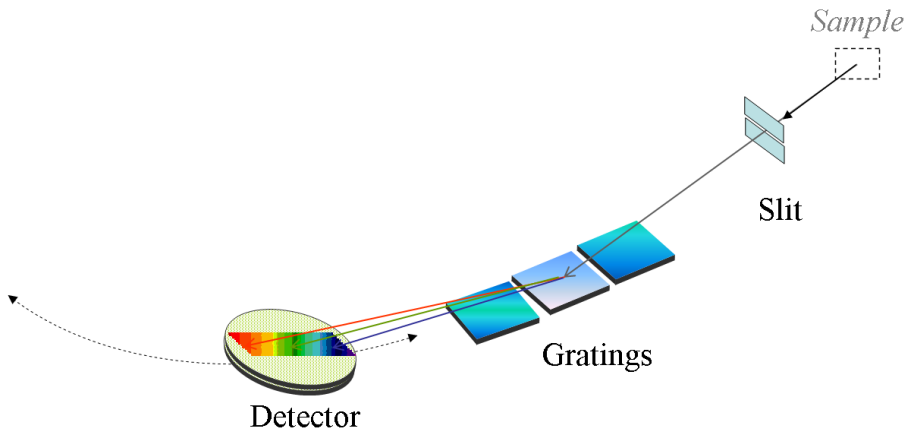

Figure 2.3: A typical selectable grating three-element slit-grating-detector design. The three interchangeable gratings are each designed to operated in different incident energy ranges. They can be translated to place the required grating in the optical path allowing them to share a common entrance slit and detector.

able gratings to cover the energy range of interest. Using multiple interchangeable gratings allows the efficiency and resolving power of a spectrometer to be optimized to multiple energies and allows it to reach the focal point for any given energy with a reasonable amount of detector motion. Each grating is typically optimized for a different energy or range of energies and some type of mechanical system is used to translate the grating appropriate to the desired energy range into the optical path. These three-element, selectable-grating soft X-ray spectrometers are the types of systems that are explored in this thesis.

2.3 Spectrometer Performance Evaluation

There are two key characteristics of soft X-ray spectrometers that define their performance: resolving power and efficiency. The majority of the design parameters of a spectrometer affect both of of these characteristics, and usually in an oppos-

ing manner. Thus, in order to choose or design an effective spectrometer, these characteristics must be considered in unison to ensure an optimally balanced instrument. Our group, building on two existing software simulation tools, developed a software suite designed to calculate these performance characteristics for arbitrary spectrometer designs. These tools allowed us to perform the detailed analysis required to choose or produce a balanced design optimized to meet our needs. These two key characteristics and the simulation techniques developed to calculate them are discussed in the following sections.

2.3.1 Resolving Power

The resolving power of a spectrometer is a measure of how finely it is able to distinguish between photons of different energies. Resolution, ΔE_{res}, is a measure of smallest amount by which two energies can differ and still be distinguished (or *resolved*) by a given spectrometer. Various criteria exist for defining when two energies are resolvable. Our group developed techniques and software tools which allowed us to determine the resolving power of various spectrometer designs using one consistent resolving criterion. This facilitated meaningful comparison of the performance of the different systems. The resolving criteria developed and used for this project are described in a later section.

Higher energy photons can be more difficult to finely resolve and finer resolution is more important at lower energies than higher energies. This makes it practical to define the resolving power as an energy normalized resolution, $E/\Delta E_{res}$, typically as an inverse with ΔE_{res} in the denominator. In this way the resolving power has more

intuitive values since superior resolutions result in greater resolving power values.

The resolution can be equally well defined in terms of the incident wavelength, λ. Due to the differential nature of resolution, resolving power is defined in the same way, as $\lambda/\Delta\lambda_{res}$, because:

$$\begin{aligned} E =& \frac{hc}{\lambda} \\ dE =& \frac{hc}{\lambda^2} d\lambda \\ \Delta E =& \frac{hc}{\lambda^2} \Delta\lambda \end{aligned} \tag{2.1}$$

then

$$\frac{E}{\Delta E_{res}} = \frac{\frac{hc}{\lambda}}{\frac{hc}{\lambda^2}\Delta\lambda_{res}} = \frac{\lambda}{\Delta\lambda_{res}}$$

where h is Planck's constant and c is the speed of light. This highlights another advantage of using resolving power instead of resolution, namely energy and wavelength can be used interchangeably in the discussion of resolving power, with less potential for confusion.

Of the two key characteristics, resolving power is the most difficult to deal with, mainly because it is not a clearly defined quantity. There are numerous criteria for defining the resolvable energy difference, ΔE_{res}, and numerous methods of applying these criteria to determine the resolving power of a system. As a result it can be extremely difficult to compare the performance of two spectrometers based on their published or advertised characteristics. Even if the exact criteria used to determine

the resolving powers of different spectrometers is known, it may be impossible to convert these values to a common system for comparison. In order to examine and compare the resolving power of various spectrometer designs in a meaningful way, a uniform method of quantitatively analyzing their performance was required.

There are numerous analytical formulae for describing the resolution or resolving power of an optical system. Among the simplest of these formulae are those based on diffraction limited resolving power criteria such as the Taylor or Rayleigh criteria. For example, the Rayleigh criteria requires that the bright fringe of one energy line falls on the first dark fringe of the second energy line for the lines to be considered resolvable. For a grating, this leads to the result[7]:

$$E/\Delta E_{res} = N\ell k \tag{2.2}$$

where $N\ell$ is the total number of grooves of the grating and k is the diffraction order. Typical soft X-ray spectrometer gratings may range from 4,000-24,000 lines/cm and would be approximately 4 cm long. In the first diffraction order Eqn. 2.2 gives resolving powers of 16,000-96,000. Such resolving powers are completely unobtainable, as this formula does not take into account any of the optical properties or characteristics of the components or their limitations and unavoidable imperfections.

As another simple example, we can consider the dispersion that a given optical configuration will produce. Dispersion can be expressed in two ways, spatial dispersion and angular dispersion. The angular dispersion is the rate at which the diffraction angle changes with energy. Spatial dispersion is the physical spacing *on*

the focal plane of two lines of different energies. The spatial dispersion is determined by the angular dispersion and the distance between the grating and the focal plane (focal length). Fig. 2.4 shows how spatial and angular dispersion are related. Greater dispersion results in more separation between spectral features and a higher resolving power.

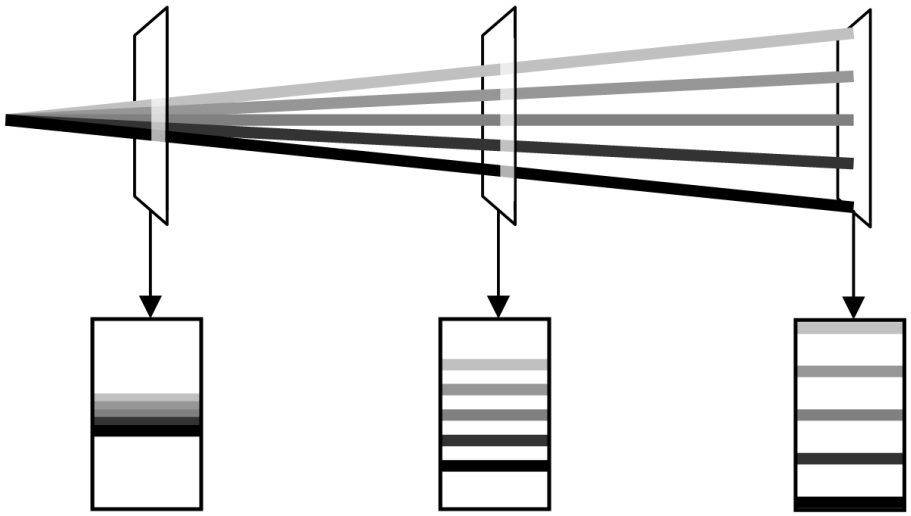

Figure 2.4: Shown are lines of five different energies that have been dispersed by a grating and detectors at three different distances from the grating. The angular separation of two given energies is determined by the optical layout and characteristics of the grating. The spatial dispersion, as seen by the detector, is a function of both the angular dispersion and distance from the grating to the detector (typically the focal length).

The standard expression for angular dispersion can be found from the grating equation, which will be derived in Section 2.4, (Eqn. 2.9):

$$Nk\lambda = \sin\alpha + \sin\beta$$

where N is the grating line density, k is the diffraction order, λ is the incident wavelength, α is the incidence angle and β is the diffraction angle. By differentiating

the grating equation implicitly with respect to λ, assuming α to be constant[8] we attain:

$$\begin{aligned}\left(\frac{d}{d\lambda}\right)_\alpha Nk\lambda &= \left(\frac{d}{d\lambda}\right)_\alpha (\sin\alpha + \sin\beta) \\ Nk &= \cos\beta \left(\frac{d\beta}{d\lambda}\right)_\alpha \\ \left(\frac{d\beta}{d\lambda}\right)_\alpha &= \frac{Nk}{\cos\beta} \end{aligned} \tag{2.3}$$

This equation describes how quickly the diffraction angle changes with respect to the wavelength. For small values of $d\lambda$, the actual spatial dispersion at the detector can be found by multiplying Eqn. 2.3 by the grating-detector distance (focal length, r'), which could be used to establish a simplistic resolving criteria by comparing this value to the spatial resolution of the detector (e.g. the pixel size for a CCD detector). This approach would fail to take into account many important factors such as the dimensions of the source, the focal characteristics of the grating and the optical aberrations in the system. Analytical formulae that attempt to take these and other factors into account do exist but are limited in their application and vary in accuracy. Section 5.3 on page 92 discusses one such approach. Ray-tracing, a more powerful, flexible and labor-intensive calculation technique, which is described in the next section, was chosen for the calculations performed for this project.

Ray-tracing and SHADOW

For the greatest possible flexibility and accuracy, analytical formulae were neglected in favor of a software ray-tracing package that can simulate the image that would

appear on a detector based on a geometric description of the optical layout of a spectrometer. This was done using the well-known SHADOW ray-tracing package[9] from the University of Wisconsin-Madison - Center for NanoTechnology. SHADOW uses a Monte Carlo based ray-tracing engine to simulate a user-defined optical system.

Broadly defined, Monte Carlo based calculations simulate a system by randomly sampling a model of the system of interest in some fashion[10]. In the case of Monte Carlo based ray-tracers, such as SHADOW, the optical system is sampled by randomly generating ray vectors at a source and following their progression through the system by applying the laws of geometric optics to each ray-surface interaction[11]. This can be contrasted to image-based ray-tracers which generate one or more rays for each pixel of the output image and trace their paths backward through the system to determine what objects and sources contribute to that pixel.

SHADOW calculations are performed by defining the optical system within a virtual coordinate system and by describing the physical characteristics of each optical element. For the three-element (slit, grating, detector) optical systems considered in this project, optical layouts are similar to that shown in Fig 2.5. The characteristics of a source or entrance slit, a diffraction grating and a detector plane are input into the software for it to use in completing the ray-trace calculations.

The end result of such a calculation is a plot, like that shown in Fig. 2.6, of all the locations that the traced rays originating from the entrance slit intercept the detector plane after being diffracted and focused by the grating. The curvature of the lines in this figure is due to the aberrations present in a grazing incidence optical system. This is one of the many factors that ray-tracing simulations include and an

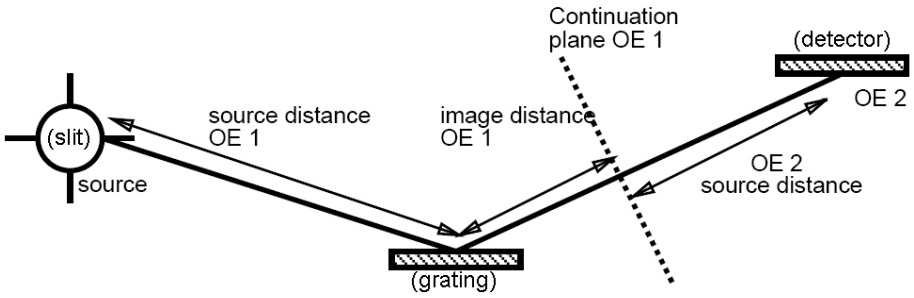

Figure 2.5: The optical layout used within the SHADOW ray-tracing package. The characteristics of the source and optical elements (OE) are defined by the user. SHADOW then traces the rays from the source through each element to determine the ray configuration at the following continuation plane. This continuation plane is then used as the source for the next element, and the process is repeated.

analytical formulae cannot easily account for.

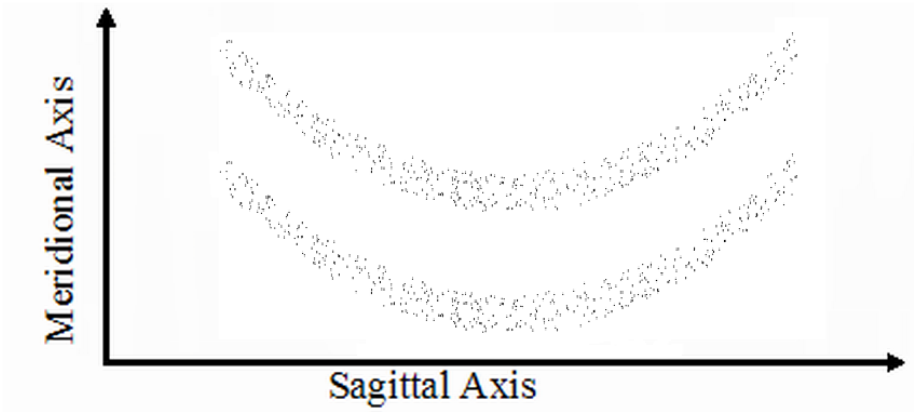

Figure 2.6: Image formed at the detector showing spatial distribution of 1,000 rays of two different discrete energies after being traced through the spectrometer. The diffraction grating acts to create a separate image on the entrance slit for each discrete energy emitted from it. The two lines seen here are these two images, their curvature is due to aberrations in optical system.

A rectangular source with the dimensions of the entrance slit was used as a source for the purpose of these calculations. Angular dispersion simulated the fact that the actual source would be a spot on a sample behind the slit. Simulations showed that this is computationally identical to using a sample as a source and a slit as an

additional optical element, but more computationally efficient as rays are not wasted impacting on the blades of the entrance slit.

SHADOW has inherent support for spherical diffraction gratings, with both constant and variable line spacing, and requires only a geometric description and line density (value or polynomial coefficients) to simulate their diffractive characteristics.

A virtual screen is placed at the detector position and the results of the ray-trace can be seen by examining the ray positions at this screen (see Fig. 2.6). This information can be used to determine the resolving power of the optical system by analyzing this image in terms of some form of resolving criterion. The resolving criterion used for the calculations presented in this thesis is explained in the next section.

Resolving Criteria

To determine the resolving power of a spectrometer based on a ray-trace calculation, the image of the slit emitting different discrete energies is considered. This image, as it appears at the detector is comprised of multiple dispersed slit images, one for each discrete energy the slit is emitting. The resolving power is determined by considering how the spatial dispersion of these images relates to the energy difference between them. To determine the spatial dispersion, the separation of these slit images (or energy lines) is typically measured peak-to-peak (center-to-center in the case of an image like Fig. 2.7). This measure, however, would neglect the slit size and the effects of optical aberrations in the system that result in spreading of these line widths. In order to factor these aberrations into our resolving criteria, we measured

the edge-to-edge separation of the lines, as shown in Fig. 2.7. The curved image at the detector seen in Fig. 2.7 is the result of the combined effects of spherical aberration and astigmatic coma. For the purpose of measuring the line separation, this curvature can be ignored as it is predictable and is easily corrected by software image post-processing when using a standard two dimensional area detector array.

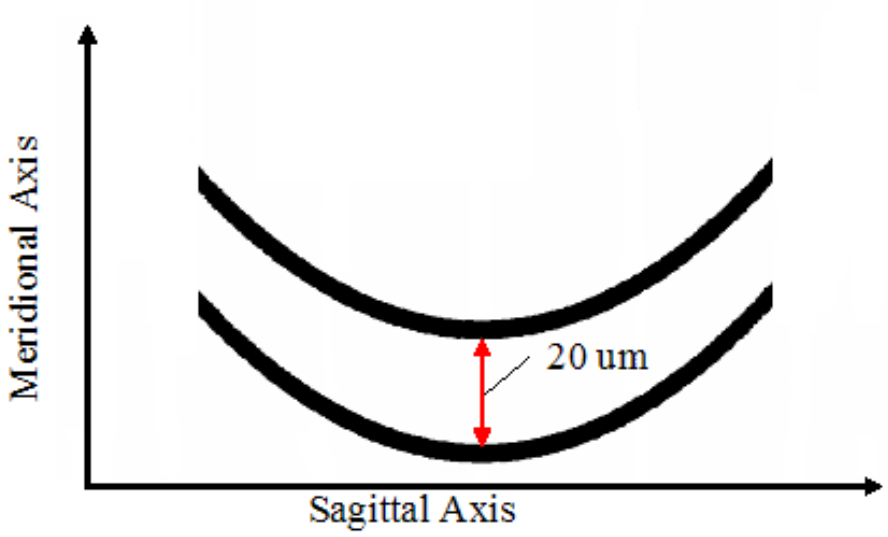

Figure 2.7: Ray-traced image at the detector showing spatial dispersion of 25,000 rays of two different discrete energies. The arrow indicates the requirement established by our resolving criteria for two given energies to be resolvable by a detector with 20 μm pixels.

For the sake of computational efficiency, only the rays arriving in the central region of the image were traced, as this is where the spatial separation was determined. From this image, a histogram like that shown in Fig. 2.8, was created. The actual spatial separation of the two lines was taken from this plot. The spatial separation was defined as the distance between the edges of two peaks at a defined height of 5 counts. This height was used to filter out some of the "noise" on the trailing edge of more aberrated lines, like those seen in the right panel of Fig. 2.8. This allowed

for more reasonable determination of their spacing with much greater accuracy and repeatability.

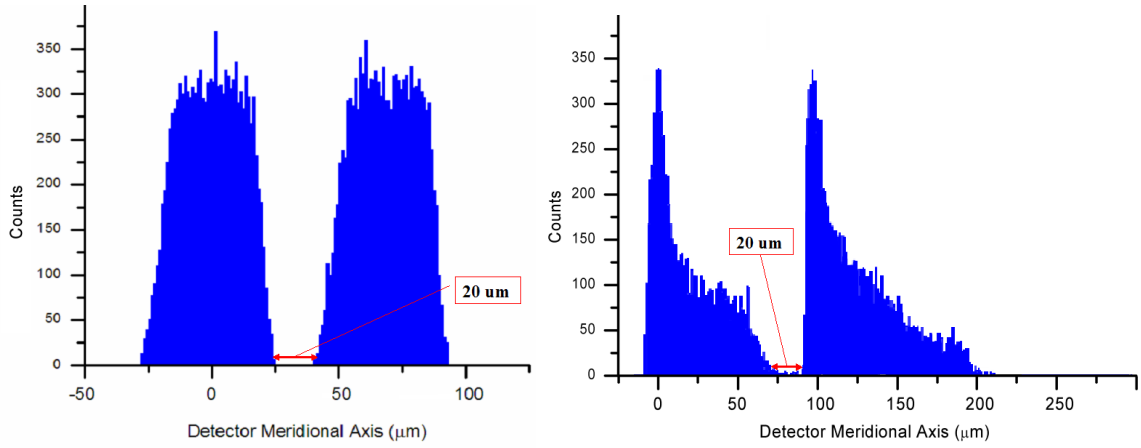

Figure 2.8: To determine the line separation between two energies, the central region of Fig. 2.7 was processed into a histogram and the spacing was measured at a fixed height of five counts. This technique made the measurement of more aberrated images (*left*) significantly more accurate and repeatable.

With a method of defining the spatial separation established, we need to define what is required for two energy lines to be considered to be resolved. The criterion used requires an absolute 20 μm separation, as measured in Fig. 2.8, between images of a 10 μm wide dichromatic entrance slit; i.e. with a 10 μm slit emitting two discrete energies, the resulting lines at the detector have to be 20 μm apart, edge-to-edge, to be considered to be resolved. The two energies emitted by the slit are iteratively adjusted until this condition is met, and their energy difference is then equal to ΔE_{res}. For example, the histogram shown in Fig. 2.8 was created by a slit emitting rays with energies of 95 eV and 95.03 eV. This resulted in an edge-to-edge line separation of 20 μm. These two energies are, therefore, considered to be resolved, giving $\Delta E_{res} = 0.03$ eV. From this we can determine that the spectrometer that

created this image has a resolving power of $E/\Delta E_{res} = 95/0.03 = 3167$ at 95 eV. Each energy focuses at a different location along the focal curve, and therefore has a different focal length. Since the spatial dispersion is a function of the focal length, each energy will therefore have a different resolving power for a given spectrometer configuration.

A 20 μm separation was chosen to represent the size of one pixel on a typical modern CCD detector. To consider how this criteria will affect the resultant data it is useful to consider the contrast of the system. The contrast is defined as[12]:

$$Contrast \equiv \frac{I_{max} - I_{min}}{I_{max} + I_{min}} \tag{2.4}$$

where I_{max} and I_{min} are the counts on adjacent pixels. For example, Fig. 2.9 shows the two extreme cases that can result when the counts from the left panel of Fig. 2.8 are binned into 20 μm detector pixels. The left panel of Fig. 2.9 shows the data from the detector if the required 20 μm separation aligns to a pixel. For this case the contrast is 1.0 according to Eqn. 2.4. For the opposing case, shown right, the 20 μm separation straddles two pixels, which leads to contrasts of 0.63 and 0.79 between the two pixel gap and the left and right features respectively.

The most difficult image to resolve would be that of two square wave pulses separated by 20 μm, as shown in Fig. 2.10. For this case the contrast ratio would be 0.33, still easily high enough to be considered resolvable. Thus our rather rigorous resolving criteria results in a minimum contrast ratio of 33% between two resolvable features.

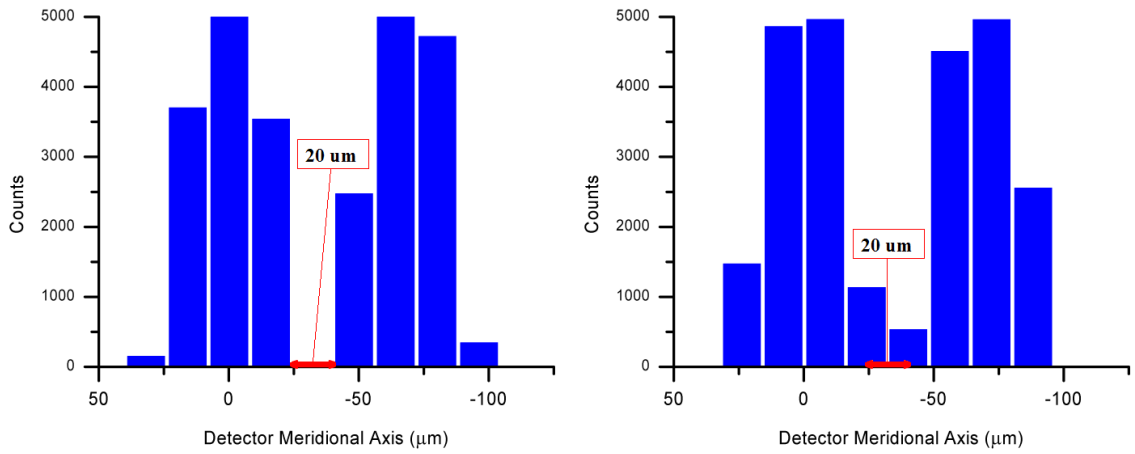

Figure 2.9: Simulated data from a detector with 20 μm pixels. The data shown here is the same two resolvable lines that are shown in the left panel of Fig. 2.8 after binning it into detector pixels. *Left:* Data that results from the required 20 μm spacing aligning to a pixel. *Right:* Data that results from a half pixel offset.

A standard 20 μm detector pixel was used as the basis for the resolving criteria to compare across spectrometers regardless of the pixel size of the detector they were originally built with. This was necessary in order to reveal the true capabilities of the optical systems since it would be a relatively simple task to upgrade a detector. In addition to this, comparisons were performed using the detector resolutions that the various spectrometers were designed with and for an "ideal" 0 μm detector pixel size. All resolving powers given in this paper are calculated as described above for either a 20 μm line separation (pixel size) or for a line separation corresponding to the original pixel size of the design in question. The ideal 0 μm line separation data was calculated to look for any trends that may appear as the detector size decreases. Since no additional information was obtained from these calculations, this data has been omitted from this thesis.

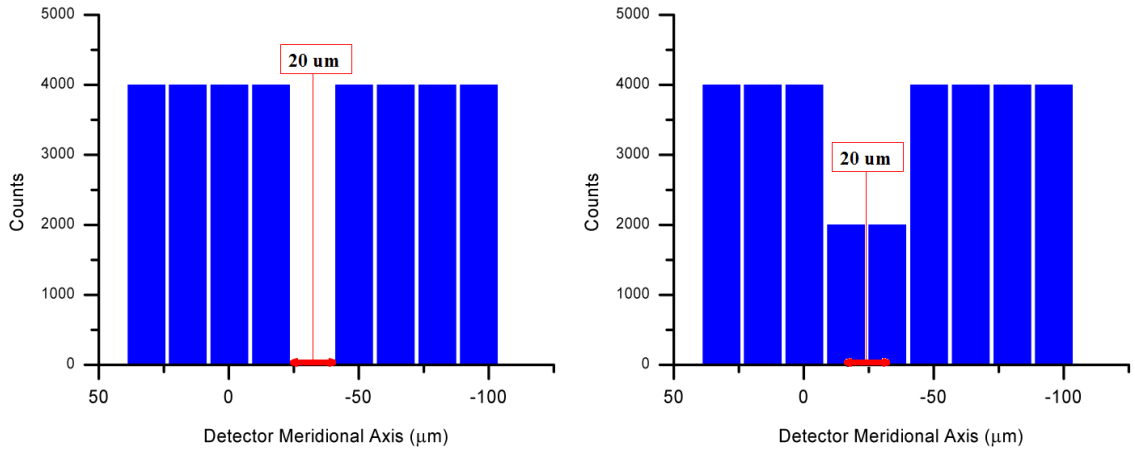

Figure 2.10: Simulated data from a detector with 20 μm pixels. The data shown here is of two resolvable square wave pulses, which results in the lowest contrast of any configuration. *Left:* Data that results from the required 20 μm spacing aligning to a pixel. *Right:* Data that results from a half pixel offset.

2.3.2 Grating Efficiency

The efficiency of a grating, or the fraction of incident photons that it successfully focuses onto the detector, is determined by two distinct factors: geometric efficiency and diffraction efficiency. The first, geometric efficiency, is relatively simple. A larger effective grating area results in more photons being collected. Diffraction efficiency is more complicated, incorporating the optical properties of the diffraction grating and the effects of the photon interactions with the grating material. Each of these components is described in detail in the following sections, along with the approaches used to factor the effects of grating efficiency into the design process of a spectrometer.

Geometric Efficiency

Geometric efficiency is the fraction of available photons that are successfully transmitted through the system as a result of the sizes of the optical elements. The obvious contribution to the geometric efficiency is the area of a grating. The *effective* area of the grating, however, results not only from the size of the grating but also from the incidence angle, α, of incoming photons since higher incidence angles cause the grating to appear smaller to the source, as shown in Fig. 2.11. This means that a lower incidence angle results in higher geometric efficiency. The second factor that effects the geometric efficiency is the source-grating distance, r'. Fig. 2.11 depicts the effects of a longer source-grating distance that reduces the effective collection area, resulting in a lower efficiency.

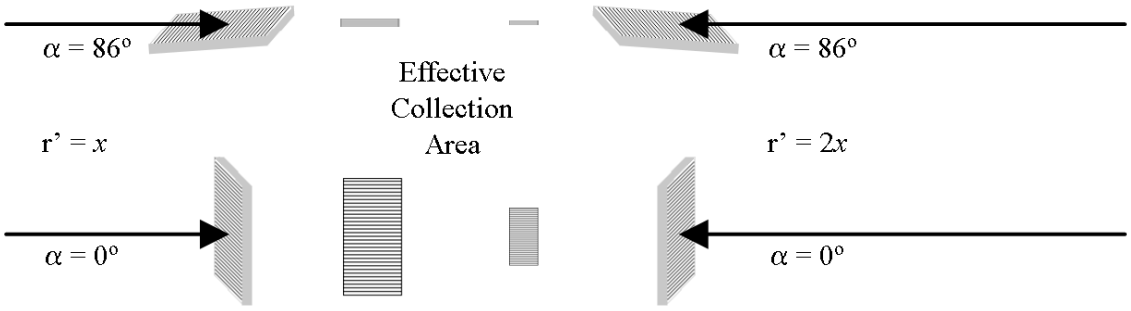

Figure 2.11: The effects of various optical layouts on the geometric efficiency of a grating. The various combinations of two different incidence angles and source-grating distances on the effective area of a grating are shown diagrammatically.

While the geometric efficiency seems like a simple characteristic to control, all the parameters that affect it are intimately tied to other aspects of the performance of the spectrometer. Many of these parameters often more strongly affect these other aspects of performance. As a result, the geometric efficiency is usually of

secondary importance to the design process and its value is determined based on the requirements of other factors influenced by the relevant parameters.

Diffraction Efficiency

The second important contribution to the efficiency of a spectrometer is diffraction efficiency. Diffraction efficiency is the fraction of the photons incident on a grating that are diffracted into the desired diffraction order. The variables that determine the diffraction efficiency of a grating are:

1. Line density (N)
2. Incidence angle (α)
3. Energy or wavelength of photons (E, λ)
4. Groove profile (blaze angle Ψ for saw-tooth profiles, see Fig. 2.13)
5. Grating material (coating)

Variables 1-3 are also critical to the resolving power of the system, and a careful balance is required for optimum performance. The actual behavior of the diffraction efficiency is complex and it can be difficult to predict without rigorous calculations since it is strongly dependent on the interactions between the photons and properties of the grating coating material. Typical grating coatings include gold, nickel and platinum. Fig. 2.12 shows plots of the reflectivity of a 30 nm coating of these materials on a SiO_2 substrate at incidence angles of $\alpha = 86°$ and $\alpha = 88°$. The behavior of the reflectivity across the operating energy range of our spectrometer is shown,

with the coating best suited to each energy range highlighted in bold. Understanding the interaction between incidence angle, grating material and diffraction efficiency is critical to an effective spectrometer design since these parameters provide a large degree of control over the achieved efficiency.

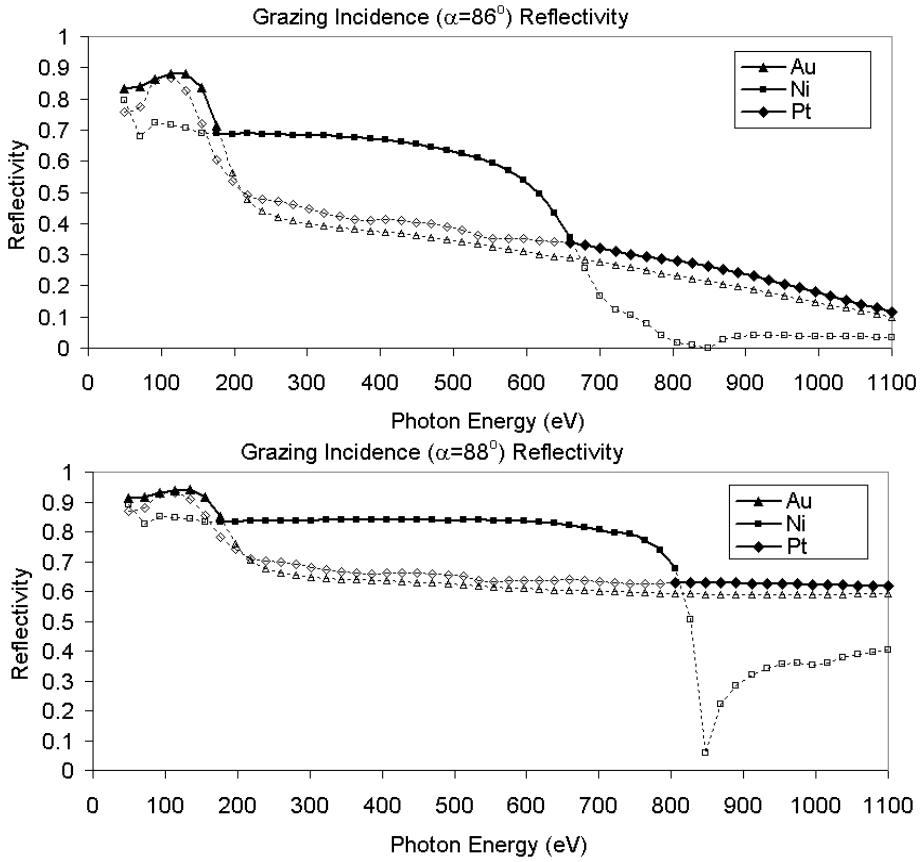

Figure 2.12: The reflectivity of common grating coatings is shown at two different grazing incidence angles[2]. The solid bold portions or each curve indicate the energy ranges for which that coating is superior.

The groove profile or the actual shape of each groove of a grating has a significant effect on the diffraction efficiency[13]. Different grating manufacturing techniques naturally produce different groove profiles and allow for differing levels of control over that profile. There are two significant characteristics that need to be considered in the design of a grating profile: the incidence angle on each groove and the fraction

of dead space on the grating. The shape of the profile determines the incidence angle on each groove. Best efficiency is achieved by controlling the profile to align the specular reflection to the diffraction angle of the energy of interest. If the shape of the profile is not carefully controlled, a significant fraction of incident rays can be lost due to dead spaces where incident rays are reflected by the back sides of grooves at bad angles, leading to either absorption by the grating material or diffraction into the wrong order. Fig. 2.13, top, illustrates how incident rays can be lost to such reflections at bad angles. The optimum groove profile is a saw tooth profile, like that shown in Fig. 2.13 bottom, which results in the maximum illuminated area reflecting light into the desired order. The energy and order of peak efficiency can be controlled by manipulating the blaze angle, Ψ. If the blaze angle is adjusted such that $N = N'$ for a given incident wavelength (λ_{blaze}) then $\alpha = \beta$ and photons of that wavelength are specularly reflected into the desired diffraction order. Details of the various grating production techniques considered, how they affect the profile of a grating and their advantages and disadvantages are discussed in Section 7.2 on page 116.

Grating Efficiency Calculations

An associated project completed by another member of our research group, Mark Boots, yielded effective diffraction efficiency calculation and optimization code based on the Neviere code. The Neviere code is an algorithm based on fundamental electromagnetic theory that calculates the diffraction efficiency of the optical configuration of a grating for any given energy and diffraction order. This software allowed the

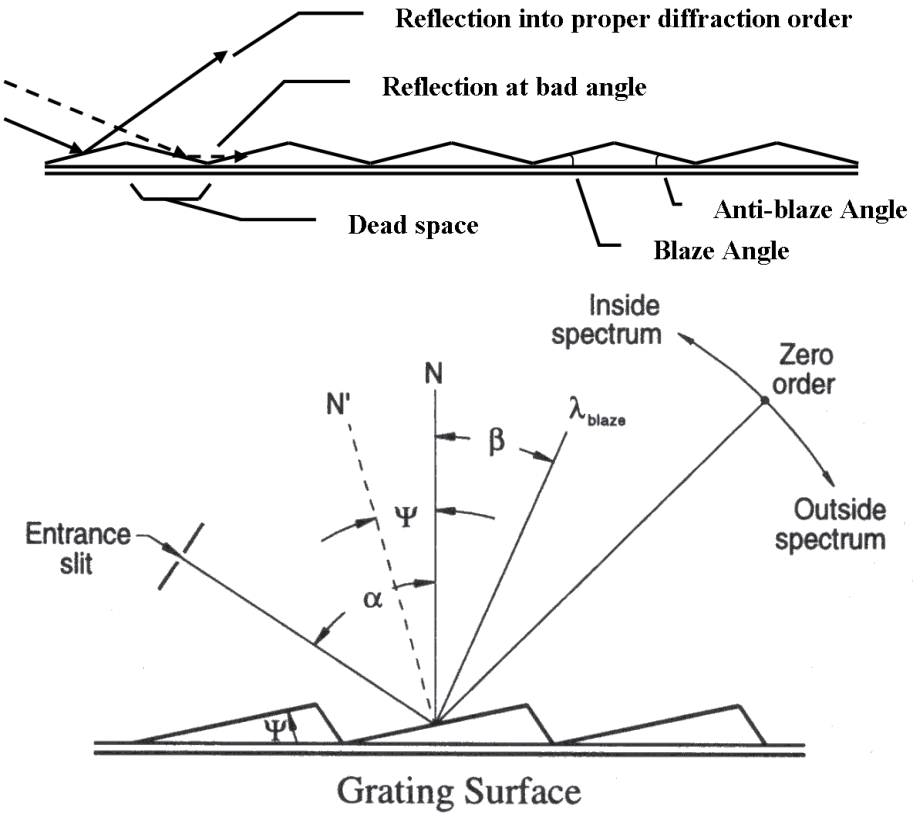

Figure 2.13: **Top:** Dead space that results from improper blaze profiles. **Bottom:** A diagram of a saw-tooth groove profile showing how the blaze angle, Ψ, can align the specular reflection to the diffraction angle of a particular wavelength, λ_{blaze}.[14]

design presented in this paper to achieve a careful balance between diffraction efficiency and resolving power. The results of these diffraction efficiency calculations are presented along with the specifications of the final design in Chapter 4. Few of the published or existing designs by other groups analyzed here or any design that could be found in the literature have included such efficiency calculations. The diffraction efficiency of some existing systems has been calculated for comparison, however exhaustive comparisons of all designs is not possible as sufficient details of the profiles of the gratings used are either rarely published or, in some cases, known.

2.4 Geometric Optics and Fermat's Principle

While the simulation techniques described allow for the behavior of any given optical system to be accurately modeled, they offer no help in determining what the specifications of those systems must be in order to ensure the optical system actually forms an image, not to mention minimizing aberrations. For this we turn to the theory of geometric optics. In studying geometric optics, Fermat's principle sets out the requirements for the formation of an image in an optical system. Fermat's principle, or the principle of least time, states that all paths through an optical system must be extrema for an image to be formed. What this means for a reflective optical element, like the one shown in Fig. 2.14, is that for the optical element to create at point B an image of a source at point A, all the optical paths from A to B via the optical element must be of the same length[14].

If we describe a point on the surface of the optical element as $P(\xi, \omega, \ell)$ (where ξ, ω, ℓ are the surface coordinates, defining a location constrained to the surface of the optical element), then an arbitrary path can be described by an optical path function:

$$F = \overline{AP} + \overline{PB} \tag{2.5}$$

and then satisfying the relations:

$$\frac{\partial F}{\partial \omega} = 0 \qquad \text{and} \qquad \frac{\partial F}{\partial \ell} = 0 \tag{2.6}$$

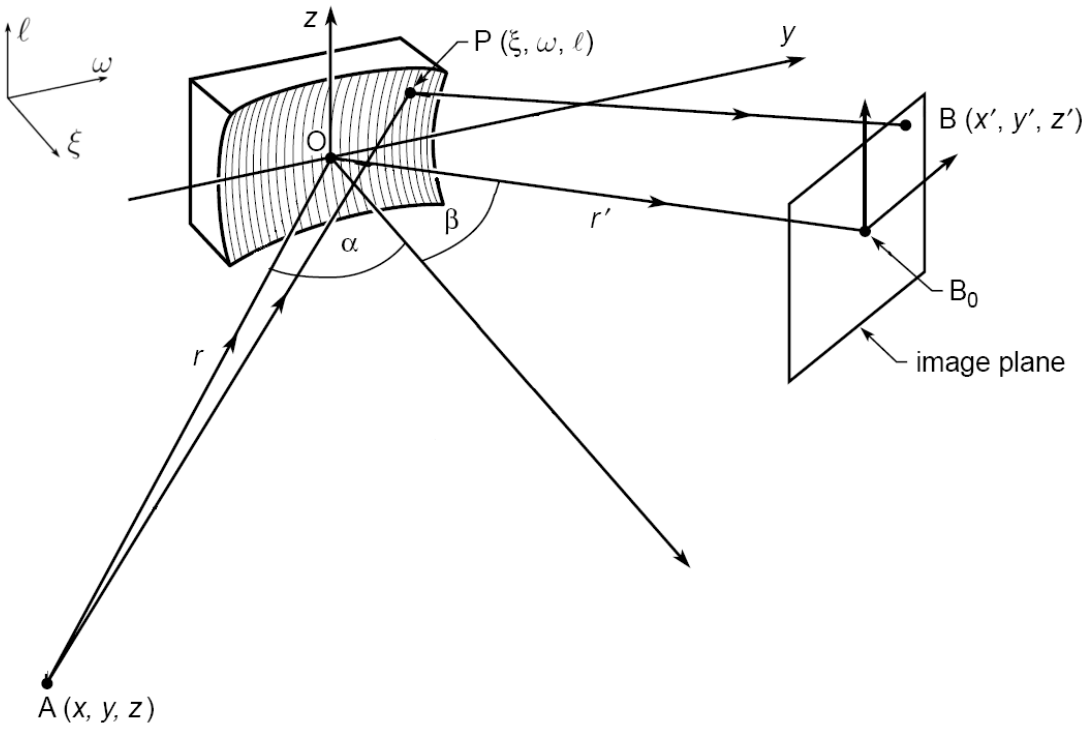

Figure 2.14: shown are all the coordinates used to describe an optical element in the formulation of Fermat's principle. (x, y, z) define the location of the source with respect to the grating origin, O. (x', y', z') define a location on the image plane. (ξ, ω, ℓ) define a location on the surface of the optical element. α and β are the incidence and reflection/diffraction angles. r and r' are the source-grating and focal distances, respectively[14].

will ensure the path length is an extremum and the optics will create an aberration-free image. If the optical element is a grating, then the phase advance resulting from diffraction must be taken into account by adjusting the optical path function as:

$$F = \overline{AP} + \overline{PB} + Nk\lambda\omega \tag{2.7}$$

where N is the grating line density, k is the diffraction order, and λ is the incident wavelength. The same conditions for focus (Eqn. 2.6) apply. By taking ξ to be a function of ω and ℓ, as defined by the geometry of the optical element, the optical

path function can be defined in terms of a polynomial expansion in the coordinate system shown in Fig. 2.14 :

$$F = F_{00} + \omega F_{10} + \ell F_{01} + \omega\ell F_{11} + \frac{1}{2}\omega^2 F_{20} + \frac{1}{2}\ell^2 F_{02} + \frac{1}{2}\omega^3 F_{30} + \frac{1}{2}\omega\ell^2 F_{12} + \ldots \quad (2.8)$$

For the purpose of this derivation we will assume a spherical grating. This assumption is appropriate since the symmetry of spherical optical blanks allows them to be manufactured to significantly higher accuracy than more complicated geometries such as elliptical blanks. As a result, spherical elements are the only viable option. Design considerations of optical element geometry will be discussed in Section 7.1 on page 113. With this assumption in place the expansion in Eqn. 2.8 leads to:

$$\begin{aligned}
F_{00} &= r + r' && (*) \\
F_{10} &= Nk\lambda - (\sin\alpha + \sin\beta) && \text{grating equation} \\
F_{01} &= \frac{-z}{r} + \frac{-z'}{r'} && (*) \\
F_{11} &= -\frac{zsin\alpha}{r^2} - \frac{z'sin\beta}{r'^2} && \\
F_{02} &= \frac{1}{r} + \frac{1}{r'} - \frac{1}{R}(\cos\alpha + \cos\beta) && \text{sagittal focus} \\
F_{20} &= \left(\frac{\cos^2\alpha}{r} - \frac{\cos\alpha}{R}\right) + \left(\frac{\cos^2\beta}{r'} - \frac{\cos\beta}{R}\right) && \text{meridional focus} \\
F_{30} &= \left(\frac{\cos^2\alpha}{r} - \frac{\cos\alpha}{R}\right)\frac{\sin\alpha}{r} + \left(\frac{\cos^2\beta}{r'} - \frac{\cos\beta}{R}\right)\frac{\sin\beta}{r'} && \text{primary coma} \\
F_{12} &= \left(\frac{1}{r} - \frac{\cos\alpha}{R}\right)\frac{\sin\alpha}{r} + \left(\frac{1}{r'} - \frac{\cos\beta}{R}\right)\frac{\sin\beta}{r'} && \text{astigmatic coma}
\end{aligned} \quad (2.9)$$

where R is the radius of curvature of the grating. Differentiating Eqn. 2.8 and setting all the terms equal to zero as called for by Eqn. 2.6 satisfies Fermat's principle. This quickly shows that for an aberration-free image to be formed all of the F_{nm} terms shown in Eqn. 2.9 beyond F_{00} must be identically zero. By setting $F_{10} = 0$ we get the grating equation, which can be solved for the diffraction angle β in terms of α and N, both of which are design parameters.

The most significant terms to minimize are F_{20} and F_{30}. F_{20} is the focus in the dispersion (meridional) direction and is key to the sharp separation of spectral features. F_{30} is the next higher order term and is therefore the most significant source of aberration. Higher order terms have a decreasingly significant impact on image formation.

2.4.1 Rowland Circle Optical Geometry

The optical equations resulting from Eqn. 2.9 are quite complicated and without some form of simplification it would be difficult to design a system with good optical characteristics. One such commonly used simplification for this type of optical system comes about by recognizing the common factors:

$$\left(\frac{\cos^2\alpha}{r} - \frac{\cos\alpha}{R}\right) \qquad \text{and} \qquad \left(\frac{\cos^2\beta}{r'} - \frac{\cos\beta}{R}\right)$$

in F_{20} and F_{30} of Eqn. 2.9 and setting these two factors equal to zero. This results in both F_{20} and F_{30} being identically equal to zero. Setting those two factors to zero and rearranging them leads to the relatively simple equations:

$$\boxed{r = R\cos(\alpha) \quad \text{and} \quad r' = R\cos(\beta)} \qquad \text{The Rowland Circle Condition} \qquad (2.10)$$

These two equations define a set of diffraction angles, β, and focal lengths, r', for an optical system defined by its incidence angle, α, source-grating distance, r, and grating radius, R. Fig. 2.15 shows how this set of angles and lengths (β and r') describes a circular curve, known as the Rowland circle, with a diameter equal to the radius of the grating. This circle, termed the *focal curve*, defines the path in space along which a detector must move in order for Fermat's principle to be fulfilled for any given energy. If all three optical elements (source, grating and detector) lie on this curve, then the Rowland circle condition is met and F_{20} and F_{30} are guaranteed to be minimized. By designing a spectrometer within these constraints, good focal characteristics can be ensured.

The remaining terms in Eqn. 2.9 are not explicitly minimized by the Rowland circle condition. This is generally not an issue but, where it is, steps can be taken to minimize the resulting impact on the resolving power. The F_{00} term is independent of the optical path and does not effect the imaging characteristics. F_{01} simply expresses the mirror symmetry of the image formation and does not result in image aberrations. F_{02} is not minimized in a Rowland circle system, but this is acceptable since it leads only to defocusing perpendicular to the diffraction direction (in the sagittal plane). This does not affect resolving performance because it is the separation of two energy lines in the meridional direction that determines whether or not they can be resolved. F_{12} is also not minimized but it primarily contributes to the curvature of the image,

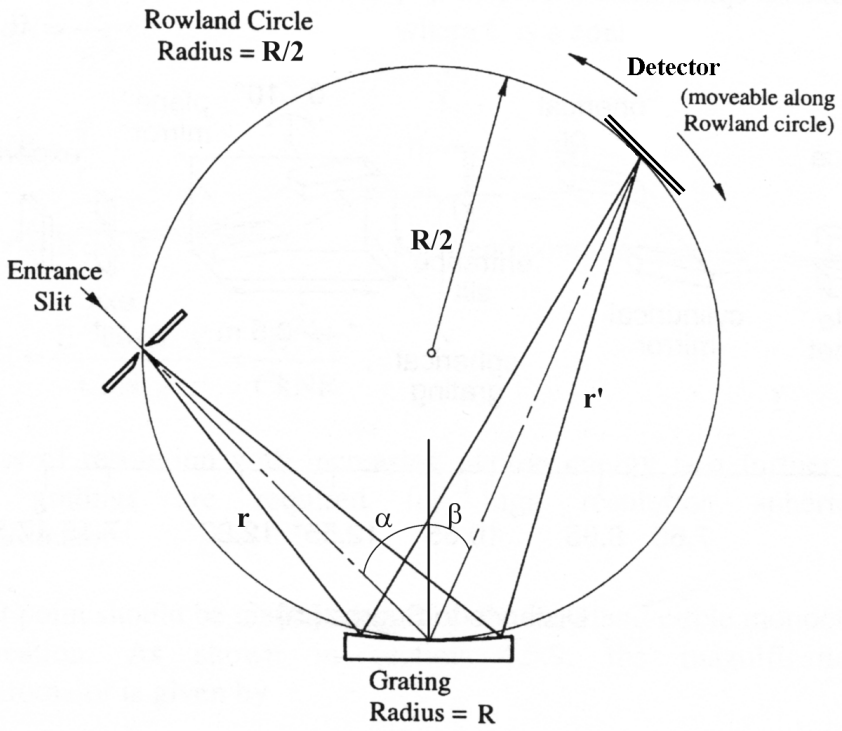

Figure 2.15: Shown is the meridional plane of a Rowland circle spectrometer. The Rowland circle is a path in space on which the grating, source and detector must lie for the Rowland focal condition to be satisfied. Different points along the Rowland circle will satisfy the condition for different energies.

which can be corrected with image post-processing.

2.4.2 Variable Line-Space Gratings

An increasingly common method of exercising additional control over the optical design of a spectrometer is to implement Variable Line-Spaced (VLS) gratings. In these cases the line density across the surface of the grating is not constant, as with standard gratings, but varies with the distance from the grating origin. The variation is typically described by a polynomial as:

$$N(\omega) = N_0 \left(1 + \frac{2b_2}{R}\omega + \frac{3b_3}{R^2}\omega^2 + \frac{4b_4}{R^3}\omega^3 + \ldots\right) \tag{2.11}$$

where N_0 is the line density at the grating origin and the coefficients b_i are design parameters.

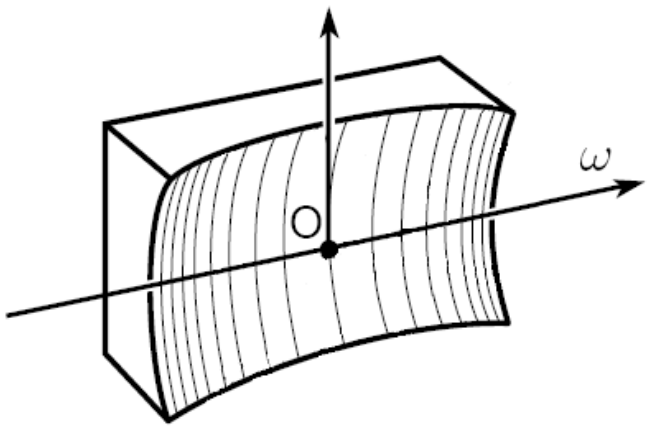

Figure 2.16: The line density varies symmetrically across a VLS grating as a function of ω.

The effect of a spherical VLS grating on an optical system can be determined by replacing $N \rightarrow N(\omega)$ in Eqn. 2.7 and using Eqn. 2.11 to rederive the F_{nm} terms. This yields the same F_{nm} terms as shown in Eqn. 2.9 with the exception of these additional (boxed) terms[15]:

$$\begin{aligned}
F_{02} &= \frac{1}{r} + \frac{1}{r'} - \frac{1}{R}(\cos\alpha + \cos\beta) - \boxed{\frac{N_0 k\lambda}{R}} && \text{sagittal focus} \\
F_{20} &= \left(\frac{\cos^2\alpha}{r} - \frac{\cos\alpha}{R}\right) + \left(\frac{\cos^2\beta}{r'} - \frac{\cos\beta}{R}\right) - \boxed{\frac{2N_0 k\lambda}{R} b_2} && \text{meridional focus} \\
F_{30} &= \left(\frac{\cos^2\alpha}{r} - \frac{\cos\alpha}{R}\right)\frac{\sin\alpha}{r} && \\
&\quad + \left(\frac{\cos^2\beta}{r'} - \frac{\cos\beta}{R}\right)\frac{\sin\beta}{r'} - \boxed{\frac{2N_0 k\lambda}{R^2} b_3} && \text{primary coma}
\end{aligned} \tag{2.12}$$

The grating equation, F_{10}, is unchanged which means that the diffraction angle for any given energy is the same as for a Rowland circle design. No benefit is obtained for the sagittal focus, F_{02}, which is modified but no new controllable variables are introduced. The utility of VLS gratings first appears in the meridional focus, F_{20}, where the focal length becomes subject to modification by the first order line density coefficient, b_2. The effect of modifying b_2 can have on the focal curve of a grating can be seen in Fig. 2.17, which shows the focal curves covering an energy range of 410 eV-1200 eV for a series of example designs with varying b_2 values.

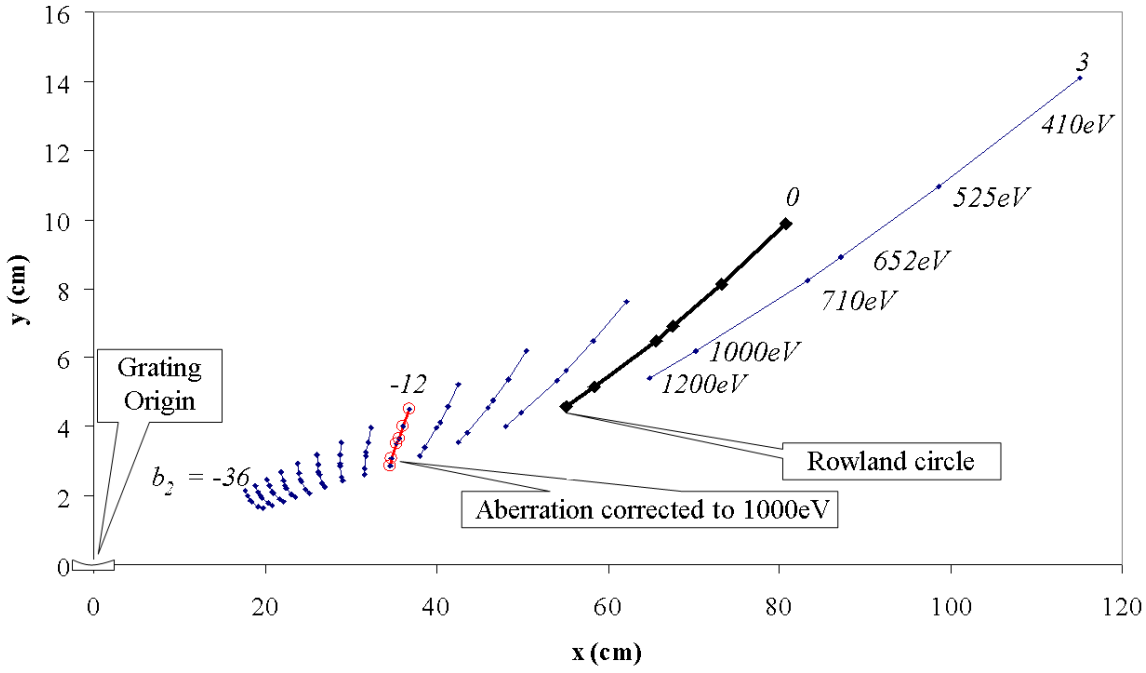

Figure 2.17: The focal curves created by various b_2 parameter values for a prototype VLS grating design. Each focal curve in the diagram covers the energies ranging from 410 eV to 1200 eV. When $b_2 = 0$, the curve lays along the Rowland circle. When $b_2 = -12$, $F_{12} = 0$ at 1000 eV. At this point, $r = r'$ =35 cm.

With $b_2 = 0$, the VLS term vanishes and the focal curve is exactly the Rowland circle. As b_2 moves to higher values, the focal lengths are increased, increasing the

size of the focal curves. This is of very little use since it serves only to introduce additional optical aberrations. As b_2 moves through increasing negative values the focal curve is reduced in size and compacted. With an appropriately chosen negative b_2 value, the focal curve is very nearly linear through a wide range of energies. This creates a compact focal curve, the length of which can be accessed by moving the detector in only one dimension. Such optical designs allow for the design of compact, mechanically simple and potentially less expensive spectrometers with reduced optical aberrations within narrow energy ranges.

The primary coma (F_{30}) is already exactly zero on the Rowland circle. b_3, the second order line density coefficient can, however, be used to minimize this term without being on the Rowland circle. Careful tweaking of b_3 can maintain a minimized F_{30} term while b_2 is adjusted to reduce higher order aberrations such as the astigmatic coma, F_{12}. Fig. 2.18 shows images formed at a detector by an aberration-corrected VLS grating and a Rowland circle grating. Astigmatic coma is responsible for most of the line curvature seen in the image formed by a Rowland circle grating and, as a result, the aberration corrected VLS image is almost completely free of such curvature. This aberration correction is energy dependent, meaning that it is effective for only one specific energy and away from this energy both the astigmatic coma and other aberrations can very quickly become significant.

The focal curve that results from adjusting b_2 to minimize the astigmatic coma (F_{12}) is always symmetric about the grating, i.e. the source-grating distance and the grating-detector distances will be equal ($r = r'$) at the energy for which $F_{12} = 0$. The focal curve that results from an aberration corrected grating is noted in Fig. 2.17.

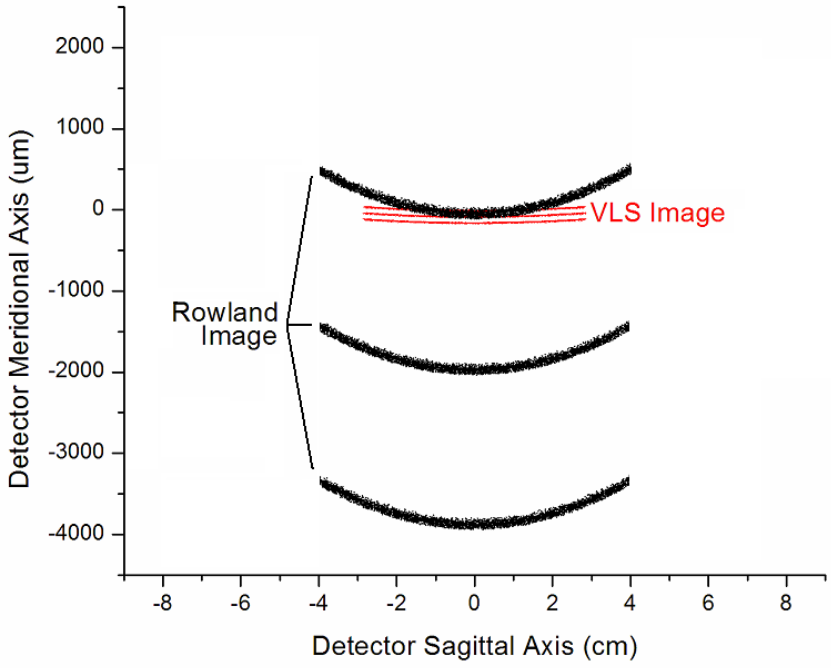

Figure 2.18: Comparison of the image created at the detector by Rowland and VLS systems for a slit emitting three discrete energies near the designed energy. The image formed by the VLS grating is more tightly focused and the aberrations which cause the majority of the line curvature have be corrected. Unfortunately, the reduced spatial dispersion dominates, resulting in a net loss in resolving power.

For the optical system used in that example, aberrations are minimized and $F_{12} = 0$ at 1000 eV when $b_2 = -12$. The 1000 eV focal point on that curve is at exactly 35 cm from the grating origin, the same as the source-grating distance. For all other energies along this focal curve, F_{12} is not minimized and aberration will degrade the resulting image.

This type of aberration correction has other disadvantages as well. The reduction in the focal distances for all energies, as compared to a Rowland circle design, results in reduced spatial energy dispersion causing a significant reduction in resolving power. This is apparent in Fig. 2.17, where the focal curve covering 410 eV-1200 eV

is dramatically shorter for the aberration-corrected curve than for the Rowland circle curve. The dramatic difference in dispersion can be seen in Fig. 2.18, which shows the images formed at the detector of the same three discrete energies emitted from an entrance slit for each type of system.

The other major disadvantage of VLS aberration reduction is that it is highly dependent on the specific photon energy and diffraction order. This results in a further reduction in resolving power, due to increased aberrations, in other orders and everywhere except in the energy region closely surrounding the design energy of the grating[16]. Additionally, VLS gratings are much more complex to design, as the formula shown in Fig. 2.19 demonstrates. This formula, omitted from Eqn. 2.9 due to its length, is required for certain approaches to VLS grating optimization involving higher order aberration reduction. Finally, their complexity increases manufacturing errors, which can be significantly higher than for constant line density gratings, leading to a reduction in performance.

$$
\begin{aligned}
&F_{40} = (1/8(-9\cos(\beta)^4 r^3 R^3 \sigma_0 \cos(\theta)^2 + 4\cos(\beta)^6 r^3 R^3 \sigma_0 \cos(\theta)^2 + 4\cos(\beta)^2 r^3 R^3 \sigma_0 \cos(\theta)^2 \\
&- r^3 r'^3 \sigma_0 \cos(\theta)^2 \cos(\beta) + r^3 r'^2 \sigma_0 \cos(\theta)^2 R + 8m\lambda r^3 r'^3 b_4 \cos(\theta)^2 - 12m\lambda r^3 \\
&\times r'^3 b_3 \sin(\theta)\cos(\theta) - m\lambda r^3 r'^3 \sin(\theta\cos(\theta) - 9\cos(\alpha)^4 R^3 r'^3 \sigma_0 \cos(\theta)^2 + 10\cos(\alpha)^3 \\
&\times R^2 r'^3 \times \sigma_0 \cos(\theta)^2 r - \cos(\alpha)^2 R r'^3 \sigma_0 \cos(\theta)^2 r^2 - r^3 r'^3 \sigma_0 \cos(\theta)^2 \times \cos(\alpha) + r^2 r'^3 \\
&\times \sigma_0 \cos(\theta)^2 R + 10\cos(\beta)^3 r^3 R^2 \times \sigma_0 \cos(\theta)^2 r' - \cos(\beta)^2 r^3 R \sigma_0 \cos(\theta)^2 r'^2 - 4\cos(\beta)^5 r^3 \\
&\times R^2 \sigma_0 \times \cos(\theta)^2 r' + 2m\lambda r^3 r'^3 b_2 - 2m\lambda r^3 r'^3 b_2 \cos(\theta)^2 + 4 \times \cos(\alpha)^2 R^3 r'^3 \\
&\times \sigma_0 \cos(\theta)^2 + 4\cos(\alpha)^6 R^3 r'^3 \sigma_0 \cos(\theta)^2 - 4\cos(\alpha) R^2 r'^3 \sigma_0 \cos(\theta)^2 r - 4\cos(\alpha)^5 R^2 \\
&\times r'^3 \times \sigma_0 \cos(\theta)^2 r - 4\cos(\beta) r^3 R^2 \sigma_0 \cos(\theta)^2 r')/r^3/R^3/r'^3/\sigma_0/\cos(\theta)^2
\end{aligned}
$$

Figure 2.19: This typical VLS design formula was written for a spreadsheet used to minimize a higher order term of the optical path function. This was used in the calculation of the focal curves seen in Fig. 2.17, and illustrates the complexity of these systems.

2.5 Conclusion

The designing of soft X-ray optical systems involves overcoming a number of unique challenges. Because soft X-rays are easily absorbed by materials, grazing incidence diffractive optical systems must be used to manipulate them. These grazing incidence optics lead to strong imaging aberrations that the optical systems must be carefully designed to control. The basic soft X-ray optical spectrometer consists of three optical elements: a source or entrance slit, a spherical diffraction grating, and a movable area detector. Such designs can result in efficient and effective spectrometers.

The performance of a spectrometer can be described by two characteristics: resolving power and efficiency. Each of these characteristics is dependent on a number of design variables and there is significant interrelation between them. As a result, both characteristics need to be considered in unison during the design process in order to ensure optimal overall performance. To achieve this, our group developed a number of software tools that allowed us to simulate, analyze and optimize the overall design of a soft X-ray optical system.

These software simulation tools, while powerful, can be used only to analyze and optimize the performance of a set optical configuration. They can not alone be used to design an optical system with any hope of ending up with a system capable of even forming an image. For this, design formulas derived from geometric optics are needed. From these formulas the design constraints for the standard Rowland circle optical layout can be derived. These constraints provide a relatively simple framework in which a high performance grazing incidence optical system can be

designed.

Rowland circle geometry is not, however, the only approach to designing a grazing incidence spectrometer. The use of variable line spaced gratings to afford more control over the optical system has become increasingly popular in recent years. This added control does come at a cost, as it brings with it strong energy dependance, additional optical aberrations and a net reduction in resolving power. The most commonly used advantage of VLS gratings is that they can create a spectrometer that is much smaller and mechanically simpler. The design priorities of the system must dictate the optimal choice. VLS gratings also have other applications in which they excel such as plane-grating monochromators where the VLS parameters can be used to achieve focus without a concave grating, resulting in a perfectly curvature free image (see Section 7.1).

Part II

Investigation

and

Optical Design

Chapter 3

Investigation of Existing Designs

The first task in this project was to gather and analyze existing spectrometer designs to establish whether they met our needs or could be modified to do so. Five systems were found that operate in the 90-1100 eV energy range we are interested in. Of these, one is a commercially available system and the remainder have been built, or are being built, by other research groups. Two of these designs use gratings with constant line spacing and three use VLS gratings. Resolving power values based on a consistent and rigorous criterion are not available nor are any diffraction efficiencies (calculated or measured), not even for the commercially available system. This necessitated the analysis presented in this chapter.

For each of the 5 systems, complete parameters of their optical layout were obtained, either from the literature or the systems designers. Based on these parameters, the performance of each system was analyzed by modeling it in the SHADOW ray-tracing package. Ray-trace calculations were performed at the specific energies for which our design is to be optimized, in order to quantify the performance of each

system. For each of these calculations the criterion described in section 2.3.1 was applied to determine the resolving power of the system. The resolving power for each grating of each spectrometer was calculated and plotted at various energies to create resolving power performance curves. In order to make sense of the large quantity of data that resulted from the analysis of the spectrometers considered, a number of plots were produced (Fig. 3.1, 3.2 and 3.3). The most revealing of these are shown and discussed below.

The first set of three plots, Fig. 3.1, shows the performance of the various spectrometers as they were designed, including the effects of detector resolution. As described in section 2.3.1, this means that the edges of two spectral lines, as they appear at the detector, are said to be resolved if they are separated by the width of one detector pixel. Each of these three plots shows the performance of each spectrometer at a different common emission edges of interest (Si ($L_{2,3}$ (92 eV), N K_1 (400 eV), Ni $L_{2,3}$ (852 eV)). Each plot shows the gratings for each spectrometer that are able to reach the specified emission edge within the mechanical limits of the design of the spectrometer. As a result, some spectrometers have multiple resolving power curves shown, each for a different grating. To reveal the behavior of each grating over the energy range in which it was designed to operate, the accessible energy range of each grating is shown, not just the performance at the specific emission edge of the plot.

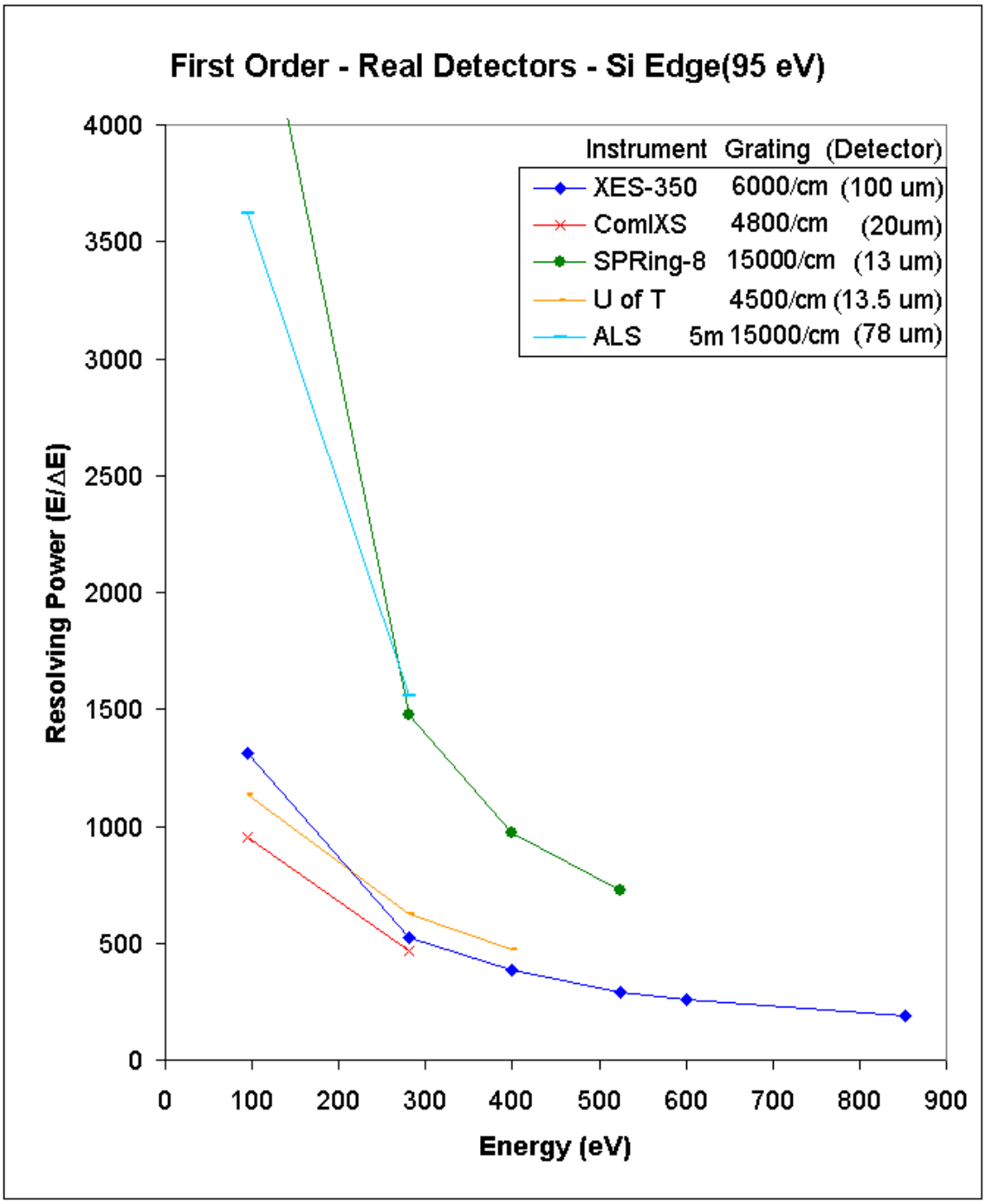

Figure 3.1: Comparison of spectrometer resolving power performance of designs with their original detectors. Capabilities of each system are shown at the Si $L_{2,3}$ emission edge. The legend specifies the spectrometer, grating (size and/or line density) with the detector pixel size in parentheses.

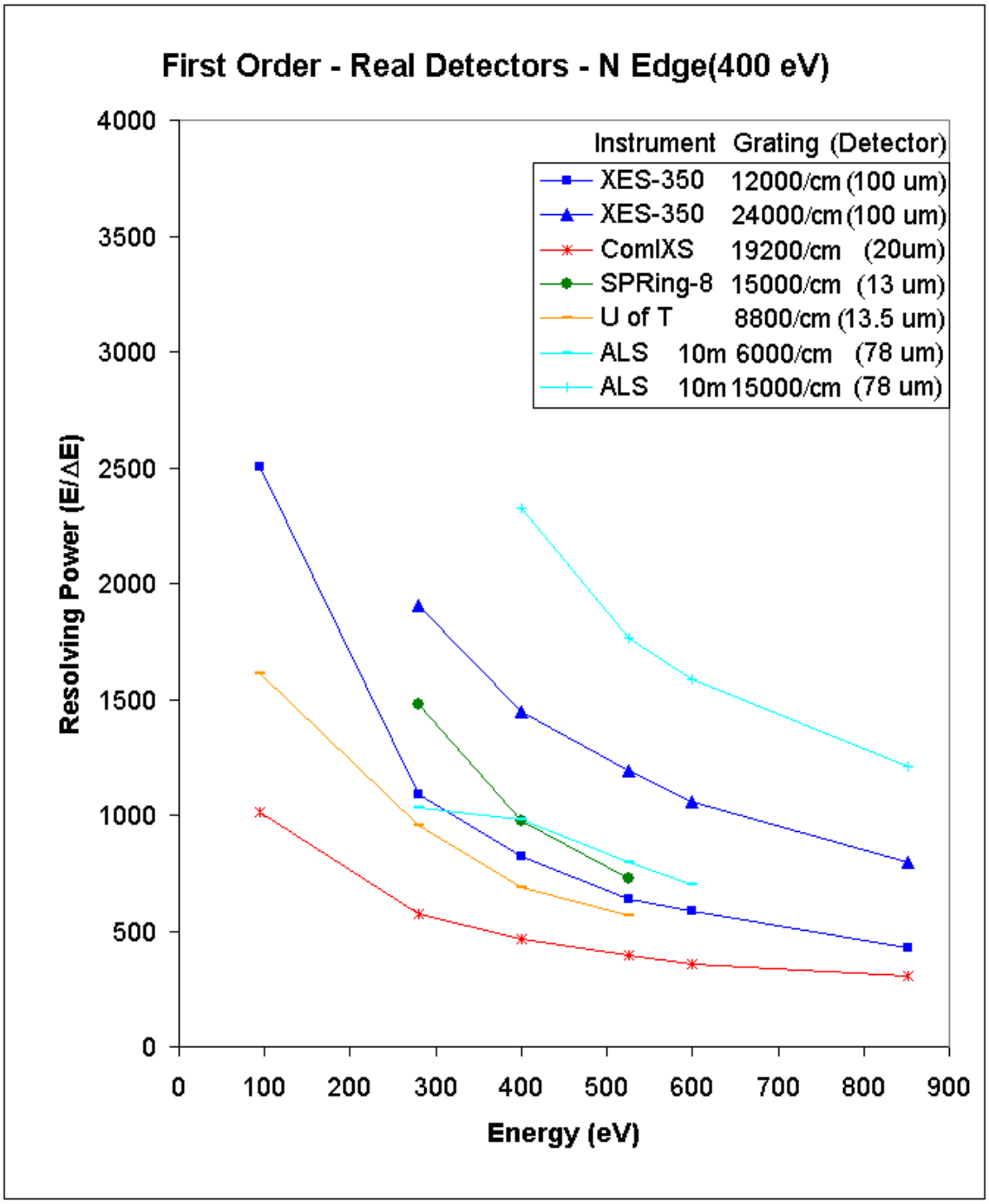

Figure 3.1 ***(cont.)*****:** Comparison of resolving power performance of spectrometer designs with their original detectors. Capabilities of each system are shown at the N K_1 emission edge. The legend specifies the spectrometer, grating (size and/or line density) with the detector pixel size in parentheses.

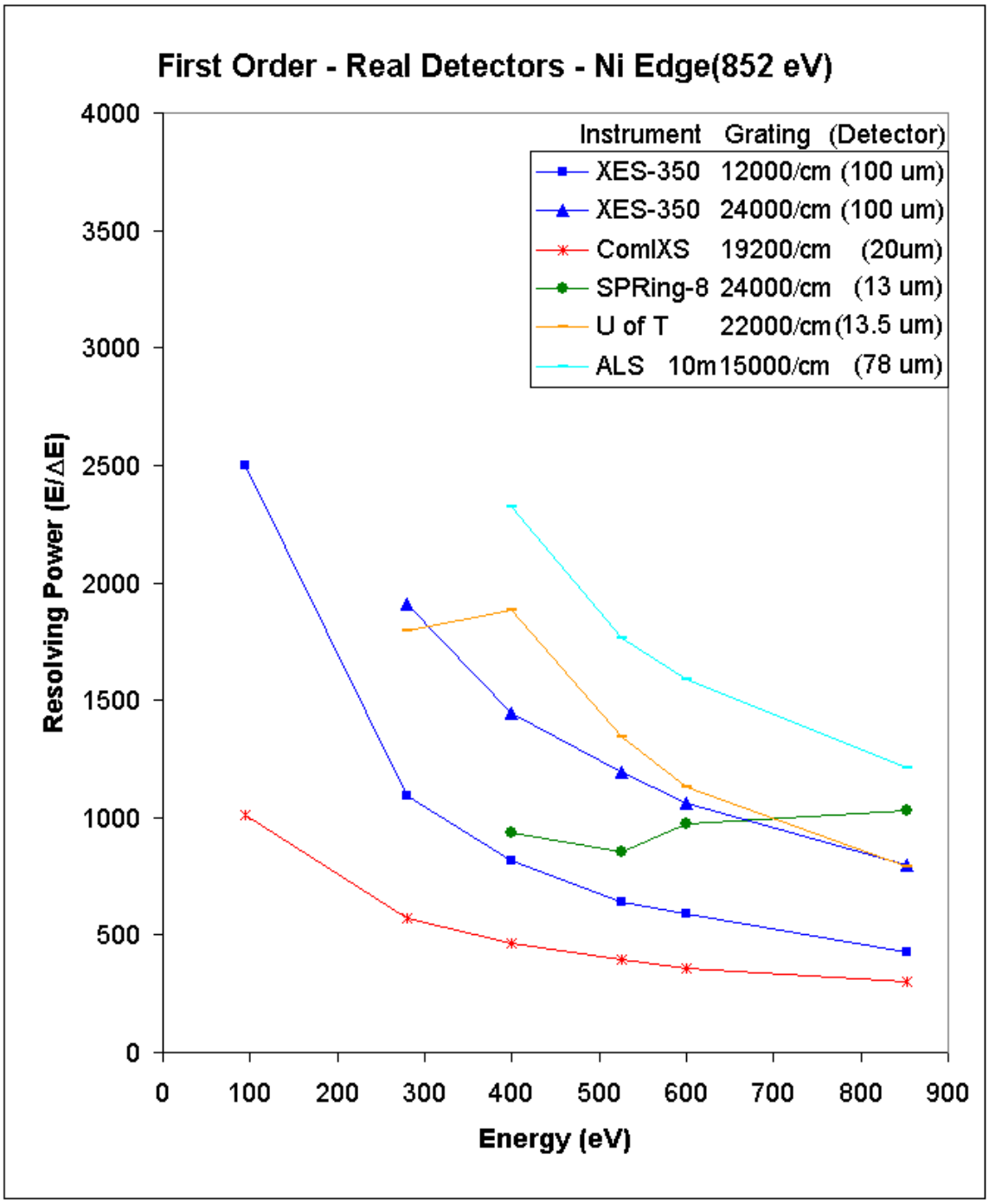

Figure 3.1 ***(cont.)*****:** Comparison of resolving power performance of spectrometer designs with their original detectors. Capabilities of each system are shown at the Ni $L_{2,3}$ emission edge. The legend specifies the spectrometer and grating (size and/or line density) with the detector pixel size in parentheses.

A detector is not an integral part of the optical design of a spectrometer and it can be upgraded with relative ease. This fact led to an additional set of calculations to compare the performance of all the spectrometers with the characteristics of the detector factored out. The same resolving criterion was used as was used for the first set of calculations, with one exception. Instead of requiring two spectral lines to be separated by one pixel width to be considered resolved, a standardized separation of 20 μm was used for all spectrometers. This allowed for the optical performance of each spectrometer to be considered independent of its specific detector characteristics. Fig. 3.2 shows the resolving power curves that resulted from this calculation. The final plot, Fig. 3.3, uses the same detector-standardized resolving power calculation technique as Fig. 3.2, but for the second diffraction order. The significance of the changes seen between these various figures, as they pertain to each spectrometer, is discussed in the following sections.

The results of this analysis, as well as comments on the design of each system and their specific strengths and weaknesses, are presented in the remainder of this chapter.

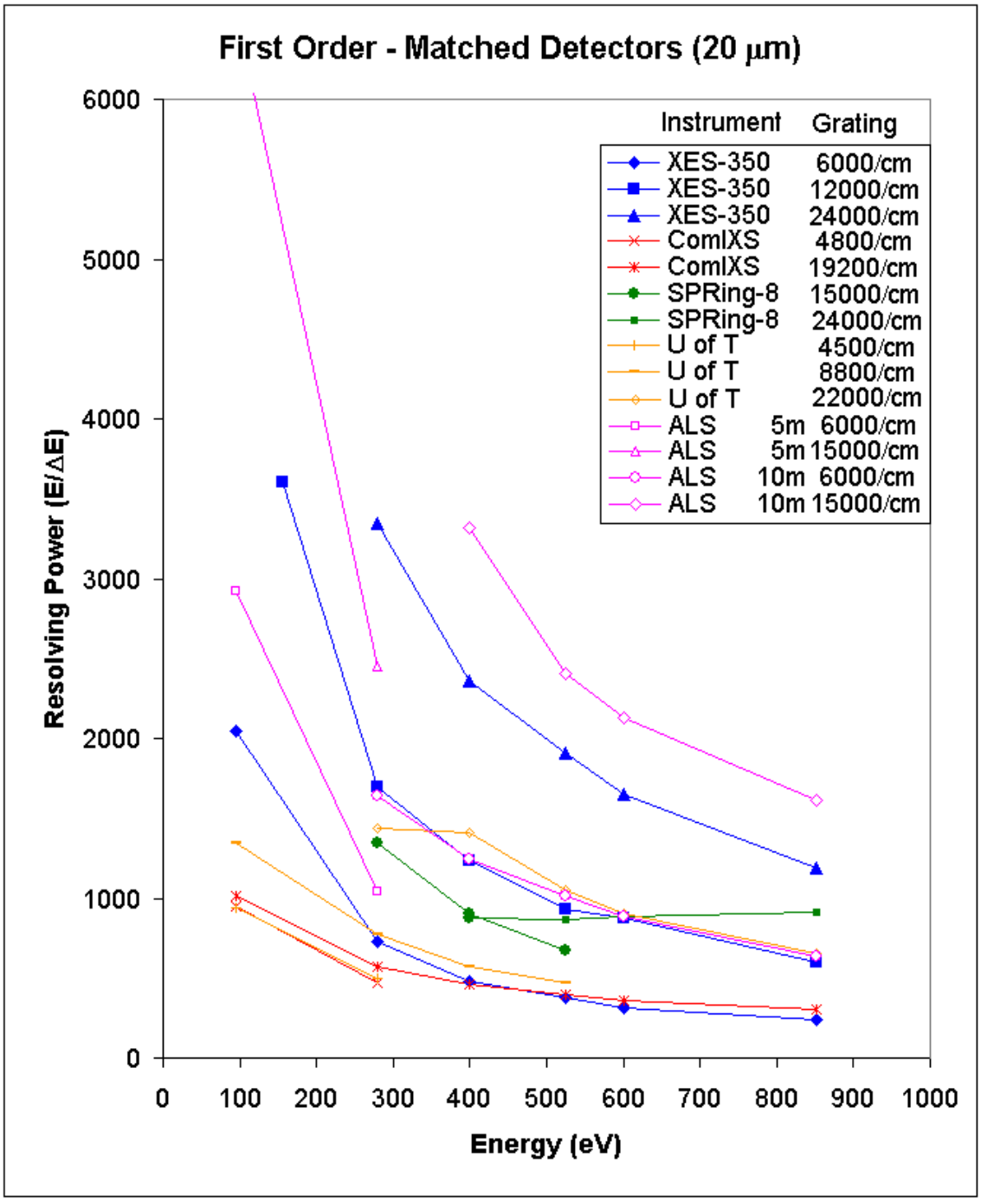

Figure 3.2: Resolving power performance comparison of spectrometer designs calculated with all detectors having a 20 μm pixel size. The legend specifies the spectrometer and grating (size and/or line density).

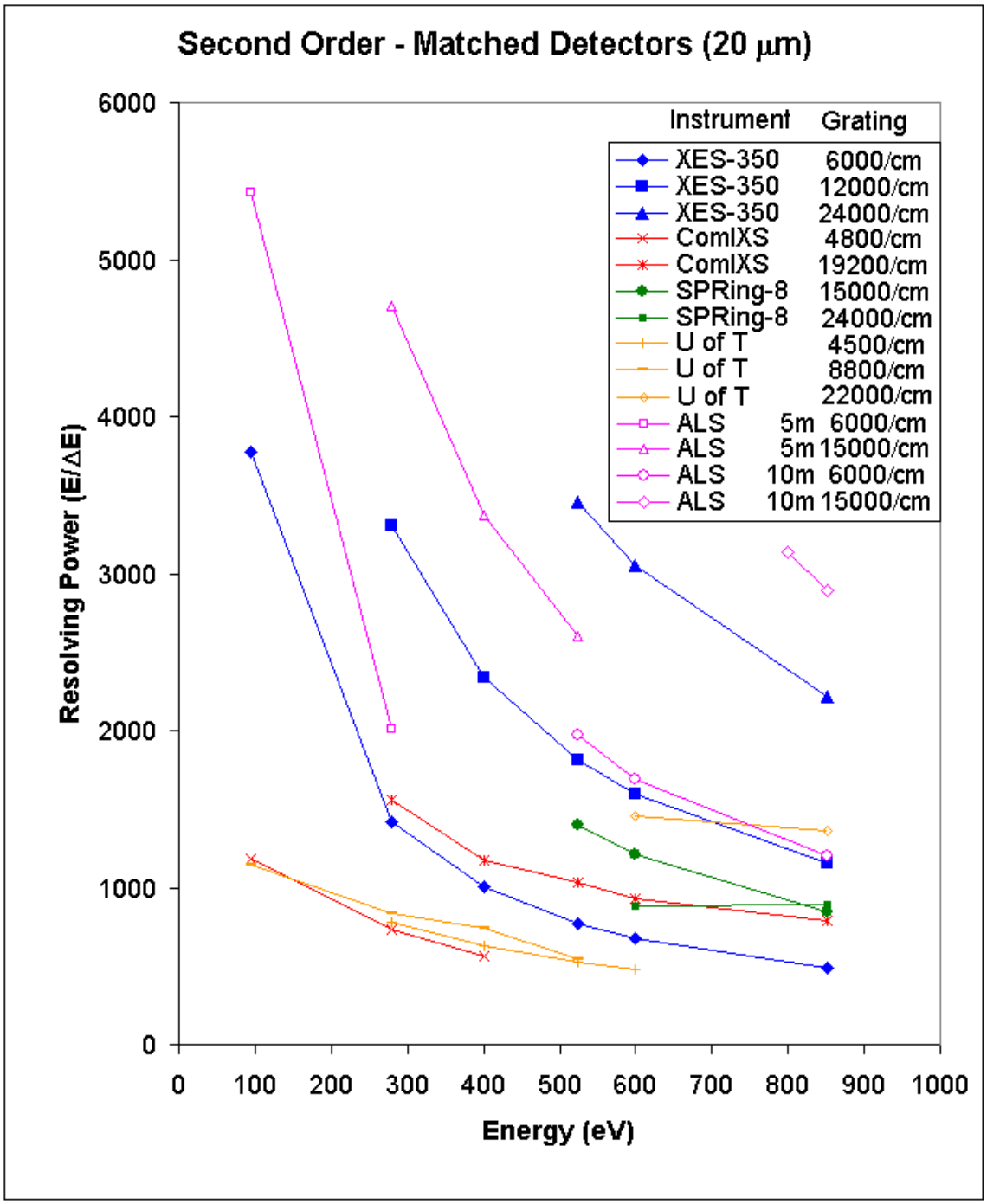

Figure 3.3: Comparison of second order resolving power performance of spectrometer designs calculated with all detectors having a 20 μm pixel size. The legend specifies the spectrometer and grating (size and/or line density).

3.1 Rowland Circle Systems

In this section, the performance of the two Rowland circle spectrometer designs that were analyzed is discussed. These two spectrometers are the Gammadata Scienta XES-350 spectrometer and the spectrometer on Beamline 8.0.1 at the Advanced Light Source. Their optical characteristics, as required for the ray-tracing calculations completed, are shown in Table 3.1. For each grating of each spectrometer, the table shows the operating energy range for that design, its radius of curvature (R), and line density (N_0). The optical layout of the gratings for each spectrometer is given by specifying the designed sample grating distance (r) and the grating incidence angle (α). All other required optical parameters (diffraction angle and focal length) can be calculated for any given energy from the equations found in Section 2.4. Finally, the detector pixel size for the spectrometer is stated. This is the pixel size that was used in the calculated data presented in Fig. 3.1.

Table 3.1: Optical characteristics of the Rowland circle spectrometers analyzed

Spectrometer	Grating	Energy Range eV	Radius R, cm	Sample Grating r, cm	Groove density N_0 (cm^{-1})	Incidence Angle 90° - α	Detector Pixel Size μm
XES-350	G3	18 - ...	500	16.525	6000	3.25	100μm
	G2	155-1600	500	22.356	12000	2.57	
	G1	250-1350	500	28.19	24000	1.9	
ALS BL 8	VLEG	40-110	500	34.88	6000	4	78μm
	LEG	90-270	500	34.88	15000	4	
	MEG	250-680	1000	34.88	6000	2	
	HEG	400-1000	1000	34.88	15000	2	

A brief discussion of each Rowland circle spectrometer design, its performance and its strengths and weaknesses is presented in the following sections.

3.1.1 Gammadata Scienta XES-350

The XES-350, the only commercially available design, is produced by GammaData Scienta in Sweden[17]. It is a basic Rowland circle system, employing 3 interchangeable gratings to cover an energy range of 18-1600 eV. As can be seen in the second plot of Fig. 3.1, the 2400 line/mm grating of the XES-350 is a leading performer in the middle of our range of interest (around, 400 eV) but, as is shown in the first and third plots of Fig. 3.1, it falls short of most other systems in lower and higher energy ranges.

The analysis completed here suggests that this is due to their choice to use all 5m radius gratings instead of varying the radius appropriate to the energy range. They achieve resolving powers as high as they do by relying on extremely high groove densities (up to 24,000 lines/cm) which have greater manufacturing error and lower diffraction efficiencies than lower density gratings. The low resolution detector that comes standard with this spectrometer hinders its innate performance and significant improvement could be seen by upgrading it. This can be seen by noting the significant jump in the resolving powers of this instrument between Fig. 3.1 and Fig. 3.2.

3.1.2 Beamline 8.0.1 at the Advanced Light Source

This spectrometer was designed by Tom Callcott's group[18] and is currently in use on beamline 8.0.1 at the Advanced Light Source in Berkeley, California[19], where our group currently conducts the bulk of its measurements. This spectrometer is a solid performer across our range of interest. It has an unusual high line-density, low radius grating for the low end of the energy range which boasts impressive resolving powers but would be expected to have low diffraction efficiency. Because of the solid performance of this spectrometer it was chosen as a starting point for the spectrometer designed by our group. As with the XES-350, an upgrade to a modern high resolution detector would significantly improve its performance.

3.2 VLS Grating Systems

In this section, the performance of the three VLS spectrometer designs that were analyzed is discussed. These three spectrometers are the ComIXS at ELETTRA, beamline BL27SU at SPRing-8 and a new spectrometer being built by T. Callcott at the University of Tennessee. The optical characteristics of these spectrometers, required for the ray-tracing calculations completed, are shown in Table 3.2. For each grating of each spectrometer, the table shows the operating energy range for that design, its radius of curvature (R), nominal line density (N_0) and the polynomial coefficients describing its line density variation (b_i). The optical layout of the gratings for each spectrometer is given by specifying the designed sample grating

distance (r) and the grating incidence angle (α). All other required optical parameters (diffraction angle and focal length) can be calculated for any given energy from the equations found in Section 2.4 and Section 2.4.2. Finally, the detector pixel size for the spectrometer is stated. This is the pixel size that was used in the calculated data presented in Fig. 3.1.

Table 3.2: Optical characteristics of VLS spectrometers analyzed

Spectrometer	Grating	Energy Range eV	Radius R, cm	Sample Grating r, cm	Groove density, variation coefficients N_0 (cm^{-1})	b_2	b_3	b_4	Incidence Angle $90° - \alpha$	Detector Pixel Size μm
ComIXS	Grating 1	20-200	1433	63	4800	29.8	1055	-	2.6	20μm
	Grating 2	100-1200	1433	63	19200	29.8	1069	-	2.6	
SPring-8	Grating 1	250-450	706.7	25	15000	4.22	45.6	1612	3	13μm
	Grating 2	400-900	1124	25	24000	10.7	40.0	8290	2	
Callcott 's UofT	Grating 3	80-300	955	50	4500	12.8	345	9968	2	13μm
	Grating 2	120-480	1430	50	8800	22.0	849	41205	2	
	Grating 1	300-1200	1430	50	22000	22.0	849	40872	3	

A brief discussion of each VLS spectrometer design, its performance and its strengths and weaknesses is presented in the following sections.

3.2.1 ComIXS at ELETTRA

ComIXS, or the **COM**pact **I**nelastic **X**-ray **S**pectrometer[20], was designed by D. Cocco in Kevin Prince's group for the BACH[21,22] beamline of the ELETTRA synchrotron in Trieste, Italy. The objective of the design of this spectrometer was to produce a moderate performance, highly compact spectrometer. Advantage was taken of the ability of a VLS grating to compact the focal curve. The size of the system was further reduced by using only two gratings over the entire energy range and moving the detector in only one dimension along the flat focal field produced.

ComIXS uses what could be called a "partial Rowland circle" focal curve by enforcing the first half of Eqn. 2.10 to simplify Eqn. 2.12. This reduces the design parameters that need to be considered but also fixes variables that could otherwise be manipulated to reduce aberrations. This was a reasonable choice since the primary design goal was a compact and flexible machine, not high performance. Also, because of the large energy range that must be covered by each grating, any attempts to aberration correct the grating to a specific energy would hinder its performance across the rest of the range. Since we are not restricted to a compact spectrometer, and do require outstanding performance, this design is not a reasonable choice to meet the needs of our group.

3.2.2 SPRing-8

The spectrometer on beamline BL27SU[23] of the SPRing-8 synchrotron in Japan is a compact VLS design intended to achieve high efficiency and moderate resolving power. It exhibits average resolving power across its designed range which is limited to 250-900 eV. This design does not use a Rowland-constrained focal curve allowing for aberration correction that results in sharp focal characteristics near the design energy of the gratings. The strong energy dependence of this aberration correction can be seen in the decline in low energy performance of the 1500 lines/mm grating (see the first plot in Fig. 3.1). In order to achieve the performance it does, despite its compact flat focal field design, it requires a cutting edge 13 μm pixel CCD detector. Again, the focus of this design on a mechanically simple and compact system makes it unable to meet the needs of our group.

3.2.3 University of Tennessee VLS Spectrometer

This spectrometer is being constructed by T. Callcott at the University Tennessee[24]. Similar to the SPRing-8 spectrometer it is a compact (approximately 1 m total length) VLS design requiring an extremely high resolution (13 μm) CCD detector to achieve moderate performance. It is not a suitable choice for our group for the same reasons as the other VLS designs.

3.3 The Second Diffraction Order

To achieve improved resolving performance at the cost of diffraction efficiency, a spectrometer can be operated in the second diffraction order. In theory, this should result in twice the dispersion providing twice the resolving power.

This is very nearly the case for the two Rowland Circle designs. Due to the order dependence of the terms of the optical path function for VLS systems (Eqn. 2.12), however, VLS spectrometers tend to behave erratically outside the diffraction order they were designed for (the first diffraction order in the case of all the designs presented here). The performance of the analyzed spectrometers in the second diffraction order can be seen in Fig. 3.3. By comparing it to Fig. 3.2 it can be seen with relative easy that Rowland circle spectrometers (XES-350 and ALS, blue and magenta lines) which are grouped near the top Fig. 3.2 are above the remaining VLS designs by an even larger margin in the second diffraction order (Fig. 3.3) than they are in the first order (Fig. 3.2).

This demonstrates an additional drawback of VLS systems, namely that they lose the flexibility to be operated in higher orders to trade efficiency for increased resolution at the discretion of the user, since no significant gain is achieved.

3.4 Conclusion

Table 3.3 shows, for each of the spectrometers analyzed, the best resolving power that can be achieved in the first diffraction order by each spectrometer at a number of common energies of interest. For each spectrometer, the grating that produced the best resolving power was chosen, within the motion limits of the spectrometers mechanical design and without regard for diffraction efficiency. These values are taken from the detector-standardized calculations (shown in Fig. 3.2). The dramatic performance difference between constant line spaced (Rowland circle) spectrometer designs the more compact VLS designs is quite clear from these figures.

Table 3.3: Best resolving powers for each design at energies of interest, calculated with 20 μm detector pixel sizes.

eV	XES-350	ALS 8.0.1	ComIXS	SPRing-8	Callcott U of T
95	2049	6555	950	n/a	1344
280	3346	2448	571	1343	1441
400	2356	3318	465	899	1414
852	1184	1609	304	910	650
	Constant Line Spaced		*Variable Line Spaced*		

The results of these calculations very clearly show that the Rowland circle spectrometer designs have superior resolving performance as compared to the VLS spectrometer designs. In addition they have the added flexibility of being able to achieve

significantly higher resolving powers by operating in the second diffraction order, though this will reduce diffraction efficiency. The VLS designs do have advantages that are not highlighted by these calculations. All of the VLS spectrometer designs presented here are significantly smaller than the Rowland circle spectrometer designs presented. Additionally, the linear focal field that can result from VLS designs can make them mechanically simpler and even more compact. Neither of these advantages support the goals of this spectrometer design project. These results therefore suggest that a Rowland circle design will best succeed at achieving the design goals set out for this project.

Chapter 4

Our Optical Design

After completing the analysis of existing systems, our calculations suggested that it would be possible to design a spectrometer that exceeded existing designs in resolving power and efficiency. This could be accomplished by focusing our efforts on optimizing for specific energies of interest, not sacrificing performance to create a mechanically simple system and by taking advantage of higher line density gratings now being produced. After seeing performances achieved by existing designs we settled on aiming for a minimum resolving power of 2500 through our range of interest and striving for excellent efficiency in a reasonably sized and flexible design. By keeping these goals in mind, and carefully balancing resolving power and diffraction efficiency using the calculation techniques developed, a design meeting these objects has been completed.

In the course of the study of our diffraction efficiency calculations it was noticed that, with proper design, superior diffraction efficiency could be achieved in the third diffraction order as compared to the second diffraction order. A novel grating system was devised to exploit it.

These proposed designs and the methods used to obtain them are outlined in the

following sections.

4.1 Basic goals and design requirements

Having decided that our needs would best be met by designing a custom spectrometer, we established the specifications within which we needed to work. The initial design requirements that we began with specified an operational energy range of 90 eV - 1100 eV. A minimum resolving power of 2000 throughout most of this range was desired, using our detector standardized resolving criterion (20 μm detector pixel size). Based on our experience with the performance of the designs we analyzed and some preliminary calculations, we decided to aim for a minimum resolving power of 2500 at all of the energies of interest specified for this design (Si L-edge: 92 eV, C K-edge: 285 eV, N K-edge: 410 eV, Fe L-edge: 710 eV). Since the diffraction efficiency was not known for any of the designs analyzed, and could not be calculated due to incomplete knowledge of their optical characteristics, it was impossible to establish a quantitative goal for the efficiency of our system. Since the design goals focused more on superior resolving power than high efficiency, we opted to optimize the efficiency to the best of our ability as the design proceeded, making appropriate compromises between efficiency and resolving power where needed. The initial specifications of the beamline suggested that there would be enough space to accommodate a spectrometer with a maximum optical path length of approximately 1.5 m. With these goals established, the process of decided on a spectrometer style and design approach and completing an initial design could begin.

4.2 Design parameters

Two styles of spectrometer were analyzed and considered for this design, Rowland circle and variable line spaced (VLS). The Rowland circle designs analyzed were by far the superior performers. With the relatively large amount of space we had to work with for our design, the compactness gained by implementing a VLS design was not required. The ability of VLS gratings to be designed to correct for aberrations at a particular energy would compromise our ability to provide high resolving power throughout the entire energy range of the design. Although a significant amount of effort was put into seeking a way to take advantage of the added flexibility of VLS in our design, in the end, a basic Rowland circle design became the clear choice.

With the design goals established and the spectrometer style chosen, the following parameters were left to specify the design:

1. the number of selectable gratings that will be required to achieve the desired performance across the entire energy range of the design;

2. the sample grating distance, r, which for the sake of mechanical simplicity should be the same for all gratings;

3. the size (width and length) of each grating, typically the same for all gratings;

4. the radius of curvature, R, of each grating;

5. the line density, N, of each grating;

6. incidence angle, α, for each grating;

7. the coating material of each grating;

8. the blazed angle, ϕ, of each grating;

9. the detector to be used.

While there are a large number of parameters to be decided, there is significant interrelation between them. Some of these parameters will be dependent on each other, which ones being dependent on the design approach chosen. The design goals state requirements for the resolving power, diffraction efficiency and total length. Most of the listed design parameters will, in some way, affect more than one of these requirements. This means that any choice of a value for any parameter must be carefully considered to balance its effect on all the requirements. Each requirement, and how it is effected by the various parameters, will be discussed in the following sections.

4.2.1 Design parameters effects on optical path length

The optical path length can be approximated as the sum of two parameters: the source-grating and grating-detector distances ($r + r'$). This may seem relatively simple, but these two parameters are intimately connected to both the resolving power and efficiency in several ways. How these parameters relate to those the resolving power and efficiency will be left to the next two sections, where each is discussed. Where the optical path length becomes a limiting factor in the design, it will be mentioned there.

4.2.2 Design parameters effects on resolving power

The resolving power of a spectrometer is a function of the spatial energy dispersion at the detector, the detector resolution and the image quality. Two of the listed parameters effect the image quality. Off normal incidence angles ($\alpha \neq 0^o$) cause aberrations (coma) which becomes a significant factor in the image quality as the source is moved further off the optical axis. However in order to achieve total external reflection, the only way to create reasonably efficient optical elements in the soft X-ray regime, grazing incidence is required. Within the range of effective grazing angles, the coma does not change significantly and, as a result, the image quality can not be significantly improved by adjusting this parameter. Spherical aberration is strongly dependent on the size of the optical element. As such, the length of the gratings must be kept as small as possible to prevent spherical aberrations from becoming significant. The downside of this is that smaller gratings cover smaller solid angles and therefore collect fewer photons, reducing efficiency.

The most significant controllable impact on resolving power comes from the spatial dispersion at the detector. The spatial dispersion is the result of two separate factors, the angular dispersion and focal distance. For any given angular dispersion, the spatial dispersion at the detector will be greater at longer focal lengths. However, the optical path length of the system is limited, which is why multiple gratings are required. Since the best resolving power will be obtained at the furthest accessible region of the focal curve, each separate grating can be design to diffract a different range of energies into this optimum focal length region.

The focal distance, r', is function of energy, and as such, is not an explicit design variable. For any given energy, it is defined by the grating radius, R, the incidence angle, α, the sample grating distance, r, the line density, N and the diffraction order, k. The first three parameters (R, α, r) characterize the Rowland circle and the relative position of the source and grating on the Rowland circle. Recall, the Rowland circle is a virtual curve in space on which the source, grating and detector must be placed on to satisfy the Rowland focal conditions (see Section 2.4). The three are not independent, because the first half of the Rowland circle condition (Eqn. 2.10):

$$r = R\cos(\alpha) \tag{2.10}$$

must be satisfied. The line density and incidence angle determine the diffraction angle for a given energy, λ, through the grating equation (Eqn. 2.9):

$$Nk\lambda = (\sin\alpha + \sin\beta) \tag{2.9}$$

where β is the diffraction angle. A higher diffraction order simply results in a lower diffraction angle for a given energy, and therefore a focal distance further along the Rowland circle. With the diffraction angle and those first three parameters (R, α, r) established, the focal length, r', for any given energy can be determined by satisfying the second half of the Rowland circle condition (Eqn. 2.10):

$$r' = R\cos(\beta) \tag{2.10}$$

As discussed in Section 2.3, angular dispersion is the rate at which the diffraction angle changes with energy. Greater dispersion results in more separation between spectral features. The standard expression for angular dispersion is:

$$\left(\frac{d\beta}{d\lambda}\right)_{\alpha} = \frac{Nk}{\cos\beta} \tag{2.3}$$

This equation tells us that the angular dispersion is dependent on the diffraction order, k, line density, N and diffraction angle, β. However, as a design variable, α is not constant. According to Eqn. 2.9 β depends on α and according to Eqn. 2.10 α, in turn, depends on r and R. This is a perfect example of how complex the interrelations between these design parameters can be.

4.2.3 Design parameters effects on efficiency

The efficiency of a grating has two distinct components: geometric efficiency and diffraction efficiency. The first, geometric efficiency, is relatively simple. A larger effective grating area results in more photons being collected. However, as mentioned already, longer gratings result in more spherical aberration which reduces the resolving power, so a balance must be found. The effective area of the grating is also effected by the incidence angle, α, since higher incidence angles results the grating appearing smaller to the source. This means that a lower incidence angle results in higher geometric efficiency. Unfortunately, lower incidence angles also result in lower diffraction efficiencies (discussed below). To further complicate matters, the incidence angle is already a key factor in determining the focal distance for a given

energy and it must be carefully controlled to place the desired energies at the optimum focal distances for a given grating. The final factor that effects the geometric efficiency is the source-grating distance, r'. A longer source-grating distance results in a smaller solid angle being collected and a lower efficiency. However, moving the grating closer to the source requires the Rowland circle be smaller or the incidence angle to be higher if the Rowland condition is to be satisfied, which will affect the resolving power and diffraction efficiency. The other factor to be considered is the limited ability of the source to to fully illuminate the grating. The source for this spectrometer will be an entrance slit on the order of tens of microns high, illuminated by a similarly sized emitting spot on a sample approximately a centimeter behind it. This will produce a cone of light of very limited size. The minimum distance that will result in complete illumination of the grating is an important factor in choosing a source-grating distance.

The diffraction efficiency is affected by the incidence and diffraction angles, the line density, the blaze profile and the grating coating material. Luckily, the blaze profile and grating material do not affect anything other than the diffraction efficiency allowing some independent control over it. As described in the previous two sections, the rest of the parameters are intimately tied to both the resolving power, geometric efficiency and optical path length of the system. Higher incidence angles result in higher diffraction efficiency because the reflectivity of the grating materials increases as the incidence angle increases, but this also leads to lower geometrical efficiency. Changing the incidence angle also dramatically affects the focal distances and angular dispersion which must both be carefully controlled to ensure that the de-

sired energies are being diffracted into the right region of the focal curve for optimum performance. The line density and diffraction angle are interrelated and similarly tied to the resolving power and optical path length. Generally, reducing the line density increases the diffraction angle which increase the diffraction efficiency but shortens the focal length and hence reduces the resolving power.

4.3 Design methodology

In general, all the interrelations between the different parameters are in the form of trade-offs. The design process becomes a matter of carefully adjusting each parameter, with consideration for the others and within the constraints of the Rowland condition, to find an optimum performance balance.

Of the two Rowland circle designs that were analyzed, the ALS beamline 8.0.1 spectrometer was by far the better performer (see Section 3.1.2). Because of this we took the basic optical layout of this spectrometer as a starting point for our design. The ALS spectrometer uses four selectable gratings to cover the energy range of 40-1000 eV. Since our design calls for a similar energy range, we chose to start with the same number of gratings. This fortuitously corresponded to the number of points of interest that were specified for our design, so one grating was optimized for each of the four energies of interest. These four gratings were:

1. a Lower Energy Grating (LEG) optimized for the Si L-edge at 92 eV

2. a Medium Energy Grating (MEG) optimized for the C K-edge at 285 eV

3. a High Energy Grating (HEG) optimized for the N K-edge at 410 eV

4. an eXtremely High Energy Grating (XHEG) optimized for the Fe L-edge at 710 eV

The radii of the four gratings on the ALS spectrometer were constrained to two values (500 cm and 1000 cm), presumably so their focal curves would overlap making the mechanical design and optimization simpler. By removing this constraint on the grating radii, implementing modern higher line-density gratings, and carefully optimizing the resolving power and efficiency for each energy of interest, we were able to achieve significantly improved performance for our design.

Due to the high degree in interrelation between the various design parameters and their effects on performance, the design process was anything but linear. The final design evolved out of the experience gained and lessons learned from dozens of experimental designs, starting from a rough best-guess design and iteratively improving it over time.

Figure 4.1 shows a design process flow chart. This may not be a true representation of the actual process used since it was also a learning process. It is, however, a fair approximation of the process used and it is the procedure that would be used were a similar project to be undertaken in the future. Even using this procedure, the design is not a simple process. There is significant flexibility in establishing N and α, which is why initial best guesses are required. In addition, determining whether or not the design goals have been met can be somewhat difficult since optimal efficiency and high resolving power are extremely subjective requirements.

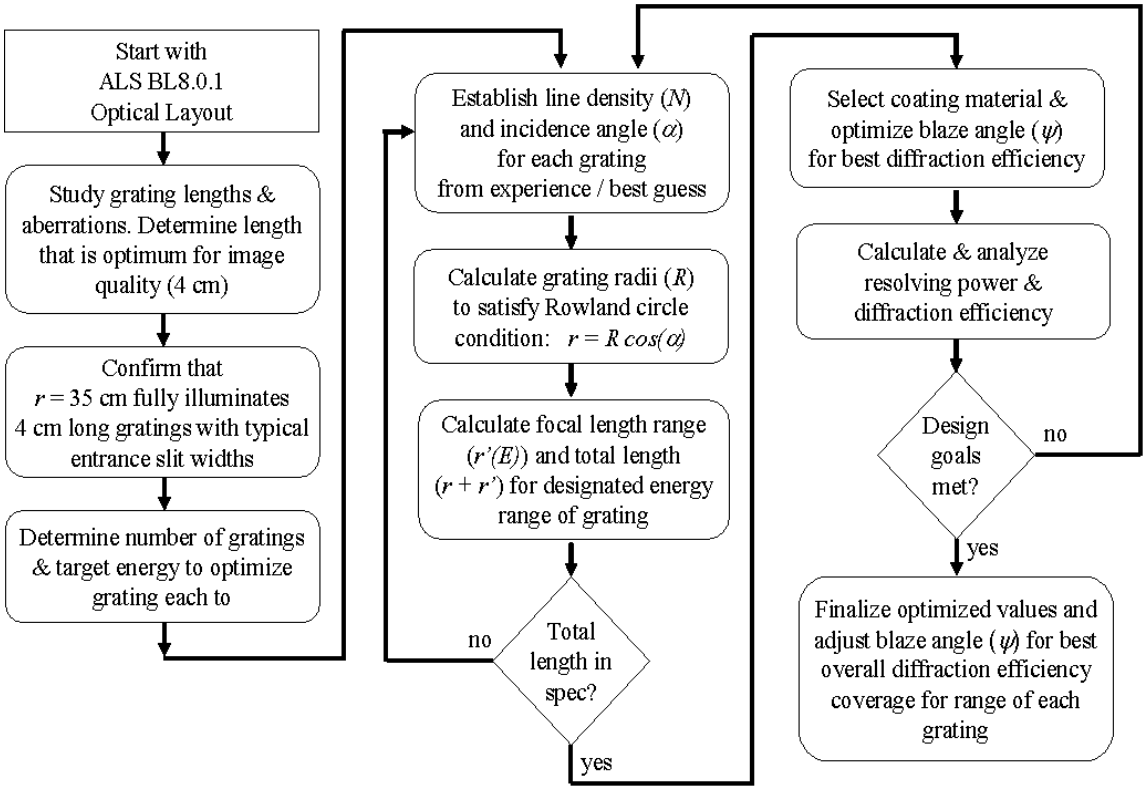

Figure 4.1: This flowchart represents the basic steps that were required to establish the current design. The actual process used is not shown. Instead, an optimized process based on the lessons learned during the design is shown.

While it is difficult to explain the entirety of this process, the key factors that determined many of the final parameter values are discussed in the following sections. Each section deals with a different parameter or set of parameters. The constraints and effects that had the greatest impact on determining their final values are discussed. The process that led to establishing what those optimum final values were is explained.

4.4 Grating Size

While the grating size may seem like a relatively insignificant place to start, it is a key factor in determining the overall optical layout. The grating size is critical in determining the optimum source-grating distance, which will in turn affect all other design parameters. It seems generally desirable to have the biggest possible grating to collect photons from the largest possible solid angle. However, many of the aberrations present in spherical optical elements are directly related to the size of the grating, resulting in a trade-off between collection efficiency and resolution. A series of ray-trace calculations were performed with varying grating sizes. From these calculations it was found that 40 mm long gratings were the largest size possible before these aberrations noticeably impacted the image at the detector, resulting in a significant decrease in resolving power. Fig. 4.2 shows the images formed at the detector of three discrete energies emitted from the entrance slit. Four different images are overlayed in different shades of grey, each the result of a different sized grating. The images formed by 20 mm and 40 mm long gratings (in black and white) are tightly focused. There is no significant image degradation in going from a 20 mm grating to a 40 mm grating and the effective resolving power is the same. Significant defocus due to spherical aberration is clearly visible for gratings longer than 40 mm (light and dark grey). For every additional 20 mm of grating length beyond 40 mm the effective resolving power is reduced by a factor of 2.

The gratings will need to be at least 20 mm wide in order to ensure complete illumination of a detector up to 40 mm wide. Gratings 30 mm wide will likely be

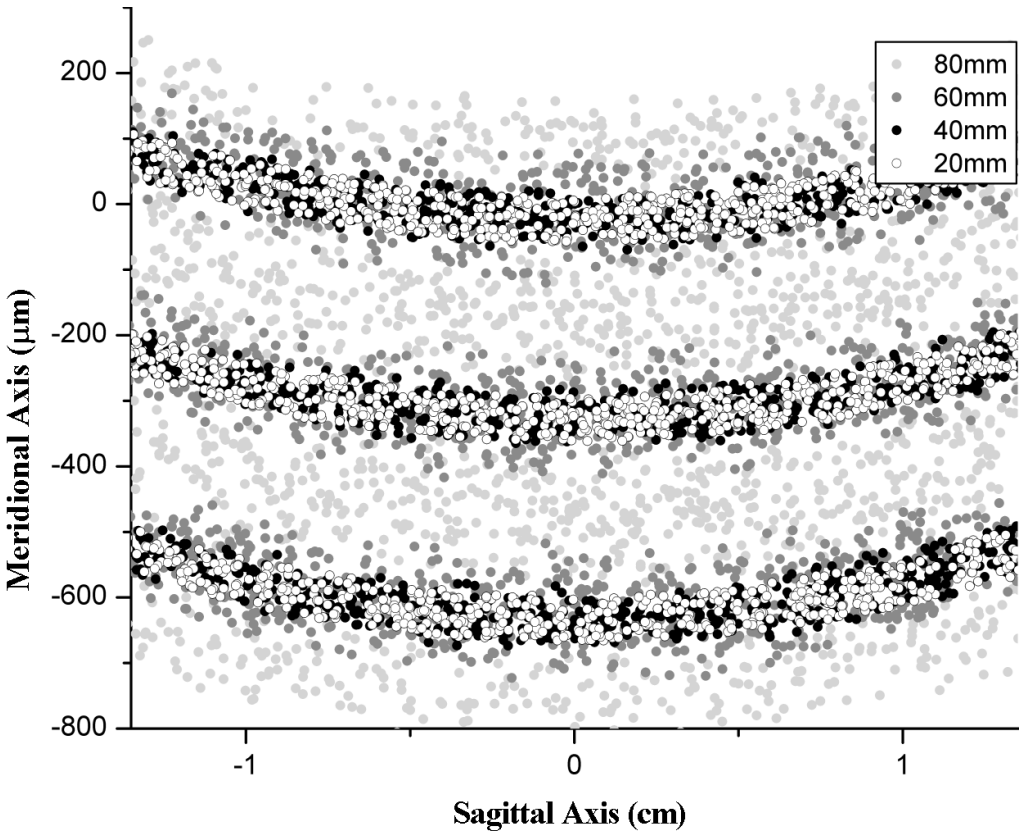

Figure 4.2: Image formed at the detector by gratings of various lengths. Marked defocus due to spherical aberration is clearly visible for gratings longer than 40 mm.

ordered to accommodate wider detectors that may be available in the future. This will also provide for the possibility of using coupled translations to "rotate" the grating around its meridional axis, reducing the degrees of freedom required from the mechanical design. Knowing the desired size of the gratings, the designer can establish an optical layout that is capable of properly illuminating them.

4.5 Optical Path Length

Beamline 8.0.1, the starting point for our design, has an optical path length of 1.3 m, slightly smaller than our specified maximum length of 1.5 m. However, it was found

that the entrance slit to grating distance, r, of 35 cm that the ALS design uses results in good illumination of a 40 mm long grating for typical entrance slit sizes and grating incidence angles. This is still a reasonable fraction of the total optical path length of our design, leaving a sufficient maximum grating-detector length to allow access to a large region of the focal curve. The total detector motion range (grating to detector distance, r') of 50 cm - 115 cm was settled on so that the total optical path ($\approx r + r'_{max}$ = 35 cm + 115 cm) was near the targeted 1.5 m. The 50 cm lower limit to the focal curve has been tentatively determined to ensure access to sufficiently high energies. This optical layout is shown in Fig. 4.3, including the entire detector motion area that will be required to access the energy ranges of the gratings detailed in the following sections.

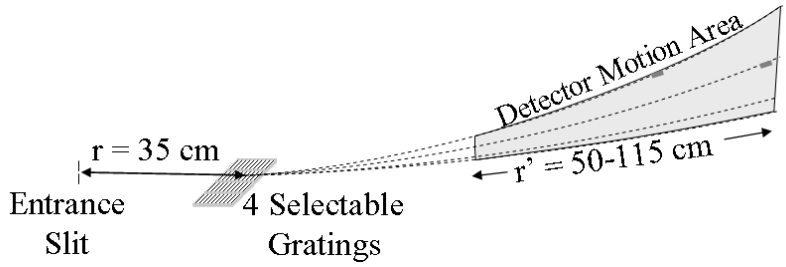

Figure 4.3: The optical layout of our spectrometer design, showing the relative positions of the entrance slit and gratings, and the motion area of the detector required to access the full focal field.

Changes to the CLS beamline layout after the design had been completed resulted in significantly more space being available than previously anticipated. A careful review of the design showed that using the additional space would not improve the overall performance of the spectrometer. Any attempts to further improve the resolving power by enlarging the design would result in unacceptable losses in efficiency. The changes to the CLS beamline layout did however allow us to proceed

with the extremely high resolution third diffraction order design mentioned, which is described in Section 4.8.

4.6 Optical Element Design

Designing the gratings without constraint on the focal curves (other than total length) allowed for maximum optimization of resolving power and efficiency. The grating incidence angle, line density and blaze angle were carefully balanced for each designed grating and the grating radius of curvature was allowed to float to satisfy the Rowland condition (Eqn. 2.10). The process used, discussed in section 4.3, was one of iterative refinement of a a series of initial parameter sets. The initial parameter sets were chosen based on the results of our analysis of existing designs and rough calcualtions to ensure they satisfied the Rowland condition and would fall within the maximum optical path length. The iterative refinement was completed with the goal of achieving resolving powers above 2500 with the best possible efficiency at each of the energies of interest (Si L-edge: 92 eV, C K-edge: 285 eV, N K-edge: 410 eV, Fe L-edge: 710 eV).

Once the best design had been settled on and the first round of optimization was completed, it was noted that the MEG (optimized for 285 eV) and the HEG (optimized for 410 eV) were very similar in design and performance. These two gratings were therefore merged into a single Medium Energy Grating (still called the MEG) and the HEG was eliminated from our design. This grating was re-optimized to perform well at both target energies (285 eV and 410 eV).

In optimizing the first three gratings, an understanding of the trade-offs between efficiency and resolving power was gained. This led to the concept of designing a grating that was more focused on high efficiency than high resolving power. With this idea, a fourth grating was added to provide higher efficiency and reasonable resolving power over a wide range of energies for measuring low intensity samples such as impurities. We therefore called this the Impurity Grating, or IMP for short.

4.7 Final Design Parameters and Performance

The parameters that were finally settled on after completion of this design process are listed in Table 4.1. Additionally, the energy ranges that each grating will be able to access by moving within the 50 cm - 115 cm focal range are given for the first and second diffraction orders. All four gratings are optimized for best performance in the first diffraction order. The only parameters not specified in this table are the grating sizes and source grating length. The optimum grating length, as was shown in Section 4.4, was found to be 40 mm, though 80 mm long gratings may be considered for reasons discussed in Section 5.4. Gratings 30 mm wide will ensure complete illumination of the detector. The source-grating distance, as established in Section 4.5, will be 35 cm for all gratings.

The resolving power performance, as calculated using our 20 μm detector standardized calculation technique, is shown for the energies of interest for this design in Table 4.2. The achieved diffraction efficiency for each grating at each energy is also shown. Fig. 4.5 shows, overlaid, the resolving power and efficiency performance

Table 4.1: Specifications of the gratings for our spectrometer design

	Groove Density (lines/cm)	Incidence Angle (degrees)	Blaze Angle (degrees)	Coating	Grating Radius (cm)	1st Order Range (eV)	2nd Order Range (eV)
LEG	6,000	86	1.85	Au	501.7	30-300	60-600
Impurity	9,000	87	1.11	Ni	668.7	75-750	150-1500
MEG	12,000	88	1.48	Ni	1002.9	250-2500	500-5000
HEG	20,000	88	1.52	Pt	1002.9	400-4000	800-8000

across the energy range of each grating. These plots provide a good visual impression of the overall performance of each grating for any given energy. The advantage of multiple gratings to cover the energy range is clearly shown. Careful design has matched the peak efficiency for each grating to the energy range it is designed to operate in.

Table 4.2: Resolving power and efficiency for each grating of our design at energies of interest

	Standard Gratings							
	IMPURITY		LEG		MEG		XHEG	
eV	RP	Eff	RP	Eff	RP	Eff	RP	Eff
92	4693	7.4%	2986	38.7%	10146	5.3%	15580	3.6%
285	1722	29.1%	1032	3.8%	3646	19.6%	5752	6.7%
410	1226	34.1%			2528	22.8%	4039	9.8%
710	731	23.4%			1588	17.7%	2595	12.2%

*Shaded boxes denote energies unreachable within initial 50-115~cm focal curve

Fig. 4.4 shows all gratings for all designs calculated using a our 20 μm detector standardized criterion. The bold lines indicate the performance of the gratings of our spectrometer which, as can be seen, are surpassed only by the low energy performance of beamline 8.0.1 at the ALS.

Plots, similar to those found in Chapter 3, detailing the performance of our design as compared to all other spectrometers are shown in Appendix B.

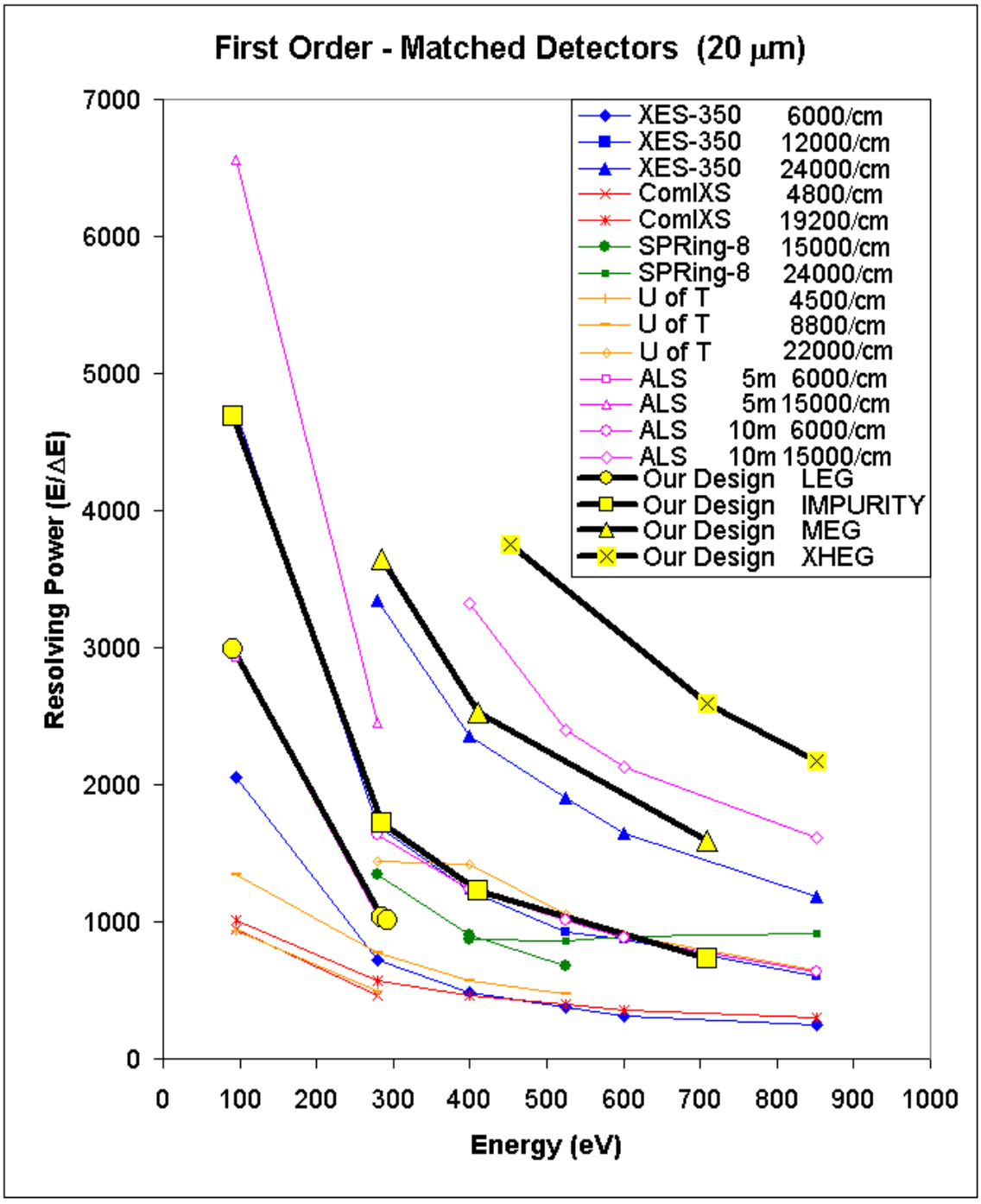

Figure 4.4: Comparison of Our Design to Existing Spectrometer Designs calculated with all detectors having a 20 μm pixel size. The legend specifies the spectrometer and grating (size and/or line density)

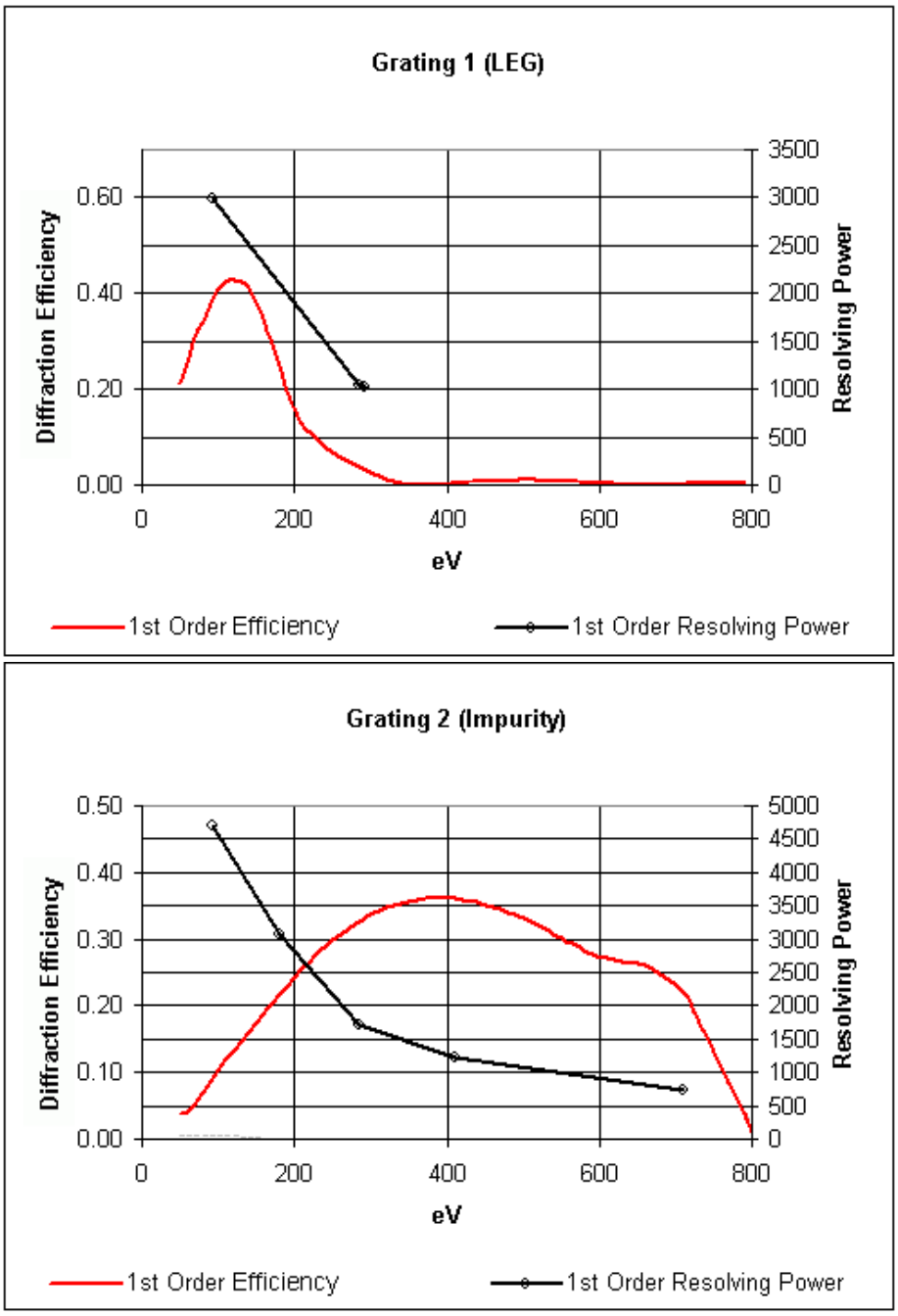

Figure 4.5: Resolving power and diffraction efficiency for each grating in our spectrometer design. Careful design has matched the peak efficiency for each grating to the energy range it is designed to operate in. Broken lines indicate energy ranges that could be accessible if the motion range detector is extended.

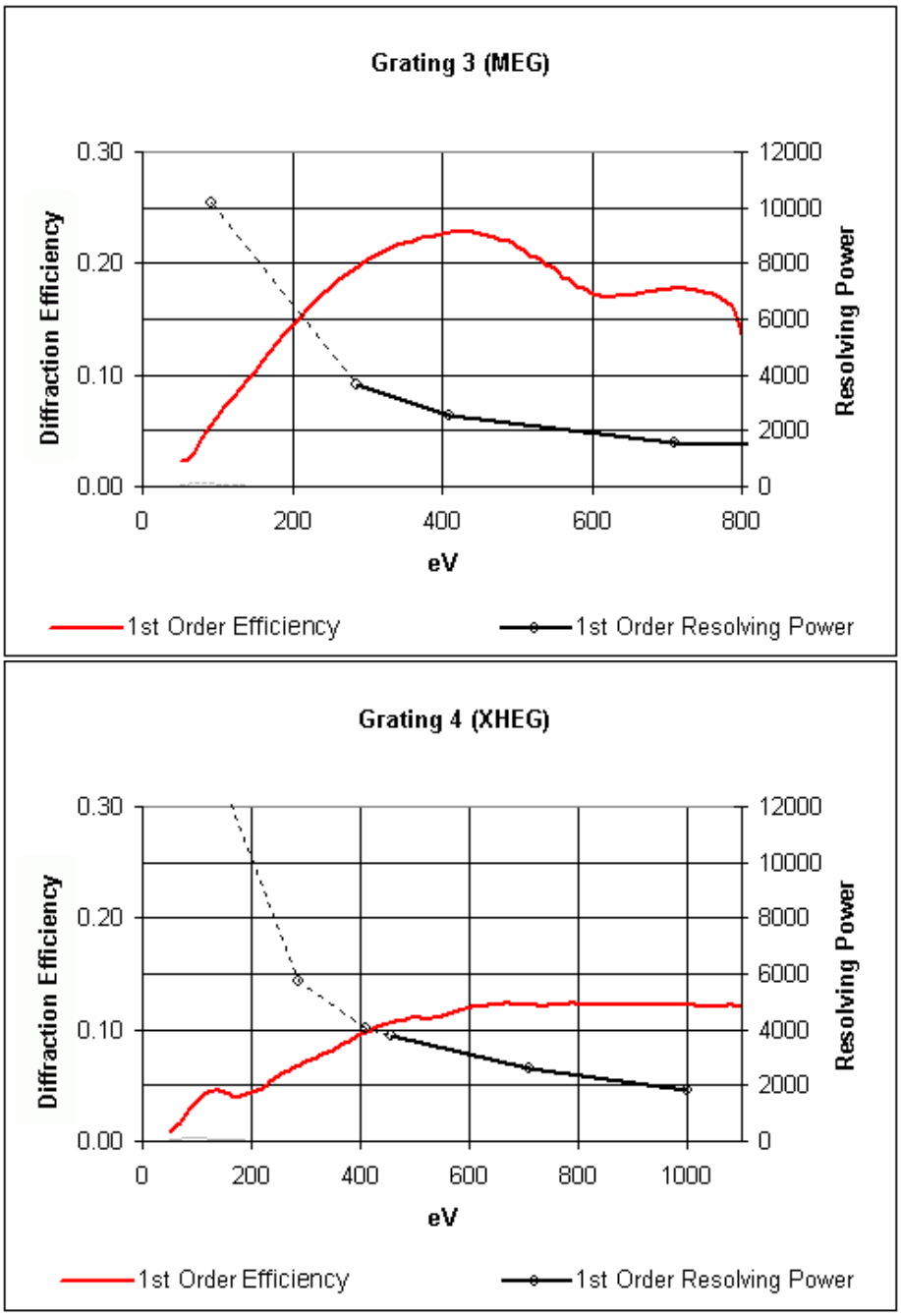

Figure 4.5 ***(cont.)*****:**Resolving power and diffraction efficiency for each grating in our spectrometer design. Careful design has matched the peak efficiency for each grating to the energy range it is designed to operate in. Broken lines indicate energy ranges that could be accessible if the motion range detector is extended.

4.8 High Resolution 3rd Order Gratings

In performing calculations to explore the behavior of diffraction efficiency, Mark Boots, a member of my research group, noticed that the third diffraction order can provide performance superior to that of the second diffraction order if the gratings are properly blazed to take advantage of it. He proposed that this may be exploited as a novel method of achieving extremely high resolving powers. This was attempted with the goal of achieving a resolving power of over 10,000 throughout the high end of the energy range of our design. Two additional High Resolution gratings were designed to cover the Medium and High energy ranges (the HRMEG and the HRHEG). These gratings were designed and optimized by following a procedure similar to that used for the first four gratings. The final specifications of these gratings are shown in Table 4.3. These gratings have a very large focal curve (grating-detector distances as high as r' =220 cm, illustrated in Fig. 4.6) with low efficiency but stunning resolving power.

Table 4.3: Specifications of the 3rd order gratings for our spectrometer design

	Groove Density (lines/cm)	Incidence Angle (degrees)	Blaze Angle (degrees)	Coating	Grating Radius (cm)	3rd Order Range (eV)
HRMEG	18,000	88	4.85	Ni	1002.9	~285+
HRHEG	26,000	88.25	4.05	Pt	1146.1	~525+

Table 4.4 shows the resolving power performance of these gratings along with our standard first order gratings for common energies of interest. The achieved diffraction efficiency for each grating at each energy is also shown. This demonstrates

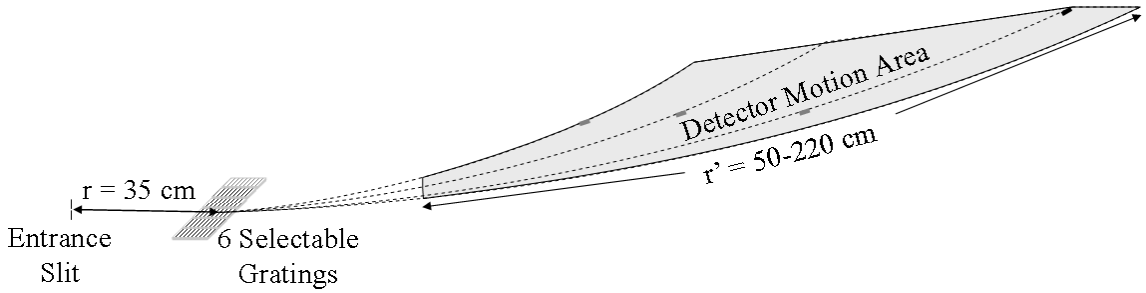

Figure 4.6: The optical layout of our high resolution third order spectrometer design, showing the relative positions of the entrance slit and gratings, and the extended motion area of the detector required to access the full focal field.

the sacrifice required to achieve these resolving powers. The diffraction efficiency is nearly an order of magnitude lower than the value for standard gratings. The resolving power and efficiency performance across the energy range of each grating is shown in Fig. 4.8. This gives a good visual impression of the overall performance of each grating for any given energy. The necessity of employing two gratings to cover the energy range is clear, due to the relatively low efficiency even in the designed energy range. Careful design was vital to ensure that the peak efficiency for each grating was matched to the energy range it was designed to operate in.

Table 4.4: Resolving power and efficiency for each grating of our design, including 3rd order gratings, at energies of interest

	Standard Gratings								3rd Order Gratings			
	IMPURITY		LEG		MEG		XHEG		HRMEG		HRHEG	
eV	RP	Eff	RP	Eff	RP	Eff	RP	Eff	RP	Eff	RP	Eff
92	4693	7.4%	2986	38.7%	10146	5.3%	15580	3.6%				
285	1722	29.1%	1032	3.8%	3646	19.6%	5752	6.7%	14066	4.7%		
410	1226	34.1%			2528	22.8%	4039	9.8%	10227	3.4%	16510	1.5%
710	731	23.4%			1588	17.7%	2595	12.2%	6238	0.9%	9468	2.1%

*Shaded boxes denoted energies unreachable within initial 50-115 cm focal curve

Fig. 4.7 shows all gratings for all designs calculated in the diffraction order they were designed to operate in and includes our 3rd order optimized gratings. These were calculated using our standardized 20 μm detector criterion. The dramatic difference in the resolving powers of these two gratings over all others is easily seen.

This approach was until very recently a purely conceptual one. Currently C. Heske's group at the ALS is implementing a design[25] that will be using the third diffraction order to measure at the Nitrogen emission edge (410 eV). They discovered this approach when a manufacturing error in the grating blaze angle fortuitously produced superior efficiency in the third rather than the second order.

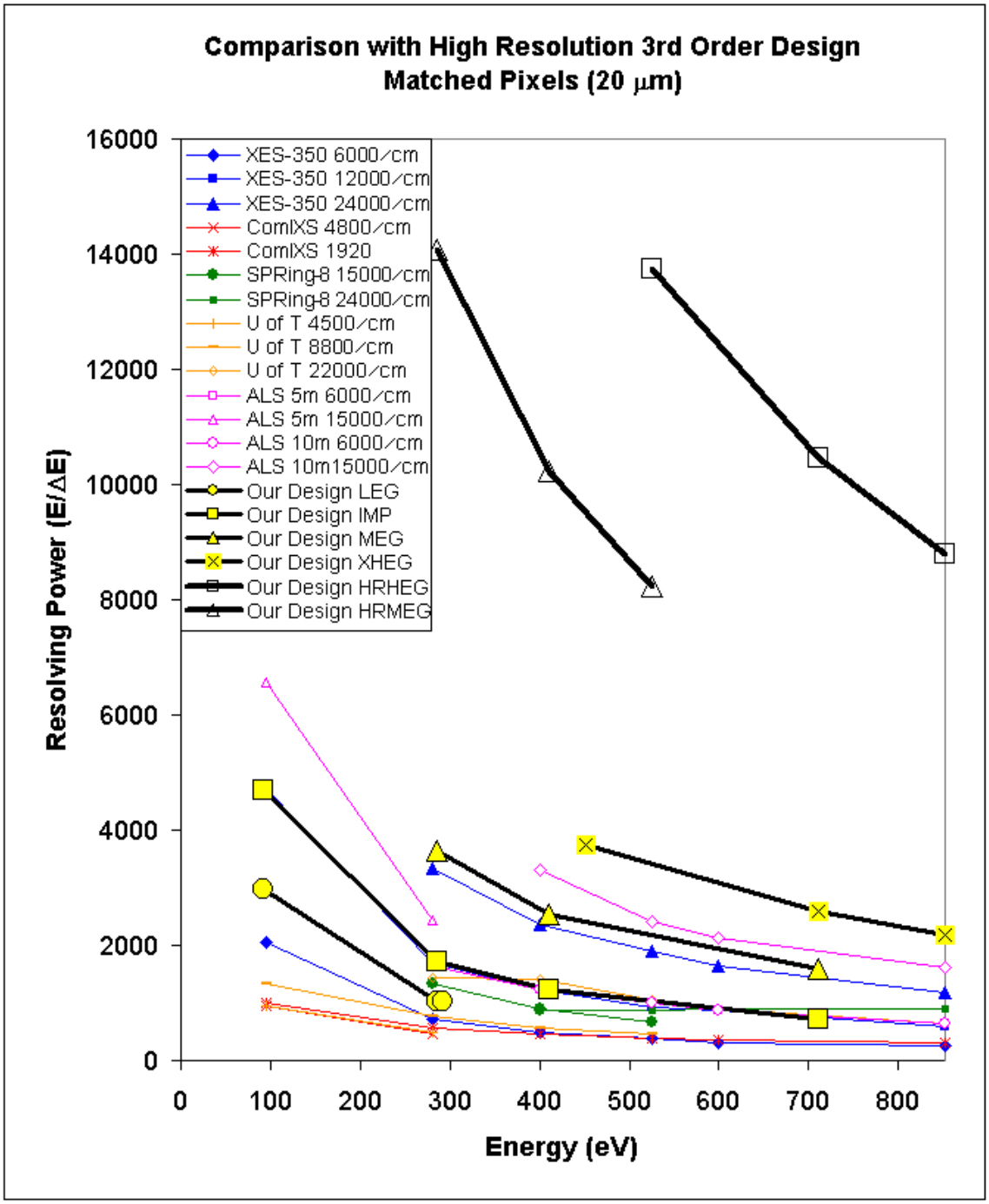

Figure 4.7: Comparison of our design, including our high resolution 3rd order gratings, to existing spectrometer designs calculated with all detectors having a 20 μm pixel size. The legend specifies the spectrometer and grating (size and/or line density)

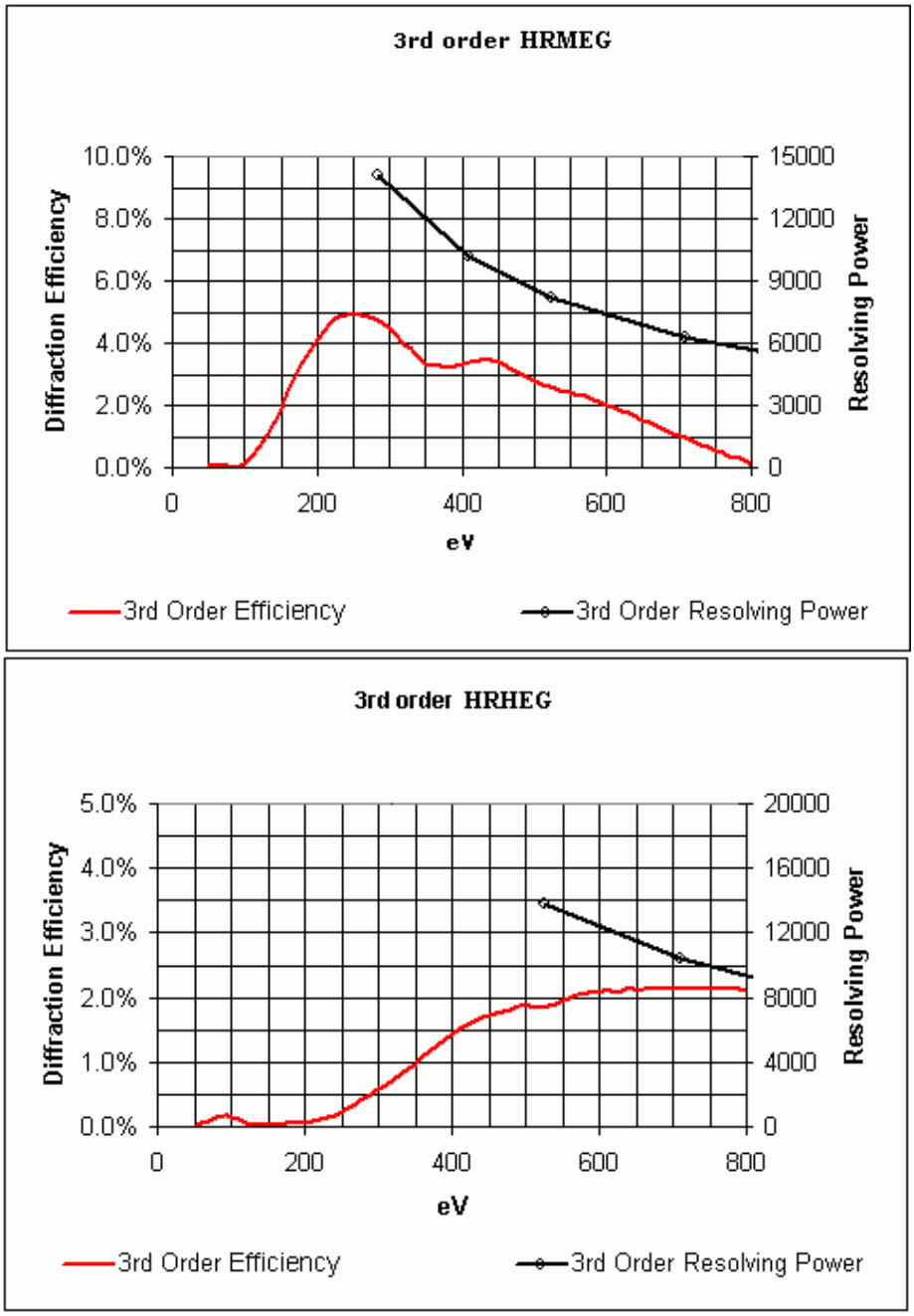

Figure 4.8: Resolving power and diffraction efficiency for each grating in our third order high resolution spectrometer design. Careful design has matched the peak efficiency for each grating to the energy range it is designed to operate in.

4.9 Conclusion

Table 4.5 lists the best resolving power that can be achieved in the primary order of each of the spectrometers analyzed, as well as for our design, at a number of common emission edges of interest. For each spectrometer, the grating that produced the best resolving power was chosen within the motion limits of the spectrometers mechanical design and without regard for diffraction efficiency. All calculations were performed assuming a 20 μm detector size for consistency.

Table 4.5: Best resolving powers for each design at energies of interest, calculated with all spectrometers using detectors with 20 μm pixels.

	1st Order	**3rd Order**					Callcott
eV	**Gratings**	**Gratings**	XES-350	ALS 8.0.1	ComIXS	SPRing-8	U of T
95	**4693**	n/a	2049	6555	950	n/a	1344
280	**3646**	**14065**	3346	2448	571	1343	1441
400	**3200**	**10226**	2356	3318	465	899	1414
852	**2170**	**8786**	1184	1609	304	910	650
	Our Design		*Constant Line Spaced*		*Variable Line Spaced*		

Table 4.5 shows that our design will achieve leading resolving powers throughout a wide spectral range. Only beamline 8.0.1 at the ALS would be able to compete, and then only with an upgrade from the current 78 μm detector to a modern 20 μm detector. The calculations for our base gratings assume a detector motion limit of 50 cm - 115 cm. If the full 220 cm motion range is available, the higher energy first order gratings will be able to reach lower energy ranges with greater resolving powers. If this is the case then the performance of this design will surpass that of the ALS at all energies. We were able to achieve a resolving power of 2500 at

all targeted energies of interest up to the Fe L-edge (710 eV), and nearly reached that performance level at the Ni L-edge (852 eV) as well. With the addition of our 3rd order high resolution gratings, our spectrometer will outperform all others by a factor of between three and eight depending on the specific energy.

All 6 gratings, as specified in this chapter, have been ordered and were being produced when this document was finalized.

Part III

Design Review

and

Analysis

Chapter 5

External Design Review

Having completed the optical design for our new soft X-ray emission spectrometer, and thereby achieving the initial goals of the project, work began towards realizing this design as a functioning scientific instrument.

As a first step towards this goal, an outside consultant was hired to assess and analyze our design. Dr. Ruben Reininger of Scientific Answers and Solutions LLC, a recognized expert in the field of soft X-ray optics, was retained for this purpose. We were particularly interested in an opinion of the overall approach and design, the analysis criterion used and any suggestions or approaches that may improve our design. We also inquired about the possibility of using some novel approaches such as variable groove depth and multilayered gratings. A document detailing our analysis of existing designs, the criterion used, the design approach we settled upon and our final design was prepared and presented to him. His comments and the resulting discussions are summarized in this chapter.

5.1 Diffraction Efficiency

Dr. Reininger verified our diffraction efficiency calculations by performing similar calculations for a groove profile with a high anti-blaze angle as produced by some manufacturing techniques (see Section 7.2 on page 116 for a discussion of various manufacturing techniques). His results were similar with slightly lower efficiencies, which is consistent with the varied blaze profile. While his calculations did not explicitly verify ours, due to his choice to use a different profile then the one we used (and specified), their similarity does lend support to our work.

The possibility of exotic solutions for increasing diffraction efficiency was also addressed. The available technologies that we had hoped may have some potential were variable groove depth and multilayer coated gratings. Multilayer coated gratings would have obvious difficulties in that the necessary quarter-wave layers would be in the 2-20 $\mathring{A}$ range, requiring near perfect atomic monolayers which is not feasible. This approach would also result in strongly wavelength dependent diffraction efficiency. Dr. Reininger confirmed our concerns and was of the opinion that this approach was not feasible.

Variable groove depth is a relatively new approach to maximizing diffraction grating efficiency. This approach, as Dr. Reininger explained, allows for run-time optimization of the efficiency by varying the groove depth across each groove. This allows the grating to be translated perpendicular to the beam in order to find the highest flux for any given incidence angle. Because of this, it is more suited to monochromators than spectrometers since it requires the grating to be significantly

wider than the incident beam, as is the case for a tightly collimated synchrotron source, and not for a point source, such as the emitting samples seen by a spectrometer such as ours.

5.2 VLS vs. Rowland Design

In our initial meeting with Dr. Reininger, he questioned my decision to use a Rowland circle design. He expressed his opinion that a properly designed VLS system could produce a better image with superior resolving power. It would also have the added advantage of producing an image without curvature so post-processing the image would not be required. This point was the center of a lively discussion, which led to both of us setting out to find further support for our assertions. The results of my efforts have been presented in Section 2.4.2. Dr. Reininger failed in his attempt to produce a VLS design that exceeded the performance of my Rowland design. The reason for this is shown Fig. 5.1.

Regardless of the quality of an aberration-corrected image that can be produced with a VLS grating, the aberration correction will always be energy dependent, as explained in Section 2.4.2. Fig. 5.1 demonstrates that, while a VLS gratings forms a good image at the optimized energy of 200 eV, the image is severely aberrated only 50 eV away. This would result in the effective range of each grating being extremely narrow. It can also be seen that, even though it is strongly reduced, the line curvature is still present. This curvature would still significantly reduce the resolving power if not corrected by post-processing the image.

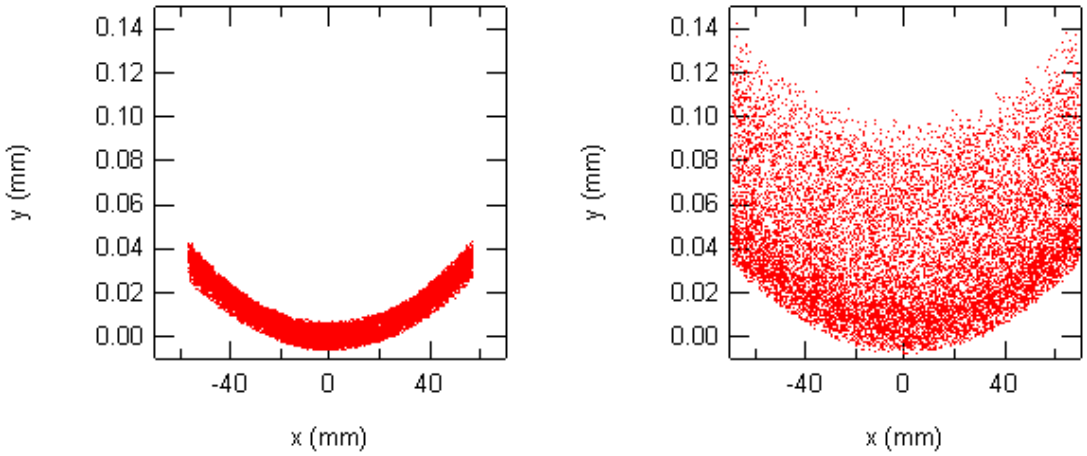

Figure 5.1: Images from Dr. Reininger's VLS grating design which is aberration corrected to 200 eV.[26] **Left:** Image of a slit emitting 200 eV photons. **Right:** Image of a slit emitting 250 eV photon. The abberation due to the energy dependence of a VLS grating is evident.

5.3 Analysis of Our Design

Dr. Reininger performed analytical calculations to determine the resolving power of our design. He stated that, in his experience, the equations he used are in good agreement with the actual performance of systems he has worked on. The equation he provided for this purpose was:

$$\Delta\lambda = \frac{1}{Nk}\sqrt{\left(\frac{\cos(\alpha)s}{r}\right)^2 + \left(\frac{\cos^2(\beta)d}{r'}\right)^2 + \mathrm{SE}^2 + \mathrm{SA}^2} \tag{5.1}$$

using

$$\mathrm{SE} = 2 \times 2.7\sigma \cos\left(\frac{\alpha+\beta}{2}\right)\cos\left(\frac{\alpha-\beta}{2}\right) \qquad \text{Surface Errors}^{27,28} \tag{5.2}$$

and

$$\mathrm{SA} = \frac{2.7}{2}\sigma_i \left(\frac{1}{r} - \frac{\cos\alpha}{R} + \frac{1}{r'} - \frac{cos\beta}{R}\right)\frac{1}{R} \qquad \text{Spherical Aberrations}^{8} \tag{5.3}$$

where s is the entrance slit width, d is the detector pixel size, σ is the RMS slope error and σ_i is given by

$$\sigma_i = \sqrt{\frac{\int_{-\ell}^{\ell} x^6 dx}{2\ell}} \tag{5.4}$$

for a fully illuminated grating.

Eqn. 5.1 provides an analytical approximation of the resolution of a spherical diffraction grating in terms of wavelength, which is proportional to the resolution in terms of energy ($\Delta\lambda \propto \Delta E$). Wavelength and energy can be used interchangeably in determining resolution and resolving power as:

$$\begin{aligned} d\lambda =& d\frac{hc}{E} = -\frac{hc}{E^2}dE \\ |\frac{\lambda}{d\lambda}| =& \frac{\frac{hc}{E}}{\frac{hc}{E^2}dE} = \frac{E}{dE} \end{aligned} \tag{5.5}$$

This allows Eqn. 5.1 to be used to determine the energy resolution or resolving power of an instrument, as used in the remainder of this document. The leading factor indicates that the resolution is inversely proportional to the line density of the grating and the diffraction order being considered. The first term under the radical expresses the contribution of the entrance slit and entrance arm (as defined by the incidence angle, α, and the slit/grating distance, r) to the resolution. The second term accounts for the detector resolution (pixel size) and the exit arm as defined

by the diffraction angle, β, and the focal distance, r'). The third term of Eqn. 5.1, defined in Eqn. 5.2, accounts for the contribution of surface error to the resolution. The surface error is primarily a function of the slope error, σ, which describes the angular deviation from a true spherical surface (see Section 6.1 for more detail). The fourth and final term of Eqn. 5.1, defined in Eqn. 5.3, accounts for the image degradation caused by spherical aberration and by using an incidence angle off the primary optical axis. This effect is dependent on the illuminated size of the grating, account for by σ_i, defined in Eqn. 5.4.

The results of Dr. Reininger's calculations using these equations are shown in Fig. 5.2. The data, presented as Dr. Reininger provided it, is shown as energy normalized bandwidth ($\Delta E/E$) plots which is the inverse of the resolving power ($E/\Delta E$) plots presented in the remainder of this thesis. In addition to the configuration we considered (10 μm entrance slit, 40 mm long gratings), Dr. Reininger also completed these analytical calculations for a 20 μm entrance slit illuminating 80 mm long gratings, and include these calculations on these plots. His plots show not only the final bandwidth, but also show each contributing term (Eqn. 5.2 and 5.3) separately. For clarity, the relevant final results on his plots (those corresponding to the configuration used in my calculations) have been highlighted with bold lines. The results from my ray-trace calculations have been overlaid in broken bold. Fig. 5.2 shows that, for all four gratings, Dr. Reininger's predicted bandwidth (bold lines) are below that predicted by our calculations (broken bold lines). This is equivalent to his calculations predicting a higher resolving power than our calculations. It is reasonable to conclude that our calculations are conservative and we can expect the

system to perform as we predicted or better, assuming Dr. Reininger's assertions are accurate.

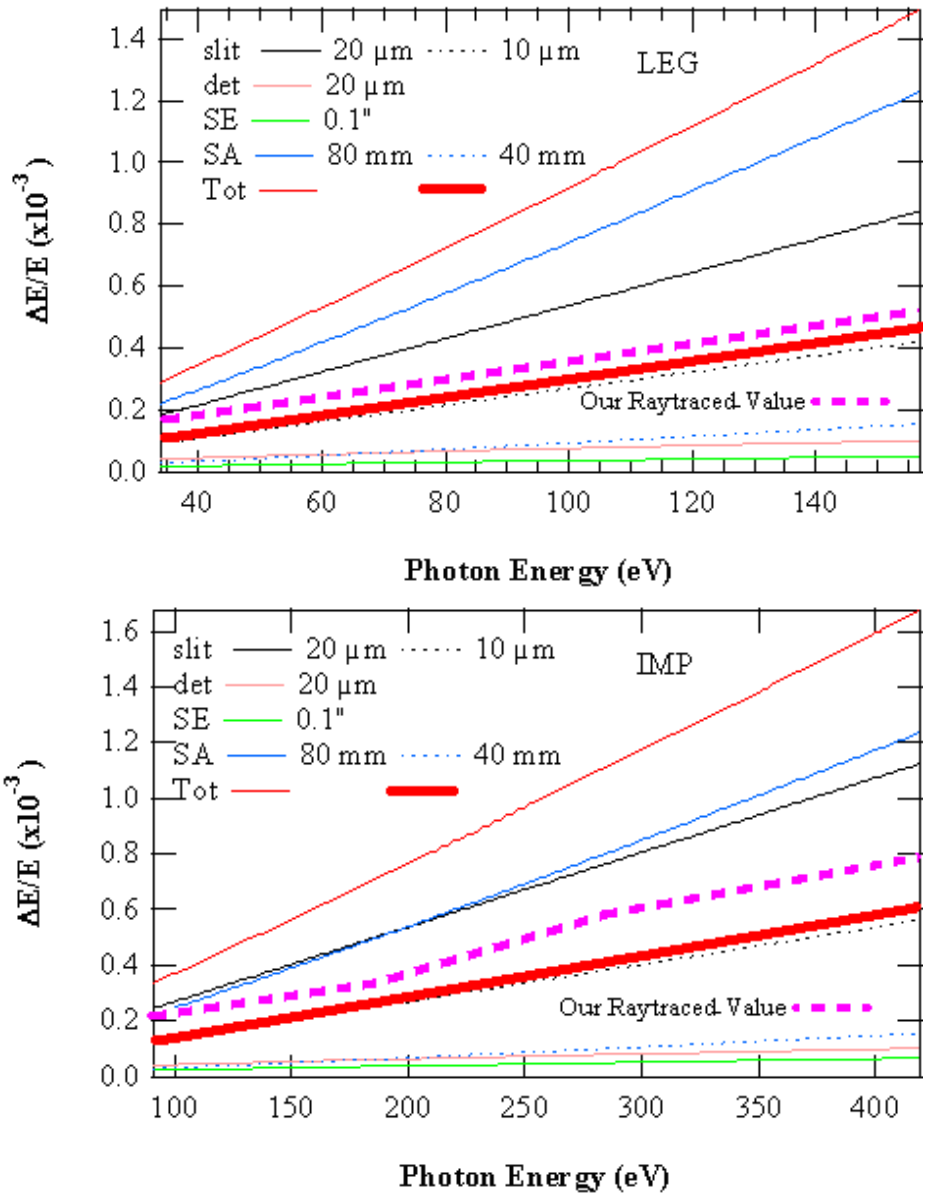

Figure 5.2: Contributions to the bandwidth of the 4 gratings in our base design.[26] The bolded lines are Dr. Reininger's calculated results for a 40 mm grating. The broken bolded lines are based on our ray-traced values. Dr. Reininger's calculations suggest our design will perform even better than we predict.

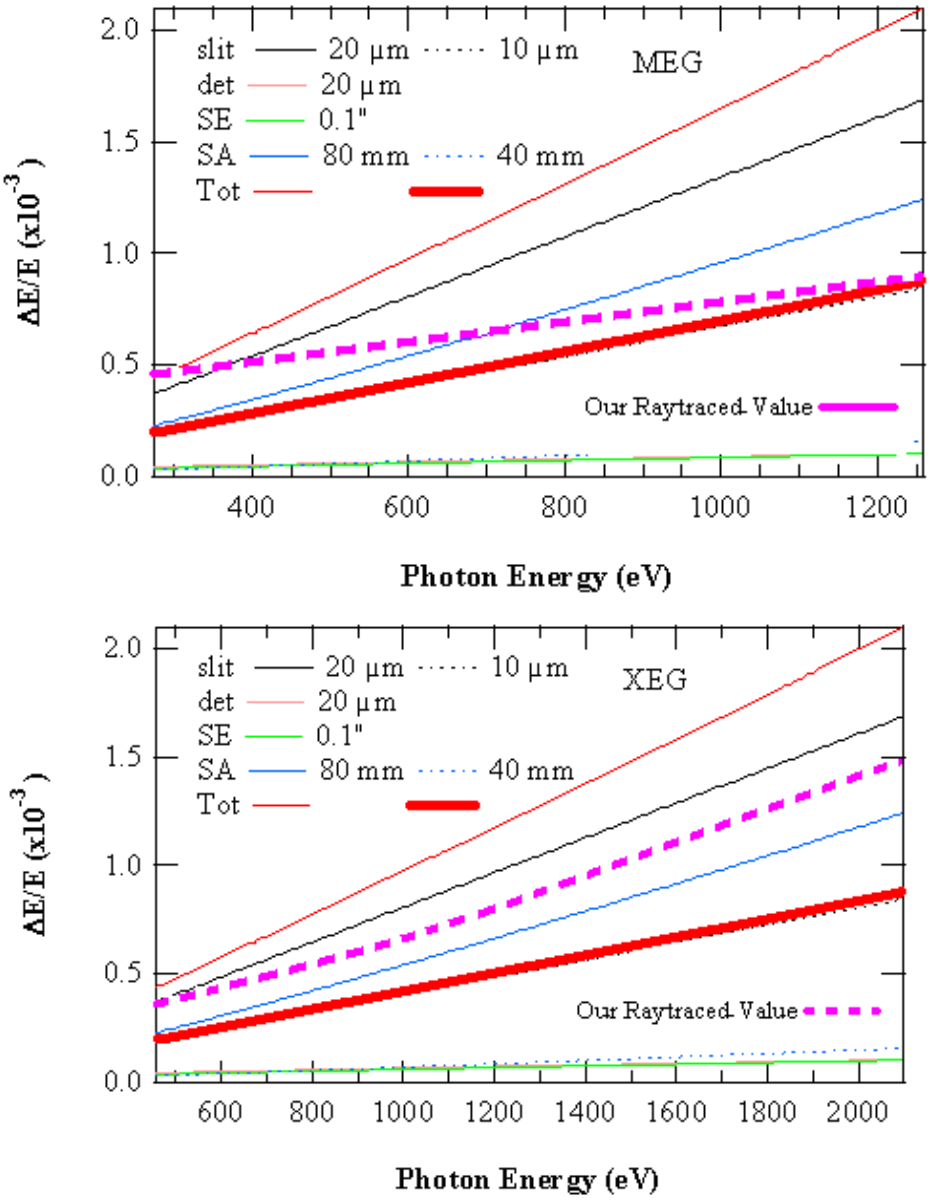

Figure 5.2 ***(cont.)*****:** Contributions to the bandwidth of the 4 gratings in our base design.[26] The bolded lines are Dr. Reininger's calculated results for a 40 mm grating. The broken bolded lines are based on our ray-traced values. Dr. Reininger's calculations suggest our design will perform even better than we predict.

5.4 Grating Size

Dr. Reininger points out that these equations show the contribution of Spherical Aberrations (SA, Eqn. 5.3) to the resolution of a grating 80 mm long is comparable to the contribution of a 20 μm slit. This suggests that an 80 mm long grating would be a reasonable maximum size to avoid the dominant source of image degradation coming from spherical aberrations. He also recommends that we employ a removable mask that allows for a 40 mm effective grating length to achieve the resolving power suggested by our ray-trace calculations. We currently plan on implementing this recommendation, as long as the larger gratings are not cost prohibitive.

5.5 Conclusion

In our consultation with Dr. Reininger, we were able to rule out the availability of any exotic solutions that may increase the efficiency of our spectrometer. His diffraction efficiency calculation results were in general agreement with ours, supporting our work. With Dr. Reininger's assistance, I was able to confirm, to my satisfaction, my belief that a Rowland circle spectrometer will outperform a VLS spectrometer for designs that are not significantly constrained by total size. Dr. Reininger's analytical resolving power calculations suggested our design would perform even better than our calculations suggest. Based on this and his experience, we can expect the performance of our design to meet or exceed our specifications.

Chapter 6

Tolerance Calculations

One of the most significant factors in determining the cost of manufacturing a complex machined component, like a grating, is the required accuracy. The complexity of aligning and calibrating an optical system is also a significant cost factor, both in terms of precision mechanical components and labour expenses. It is desirable to minimize the cost of the required components without having a detrimental effect on the quality of the performance of the spectrometer. To achieve this, some understanding of the effects of variations in the design parameters was required. To gain this understanding, a series of calculations were undertaken to explore the sensitivity of the resolving power and diffraction efficiency of the spectrometer to different design variables.

6.1 Grating Figure Error

The most significant parameter in determining the image quality of an optical element is its figure accuracy. In order for the incident rays to be properly focused

by the optical element, the true surface of the element must be as close as possible to the theoretical geometry assumed in the design process. This figure accuracy is typically quantified in one of two ways. RMS slope error is a measure of the average deviation of the angle of the optical surface from the angle required to form the desired geometry. Slope error is typically quoted in either arcseconds or mrads. Wave error is a measure of either the maximum or RMS difference in the distance traveled by an incident ray as it passes through an optical element and the distance it would travel were that element geometrically perfect. Wave error is measured in terms of a fraction of a wavelength, typically at the HeNe laser line (632.8 nm).

6.1.1 Figure Accuracy Unit Conversion

Different manufacturers tend to use only one of the above units, depending on the technique they use to measure the figure accuracy of the optical elements they produce. The first step in understanding the capabilities of these manufacturers was to find some way to meaningfully compare their quoted capabilities. No existing method of converting between these two different methods of quantifying figure accuracy could be found. The following method was developed giving an approximate comparison of the two different values.

While the two different units both quantify the figure accuracy, they do so in very different ways. Wave Error is a measure of how the height of the surface of the optical element varies as compared to the height of the desired shape. Slope error is a measure of how the angle of the surface of the optical element varies as compared to the angle of the desired surface shape. In order to compare them, an analytical

function was needed to describe the surface of the optical element, from which both the slope error and wave error could be extracted. A sinusoid was chosen for this function because the ray-tracing software that was used to model the spectrometers has the ability to superimpose a sinusoid onto an optical element to simulate an imperfect surface.

To begin with, a sine function was created with a wavelength equal to one tenth of each of the gratings surface dimensions. Ten periods across the grating was chosen as a reasonable starting value based on the advice of Dr. Reininger[26]. For the purpose of this calculation, a planar optical element was assumed. This allowed the magnitude of the sine wave to be taken as the deviation from the true planar geometry of the optical element. The angle of this function with respect to the axis is found by taking the inverse tangent of the derivative of the function. The RMS slope error could be extracted by integrating the square of this angle over the length of the optical element.

We begin with the sine function that will be overlaid to distort the surface of the optical element:

$$A \sin\left(\frac{2\pi}{\lambda} x\right)$$

where λ and A are the period and amplitude of this sine function. If we take an optical element of length ℓ, then by setting $\lambda = \ell/10$ we create a sinusoid with ten periods across the length of the element. The amplitude of the sinusoid, A, becomes the peak-to-valley deviation from that true shape.

The derivative of this sinusoid:

$$\frac{d}{dx}\left(A\sin\left(\frac{2\pi}{\lambda}x\right)\right) = \frac{2\pi}{\lambda}A\cos\left(\frac{2\pi}{\lambda}x\right)$$

gives us the slope of the surface of the deviated optical element, with respect to the true surface, for any point x along the optical element. The arctangent of this slope:

$$\arctan\left(\frac{2\pi}{\lambda}A\cos\left(\frac{2\pi}{\lambda}x\right)\right)$$

then gives the angular deviation of the optical surface from the true optical surface, at any point x along the optical element. If the square of the function is integrated along the length of the optical element, the root of the resulting value will be the RMS slope error of the element:

$$SE_{RMS} = \sqrt{\frac{1}{\ell}\int_0^{\ell}\left(\arctan^2\left(\frac{2\pi}{\lambda}A\cos\left(\frac{2\pi}{\lambda}x\right)\right)\right)dx} \tag{6.1}$$

By setting the amplitude, A, to half the wave error, the peak-to-valley height of the function is the same as the maximum wavefront error. Thus, Eqn. 6.1 provides a relationship between the wave error, $2A$, and the RMS slope error, SE_{RMS}. Inserting a wave error of $2A = \lambda/40$ (at 632.8 nm), the best achievable wave error that was quoted by some manufacturers, into Eqn. 6.1 results in an RMS slope error value of approximately $SE_{RMS} = 0.1$ arcseconds RMS. This value was quoted by other manufacturers as their best achievable slope error. Because these two values were quoted as the best achievable figure accuracies by two different but equally qualified manufacturers, this result was taken to be reasonable. From this, it is reasonable

to assume that Eqn. 6.1 provides at least a rough method of comparing these two different measurements of figure accuracy.

6.1.2 Modeling the Effects of Figure Errors

The above calculation allowed for approximate comparison of the quoted figure accuracies from various manufacturers. It was then desirable to determine the effects that different figure accuracies would have on the image produced by the optical element. As mentioned above, SHADOW has the capability to superimpose a sinusoidal deviation to modify the surface of an optical element. By using the period and amplitude (λ and A) from Eqn. 6.1, for the slope errors quoted by various manufacturers, the images shown in Fig. 6.1 were obtained. This figure shows the images formed at the detector by tracing rays of three different energies through our spectrometer design. Each energy forms a separate image of the entrance slit at the detector. The three different slit images seen in Fig. 6.1 become progressively less discernible as the slope error increases. This equates to a rapid decrease in resolving power as the slope error increases.

Even with the best achievable figure accuracy for a spherical grating (0.1" RMS), the resulting image is noticeably degraded as compared to a perfect optical element. A further reduction by about a factor of ten (1.1" RMS), which is the best some manufacturers can offer, causes so much diffusion that it completely destroys the image. As a side note, the best achievable slope error for a cylindrical grating is only about 1.0" RMS, which is the primary reason why cylindrical gratings are not feasible for this application. This will be discussed in detail in Section 7.1.

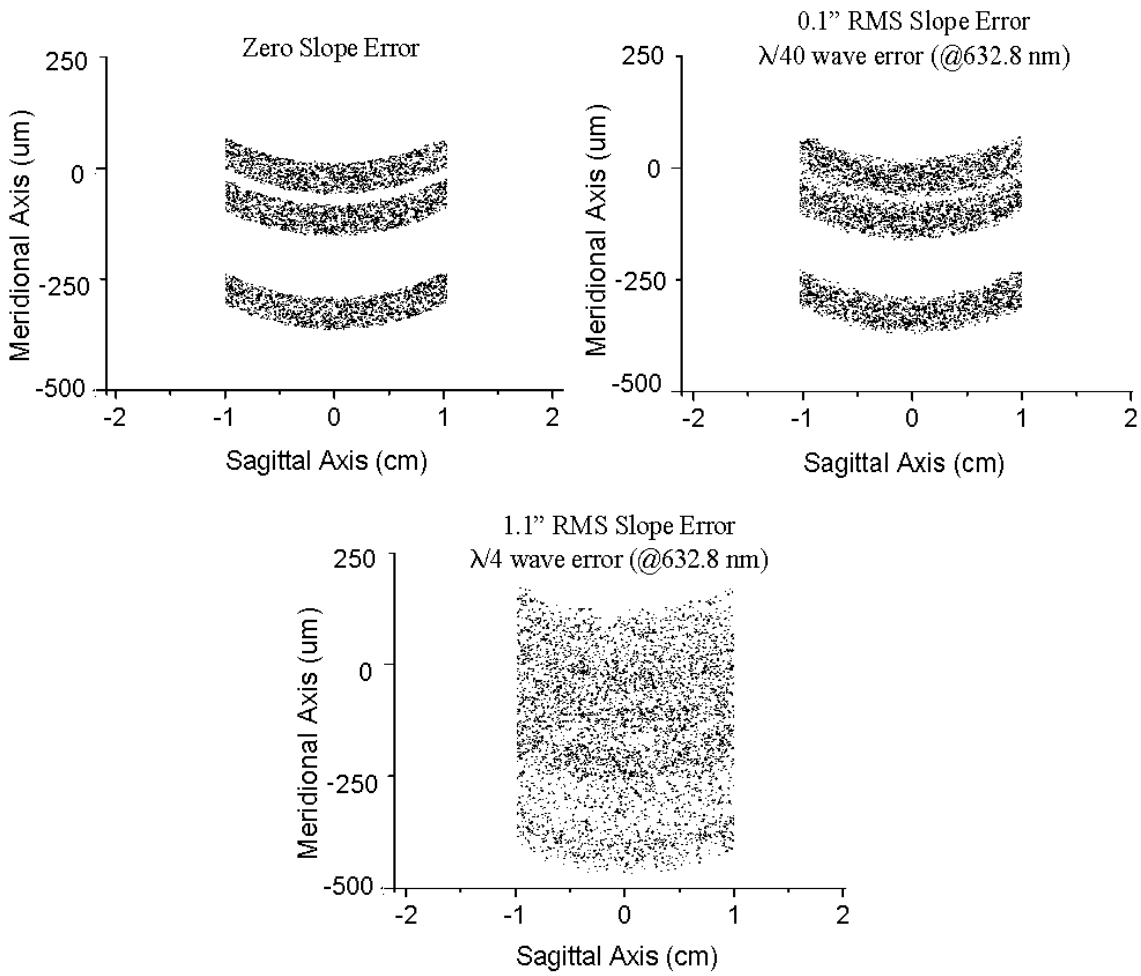

Figure 6.1: The effects of various levels of figure error on image quality. Each figure shows three different energy lines as they would appear at the detector. They are visually resolvable for a zero or 0.1" RMS slope error but are completely unresolvable for a 1.1" RMS slope error.

These calculations are, admittedly, far from rigorous. It is questionable whether these ray-tracings accurately represent the effects of a specific given figure error. However, it is reasonable to assume that they are sufficiently accurate to meaningfully compare the effects of figure errors that are an order of magnitude apart. From this it can be concluded that higher figure errors will strongly impact the resulting image quality. It is easy to conclude that, while the cost may be greater, the highest possible figure accuracy will offer substantial payoffs in terms of improved resolving

performance.

6.2 Efficiency Sensitivity

The diffraction efficiency is strongly dependent on the exact blaze profile of a diffraction grating. This is the most difficult parameter to control during the manufacturing process. As a result, the requested tolerance levels will not only have a significant effect on the price, but will also limit the number of suppliers with the technology and experience to successfully produce the required gratings. Fig. 6.2 shows the two parameters that define the profile of the grooves: the blaze angle and the anti-blaze (or apex) angle.

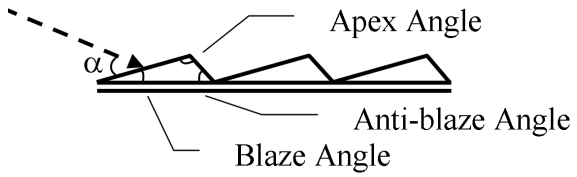

Figure 6.2: Parameters that define the groove profile

The blaze angle, as discussed in section 2.3.2, can be used to enhance the efficiency of the grating by controlling the angle that the incident light strikes and reflects off of the surface of the grooves. A series of calculations were performed to determine how dramatically variations in the blaze angle affect the diffraction efficiency. For each grating, the blaze angle was varied up and down until the diffraction efficiency was reduced by 15%. These were taken to be the acceptable manufacturing tolerance ranges. The acceptable range for the blaze angle was taken to be that which resulted in no more then a 15% loss in diffraction efficiency. The limits of these acceptable

ranges are given in Table 6.1, along with the optimum value. Most manufacturers typically quote a 10% accuracy for blaze angle reproduction through mechanical ruling. This will easily satisfy our needs as it will result in an approximate 5% relative efficiency loss, at most.

The diffraction efficiency is also closely tied to the incidence angle, α. The sensitivity of efficiency to this alignment parameter was considered using the same technique. Table 6.1 shows these acceptable ranges of incident angles as well as the optimum values. The acceptable ranges are given in terms of absolute value and percentage variations in each direction that would resulting in no more than a 15% relative loss in diffraction efficiency. As will be shown in Section 6.3, the resolving power is far more sensitive to this parameter than the diffraction efficiency is, therefore the incidence angles shown in Table 6.1 are not the limiting ranges for this parameter.

Table 6.1: Required blaze and incident angles that will result in an efficiency loss not greater that 15%

Grating Energy	Parameter	Optimum Value	Positive Limit	Negitive Limit
LEG	Incident Angle [°]	86	-3.85 (-4.5%)	0.95 (1.1%)
92 eV	Blaze Angle [°]	1.85	-0.55 (-30%)	0.55 (30%)
Impurity	Incident Angle [°]	87	-1.95 (-2.2%)	0.85 (1%)
285 eV	Blaze Angle [°]	1.21	-0.35 (-29%)	0.4 (33%)
MEG	Incident Angle [°]	88	-3.1 (-3.5%)	0.45 (0.5%)
410 eV	Blaze Angle [°]	1.485	-0.45 (-30%)	0.55 (37%)
XHEG	Incident Angle [°]	88	-1.25 (-1.4%)	0.7 (0.8%)
710 eV	Blaze Angle [°]	1.52	-0.7 (-46%)	0.3 (20%)

The design, as it stands now, calls for the anti-blaze angle to be 90 degrees, or a

true saw-tooth profile. Using most ruling techniques this is unobtainable. Grating efficiency calculations for varying anti-blaze angles were completed by Dr. Klaus Heidemann of Zeiss Optronics GmbH[29], one of our prospective grating suppliers. Table 6.2 shows the anti-blaze (and apex) angles that these calculations suggest would be required to prevent the efficiency from dropping by more than 10%. Even these angles are difficult to achieve by some techniques and this will limit the available manufacturing options.

Table 6.2: Range of anti-blaze and apex angles that will result in an efficiency loss not greater that 10%[29]

Grating	LEG	IMPURITY	MEG	HEG	HRMEG	HRHEG
Blaze angle [°]	1.85	1.11	1.49	1.52	4.2	4.05
Apex angle [°]	< 165	< 170	< 160	< 160	< 130	< 130
Anti-blaze angle [°]	< 13	< 9	< 19	< 19	< 46	< 46

6.3 Resolving Power Sensitivity

In order to explore the sensitivity of the resolving to a number of other parameters, a project was undertaken by Yann Disser, a German exchange student working with our research group, to explore the behavior of various design variables. This information will be useful not only for deciding the required manufacturing tolerances but also for determining the necessary level of accuracy that will be required in aligning the optical system. A series of ray-trace calculations were completed in which different parameters were varied in each direction until the resolving power of

the spectrometer dropped by 30%. The magnitude of the variation that results in a 30% drop in resolving power gives an indication of the sensitivity of the design to each parameter. The results of these calculations are shown in Table 6.3. For each parameter considered the optimum value is shown, along with the variations in each direction which result in a 30% loss in resolving power. Later consideration of each series of calculations showed some of the sensitivities to be erroneously high due to some naive assumptions, but useful information was gained from each. The various parameters considered and the information gained from each is discussed below.

Table 6.3: Tolerance ranges for various machining and alignment parameters. The limits reflect the deviation from the optimum value that results in a 30% loss of resolving power.

Grating Energy	Parameter	Optimum Value	Positive Limit	Negitive Limit
LEG 92 eV	grating line density [1/cm]	6000	+1250 (21%)	-900 (15%)
	grating radius [cm]	501.8	+1.35 (.3%)	-1.50 (.3%)
	image plane distance [cm]	72.6	+.35 (.5%)	-.30 (.4%)
	incidence angle [°]	86	+.04 (.05%)	-.03 (.03%)
	source plane distance [cm]	35	+.30 (.9%)	-.35 (1%)
Impurity 285 eV	grating line density [1/cm]	8000	+1750 (22%)	-1250 (16%)
	grating radius [cm]	668.8	+1.49 (.2%)	-2.01 (.3%)
	image plane distance [cm]	65.79	+.31 (.5%)	-.24 (.4%)
	incidence angle [°]	87	+.025 (.03%)	-0.02 (.02%)
	source plane distance [cm]	35	+.30 (.9%)	-.25 (.7%)
MEG 410 eV	grating line density [1/cm]	12000	+1900 (16%)	-1500 (13%)
	grating radius [cm]	1002.9	+1.62 (.2%)	-2.88 (.3%)
	image plane distance [cm]	92.24	+.31 (.3%)	-.19 (.2%)
	incidence angle [°]	88	+.02 (.02%)	-.015 (.02%)
	source plane distance [cm]	35	+.35 (1%)	-.20 (.6%)
XHEG 710 eV	grating line density [1/cm]	20000	+3000 (15%)	-2500 (13%)
	grating radius [cm]	1002.9	+1.62 (.2%)	-2.38 (.2%)
	image plane distance [cm]	90.74	+.31 (.3%)	-.19 (.2%)
	incidence angle [°]	88	+.02 (.02 %)	-.012 (.01%)
	source plane distance [cm]	35	+.35 (1%)	-.20 (.6%)

The first considered parameter was the line density. According to Table 6.3 the resolving power decreases even as the line density increases, a fact which seems counter-intuitive. The resolution should be proportional to the line density. However, in completing the ray-tracings for these tolerance calculations, only the parameter being considered was varied. This would simulate the effect of aligning and calibrating the spectrometer based on calculations that assumed the optimum line density when the grating in fact had a different line density. The resolving power drops off even as the line density increases because the focal field is curved and the detector is planar. The detector is placed tangential to the curved focal curve so only one point on the detector is truly in focus. Changing the line density changes the diffraction angle, which moves the image away from the focal curve-detector coincidence to a region of the detector that is poorly focused. This defocus overwhelms the increased dispersion resulting from the higher line density. The fact that the resolving power decreases faster as the line density decreases than it does as the line density increases is consistent with this effect. From this we can see that the system, overall, is not extremely sensitive to the exact line density, especially if the focal curve of the spectrometer is calibrated to the true line density of the grating. Since typical tolerances in ruled line densities are approximately 0.1%-0.3%[30], extraordinary efforts to tighten tolerances on this variable will not be required.

Grating radius was considered next. The resolving power drops extremely rapidly as the radius changes. As Table 6.3 shows, the resolving power will drop by 30% if the radius of curvature is off by even a fraction of a percent (0.2% - 0.3%). This was, again, a naive calculation in that all other parameters were held fixed as the

radius was changed. Changing the radius of the grating will result in a change in the focal distance which is not compensated for in these calculations, but it could be compensated for in the calibration of the instrument. The typical manufacturing tolerance for the radius of a spherical mirror is about 0.1%[30,31]. Variations of this magnitude in the true radius of the grating can be completely corrected for through proper alignment. This indicates that alignment will be made significantly easier if the true radius of the grating is known to a high precision.

Changing the radius of the grating will change the focal length of the spectrometer. A change in the radius of curvature of a grating of 0.3% results in the focal length changing by about 3-5 mm (0.3% - 0.4%). The sensitivity calculation for the focal distance shows that a deviation of approximately 3 mm will result in a 30% loss in resolving power. Locating the actual focal point with respect to the true radius of the grating will be a key step in achieving the desired performance from this spectrometer.

The source-grating distance and especially the grating incidence angle are also extremely sensitive. Any variation of these parameters will result in the three elements in the optical system moving off of the Rowland circle, effectively moving the focal plane away from the detector. In addition to defocusing the image, aberrations that are eliminated by a Rowland circle design will begin to appear, further degrading the resolving power. While these are not manufacturing tolerances for the gratings, they will become important when selecting the mechanical components that will be used to position and align the gratings and detector. Motion tables with high precision and repeatability will be a high priority.

6.4 Conclusion

From the calculation results presented in this chapter, it became clear that there are two important factors to focus on from the stand-point of grating manufacturing tolerances. To maintain high resolving power, the slope error of the grating substrates must be as low as can be reasonably achieved. To maintain high efficiency the blaze profile must be as close to a true saw-tooth profile as possible.

For an alignment and calibration, the system will be extremely sensitive to variations in the incidence angle. While the proper focal curve for any given incidence angle can be found, the key to a consistent high performance spectrometer will be in designing a mechanical system capable of highly accurate and repeatable angular grating alignment. Spatial positioning of the gratings and detector will require sub-millimeter accuracy which is easily achievable with off-the-shelf motion stages.

Part IV

Component Selection

and

Manufacturing

Chapter 7

Diffraction Gratings

Four factors determine the optical characteristics of a reflective diffraction grating: substrate geometry, groove geometry, line density and material. The material affects only the efficiency of the grating and is easily chosen with the aid of diffraction efficiency calculations. The spacing of the lines determines the angular dispersion of the grating. The spacing of the lines and the shape of the grooves impacts the grating efficiency. The substrate geometry primarily determines the focal characteristics of the optical element and is quite complicated. The design of the latter two elements, substrate geometry and groove geometry, are significantly restricted by the practicality of manufacturing the gratings. Their significance to the design and the impact of the various manufacturing processes available are discussed in this chapter.

7.1 Substrate Geometry

So far this document has assumed the use of spherical diffraction gratings, but this is not the only option available. Diffraction gratings can be made with a variety of geometries, the most popular of which include planar, spherical, cylindrical and

toroidal.

Plane gratings are typically not used in X-ray spectrometers due to their inability to focus or collimate the incident light. They would require additional optical elements to create a usable image. This is not practical due to the low reflection efficiencies in the X-ray regime which would lead to an unacceptable loss of photons. They do have a place in the design of monochromators where the use of a straight exit slit makes the curved image produced by a spherical grating less tolerable and the characteristics of a synchrotron source makes collimation unnecessary. Variable line-spacing can be used to create pseudo-focused plane gratings with imaging characteristics that lend themselves well to monochromator design.[32]

Cylindrical gratings are theoretically quite useful since the sagittal curvature of a spherical grating provides very limited collimation and results in much of the line curvature seen in the images produced. The drawback of cylindrical gratings, as was discussed in Section 6.1.2, comes from the fact that they are more complicated to produce and suffer from approximately 10 times the slope error of a similar spherical grating[33]. Slope error (typically quoted in arcseconds RMS) is a measure of the average angular deviation from the slope required to produce the desired "true" surface shape. Fig. 7.1 shows the difference in the image of a given source produced by typical spherical and cylindrical gratings. The greater slope error of the cylindrical grating results in the images of the entrance slit being significantly broader and more difficult to resolve.

Toroidal gratings can be used to create astigmatic images at the cost of severe energy dependent aberrations as the image is "collapsed" onto the focal plane. The

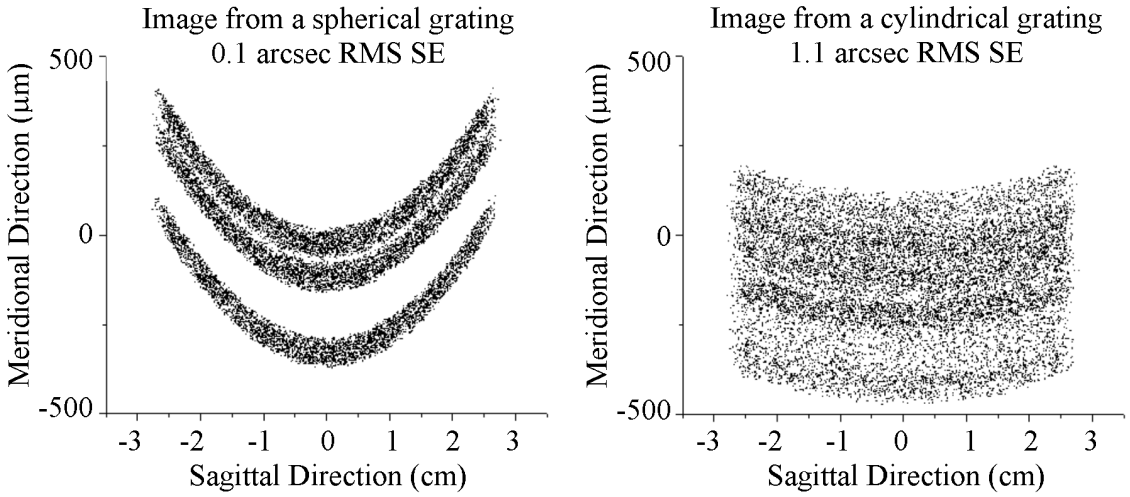

Figure 7.1: Comparison of images produced by spherical and cylindrical gratings, including expected manufacturing errors in surface geometry. While the line curvature is reduced by a cylindrical grating, the defocus resulting from increased figure error overwhelms and potential benefits.

net effect of an astigmatically corrected toroidal gratings is a marked reduction in resolving power.[34] Careful implementation of toroidal gratings can allow for larger gratings to be used without a significant increase in spherical aberrations.[35] However, due to limitations in manufacturing capabilities of this more complicated substrate geometry, the slope error in toroidal gratings is significantly higher. The reduced aberrations are replaced with image errors resulting from the higher surface errors of the optical element.

Spherical Gratings can be machined with extremely high accuracy with relative ease.[33] The inherent image errors of a spherical grating can be corrected for by using a 2D detector array and post-processing the acquired image. Other substrate geometries lend themselves to certain specialized applications. For a Rowland circle spectrometer, spherical gratings offer the most manageable balance of production precision and optical aberrations.

7.2 Ruling

There are two approaches to be considered for the ruling of diffraction gratings: holographic and mechanical. There are also a variety of post-processing options that can be used with each to achieve different effects. Each technique has advantages and disadvantages and the application and specifications of each grating must be considered to determine the best ruling method to achieve the goals of the design. Illustrations of the approximate profiles created by each combination of ruling and post-processing technique are shown in Fig. 7.2. Each of these techniques will be discussed in the following sections.

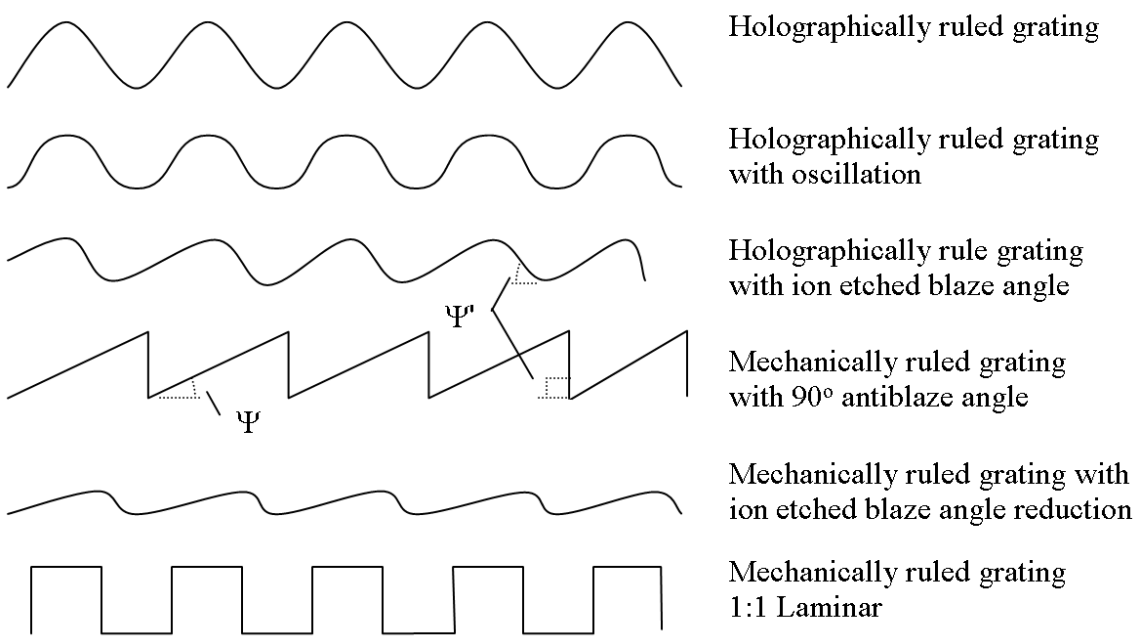

Figure 7.2: Diagrammatic comparison of approximate theoretical profiles created by various ruling techniques showing blaze (Ψ) and anitblaze (Ψ') angles . *Note: illustrative, not to scale.*

7.2.1 Holographic

Holographic ruling is achieved by exposing a photoresistive substrate to a laser-produced interference pattern. By selecting the laser wavelength, and controlling the placement of the lasers, very nearly regular and parallel line patterns can be produced. Holographic ruling is the faster of the two techniques, requiring a relatively short set-up and exposure time to produce the grating. Holographic gratings also tend to be smoother (have less micro-roughness) than ruled gratings.[26]

The major disadvantage of this technique is that it allows for very little control over the profile of the groove produced. The inherent sine-squared intensity of the interference pattern results in sinusoidal groove profiles, as shown in Fig. 7.2, that are far from optimum for efficient diffraction. This profile can be improved by post-processing the grating with techniques such as ion-etching but this is not as accurate or as flexible as mechanical ruling and it is very difficult to achieve blaze angles below 3 degrees. If laminar (rectangular) grooves are desired, they can be closely approximated by oscillating the photoresist during exposure so that the intensity peaks spend more time near the edges of the grooves.

The nature of the interference pattern produced restricts the line patterns that can be produced. Parallel, constant line density groove patterns can be closely approximated. Some level of spherical abberation correction for a given energy can be accomplished by careful placement of the holographic sources at the appropriate locations on the Rowland circle.[36] Holographically ruled VLS gratings can be produced to customize the focal curve of the spectrometer, though not with the flexibility of

mechanically ruled gratings.[4]

Due to the single exposure production technique, the cost of holographic gratings does not scale with grating size. Since each groove is not individually ruled, higher line density gratings are not more expensive and greater densities are obtainable through holographic techniques than through mechanical ruling. However, lower line densities and lower blaze angle increase the complexity of the process and therefore the price.

7.2.2 Mechanical Ruling

Mechanically ruled gratings are manufactured using complex precision ruling engines that drag a diamond-tipped stylus across an optical blank, ruling each groove individually. This is an exacting and time consuming operation often taking on the order of weeks to rule a single grating. Any interruption in the process can result in the loss of the grating.

The advantage of this technique is the high level of control afforded over the line density and groove profile. Design of the stylus tip grants a large degree of control over the groove profile. Parallel grooves can be ruled with greater accuracy than holographic approximations. Variable line-spaced gratings can be produced to meet any requirement for focal field and aberration correction limited only by the precision and accuracy of the ruling engine.

One grating manufacturer, Carl Zeiss Laser Optics GmbH, finds that superior results can be obtained for very low blaze angle groove profiles using a two step process. They begin by ruling a higher blazed angle and then they use an ion-

etching technique, similar to that used in holographic processes, to reduce the blaze to the desired angle. This approach does not result in a 90 degree blazed profile but the so called anti-blazed angle (Ψ', the angle of the surface opposite the one that on which incident rays fall, see Fig 7.2) is sufficiently high that the grating efficiency is nearly unaffected.[33] Carl Zeiss states that in order for the efficiency to be unaffected by the anti-blaze angle, it must be at least three times greater than the blaze angle. Our calculations show about a 5% loss in efficiency for this case.

7.2.3 Conclusion

Due to our desire to maximize efficiency, a carefully controlled low blaze angle is required. This overriding requirement makes mechanically ruled gratings significantly more attractive than holographically ruled gratings for our application. If mechanical ruling followed by ion etching will provide more accurate blaze angles than this is an approach worth considering. For our extreme resolution gratings, due to their very high line density, holographic gratings may be more cost effective. Since these gratings both require blaze angle above 3^o (4.1^o and 4.9^o), acceptable blaze profiles can feasibly be produced with this method followed by ion etching.

Chapter 8

Detector Selection

There are two technologies to choose from for soft X-ray area detectors: Multi-Channel Plates with Resistive Anode Encoders (MCP/RAE) and Charge Coupled Devices (CCD). Each has unique advantages and disadvantages which must be carefully considered in selecting the best detector for a particular application.

Multichannel plates (see Fig 8.1) are devices formed by boring a grid of microscopic channels through a substrate such as glass and then coating these channels with a resistive layer, turning each channel into an electron multiplier tube.[37] The surface of the plate is typically coated with a material such as CsI or MgF_2 to increase the number of electrons produced by an incident photon, which increases the efficiency of the device. The MCP is biased to prevent electrons generated in the coating from escaping the plate and to reduce the amount of drift between channels. Two or more MCPs can be stacked with channels at opposing angles (called a chevron or Z plate) to increase gain and eliminated the possibility of a photon passing through without striking a channel wall. On the back of the plate is a resistive anode sheet detector. The Resistive anode allows for the measurement of the position of the electrons emitted from the channels of the MCP by determining the

location at which the charge accumulates along each edge. This signal is digitized to produce the output.

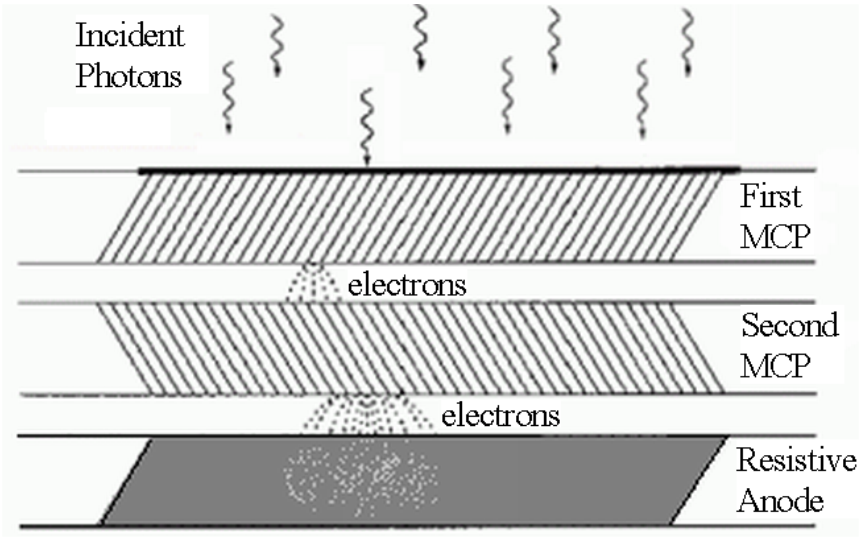

Figure 8.1: Anatomy of a Multi-Channel Plate(MCP). Incident photon strike the surface of channels bored through the plates and create electron cascades. The position of the electrons that emerge from the bottom of the plates is determined with a resistive anode and encoder.

Charge coupled devices (see Fig 8.2) are semiconductor devices that essentially consist of an array of capacitors, each forming a pixel, that are biased to collect the electrons that are ionized when an incident photon strikes the detector. Unlike MCPs, which detect individual incident photons, CCDs operate in an integrating detection mode. The accumulated charge in each pixel is periodically read out sequentially by "coupling" rows of pixels to shift the accumulated charges across to circuitry that quantifies and digitizes it, thereby determining the number of incident photons that arrived at that pixel. CCDs have the disadvantage of being sensitive to radiation damage when used for direct imaging of X-rays. Modern CCDs designed expressly for this purpose have significantly reduced this problem by incorporating shielding for sensitive components.[38]

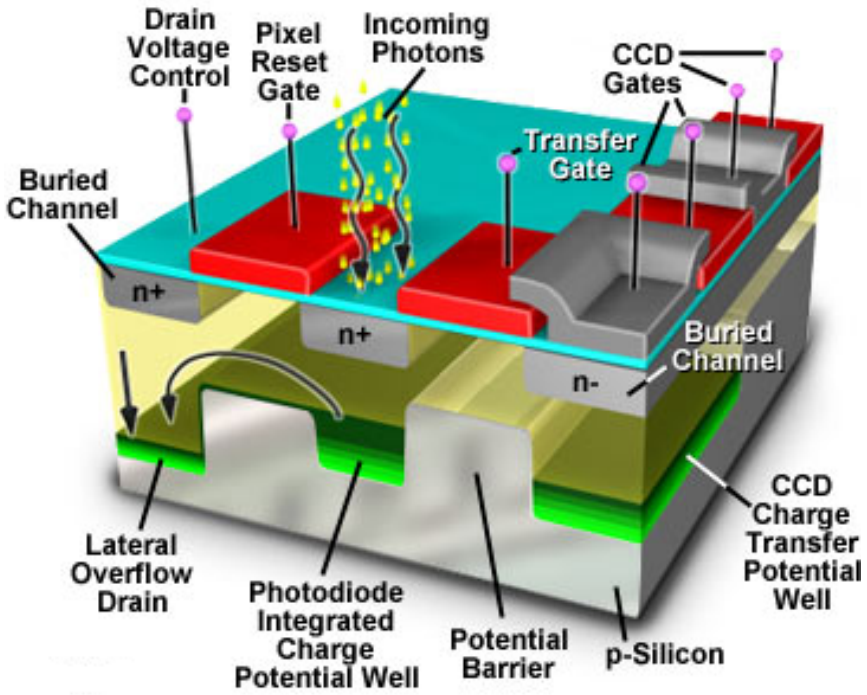

Figure 8.2: Anatomy of a Charge Coupled Device.[39] Incident photons generate electrons that are trapped in an array of photodiodes. These trapped charges are periodically read out by encoding circuitry that each row of electrons is transferred to via charge coupling of adjacent rows.

The advantages and disadvantages of each type of detector, as they relate to our emission spectrometer design, will be discussed on a point by point basis in the following sections.

8.1 Resolution and Spectral Windows

One of the most significant factors in choosing a detector system for a spectrometer is the impact it will have on the resolution and visible spectral window. The resolving power of a spectrometer is inversely proportional to the pixel size. Smaller pixels allow for finer spectral details to be resolved. The visible spectral window of a

spectrometer is the energy range that can be collected in a single exposure, without moving the detector. This is determined by the length of the detector along the dispersion direction. These two characteristics are in competition as the total size of the detector and the size of each pixel are related. Generally speaking, as the size of the detector increases the size of each pixel also increases. This creates a trade-off in that increasing the spectral window reduces the resolving power of the system. In addition to this, CCDs and MCPs use very different approaches to digitizing the image formed on them and, as such, it is not easy to compare their imaging characteristics directly.

Charge coupled devices are the simplest to understand in terms of resolution. Since they are composed of an array of pixels that are read out individually the spatial resolution of the detector is directly related to the size of each pixel. Soft X-ray CCD arrays are currently limited to a maximum size of about 2.7 cm on a side and are available from Princeton Instruments[38] in 13.5 μm and 20 μm pixel sizes in arrays of 2048x2048 and 1340x1300 respectively. Similar configurations are available from Andor Technology[40].

Multichannel plates designed for soft X-ray detection are available in high and low resolution versions from Quantar Technology[41], having 100 and 400 channels per axis respectively. Since the incident photons are converted to electrons in a coating, photons that strike between channels can send electrons down multiple channels. This allows for the resulting charge location on the resistive anode to be digitized to a higher precision than the channel spacing. Quantar suggests sampling at at least twice the physical resolution of the MCP and offers anode/encoders with 1024

channels per side. MCPs can be custom manufactured to almost any desired size. For the sake of comparison, we can consider a 2.7 cm MCP, the same size as a typical CCD. A high resolution 400 channel MCP would yield a physical channel spacing of 70 μm. This would be encoded to 1024 channels giving a theoretical resolution of about 27μm. However, residual charges on the anode from previous incident photons introduce errors known as position jitter. The effect of position jitter on the computed spatial position results in the resolution seen experimentally being, at best, twice the theoretical 27μm value. This gives an effective pixel size of about 50-60 μm.[37,42] Fig. 8.3 shows the effect of the pixel sizes on the resolving power of our spectrometer design. The lower effective resolution of an MCP detector significantly impairs the resolving power of the spectrometer.

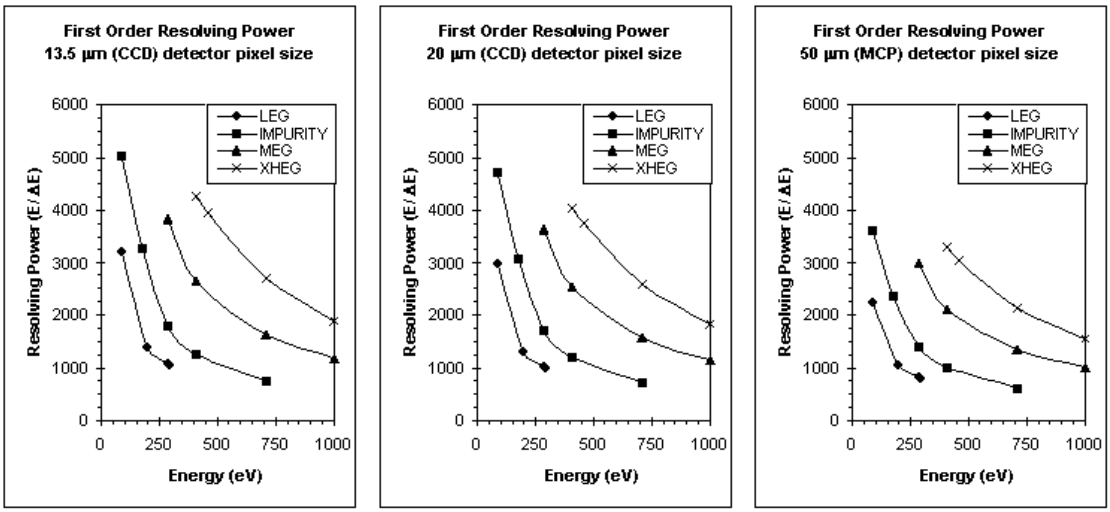

Figure 8.3: Effective resolving power of our base gratings with various detector pixel sizes. While little changed is seen between various sized CCD pixels sizes (13.5 μm and 20 μm, a significant reduction in resolving power is apparent while moving to a typical MCP detector (50 μm)

The drawback of high resolution detectors is their small area which results in a

narrow spectral window. MCP detectors have the advantage of being available in any desired size, though a larger area comes at the cost of lower resolution. Table 8.1 compares the spectral window size, in eV, of typical CCD and MCP detectors over the energy ranges of each grating in our design. For the majority of the spectrum the CCD energy window is more than sufficient. A difficultly arises at the low end of the energy range of the Impurity and LEG gratings. For these regions, the spectral window drops below 10 eV which may be insufficient for collecting a complete near-edge emission spectrum.

Table 8.1: This table shows the range of energies (spectral window) that two different sized detectors would be able to collect at either end of the energy range of each grating in our base design.

	2.76cm Detector (13.5um CCD)		4.0cm Detector (80um MCP)	
	Energy (eV)	Window (eV)	Energy (eV)	Window (eV)
Impurity	92-710	5-154	92-710	8-222
LEG	92-285	9-63	92-285	13-86
MEG	285-1000	16-121	285-1000	23-175
XHEG	410-1000	21-88	410-1000	31-127

Ray-trace simulations were completed to explore an alternative to trading away the high resolution of a CCD detector across the whole energy range to gain a broader spectral window at low energies. These calculations showed that it is possible to increase the spectral window by turning the detector off-tangent to a lower incidence angle. As is illustrated in Fig. 8.4, rotating the detector off-tangent has the effect of increasing the effective cross-section of the detector allowing it to see a larger spectral window.

There are two drawbacks to this approach. The first is that in order to fit a larger energy range onto the detector, the spatial dispersion is necessarily reduced, resulting

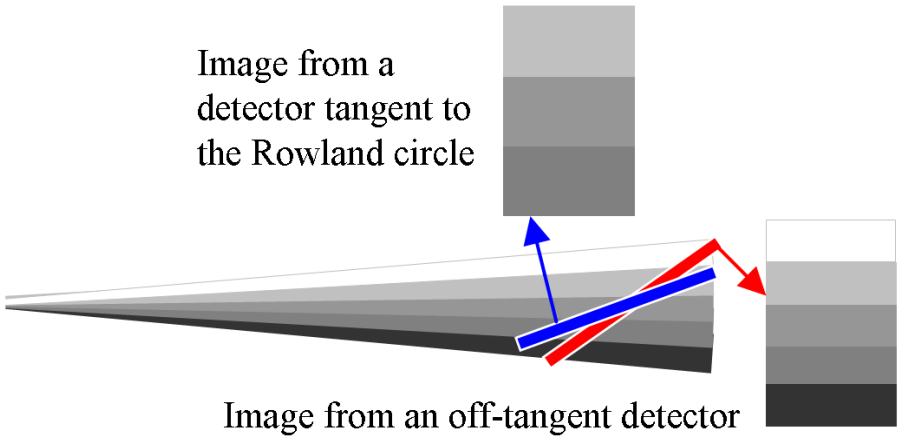

Figure 8.4: Illustration of the effects of rotating the detector off-tangent. A rotation by a few degrees results in the increased effective detector cross-section. This allows the detector to see a larger spectral window, but with reduced energy dispersion and some defocusing towards the edges of the detector.

in decreased resolving power. The second drawback is that when the detector is off-tangent, only one point on the detector can coincide with the focal curve and defocusing effects will appear along the rest of the detector. This effect can be seen graphically in Fig. 8.5. The figure shows 8 spectral lines a different energies in the range of 86-100 eV, as they appear on a 2.7 cm detector after being dispersed by our LEG. The left hand side shows that a detector tangent to the Rowland circle would see only the lines falling within the 88-96eV range but with a uniform resolving power of 3000 over that range. The off-tangent detector, shown on the right, can see the full range but with reduced line separation and increased broadening of the lines further from the center of the detector which results in a resolving power that decrease from 2600 at the center of the detector to 700 at the edge.

Moving the detector off-tangent can result in a dramatic decrease in resolving power at the edges of the spectral window. This is still more tolerable than reducing

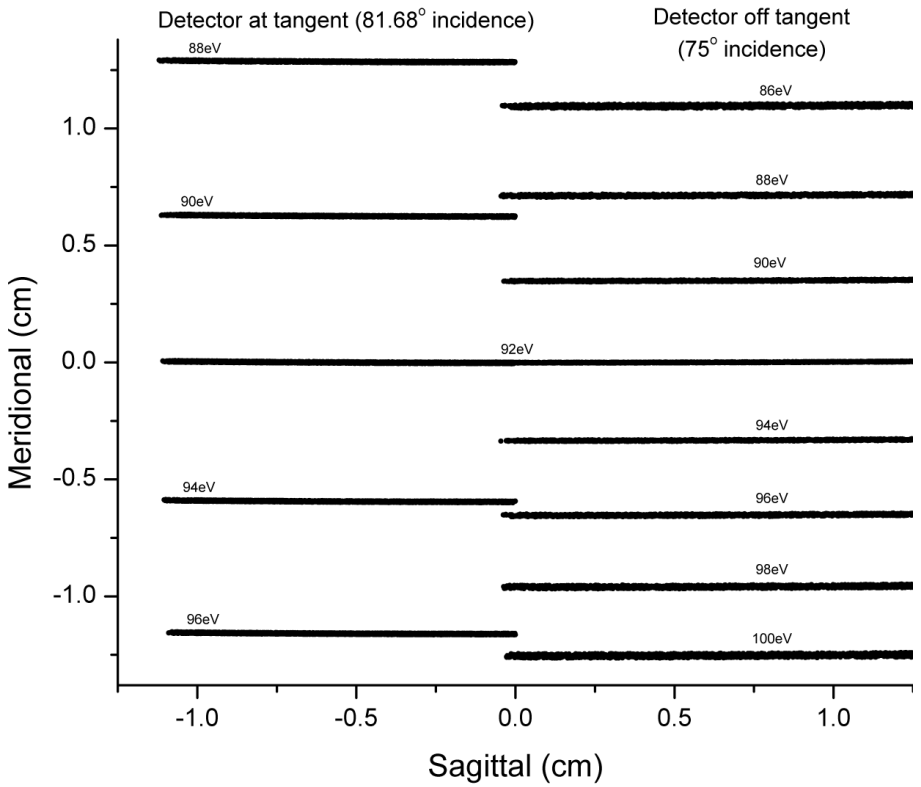

Figure 8.5: Eight spectral lines a different energies in the range of 86-100 eV, as they appear on a 2.7 cm detector. **Left:** a detector tangent to the Rowland circle would see only the lines falling within the 88-96eV range. **Right:** the off-tangent detector can see the full range but reduced line separation and increased broadening of the lines further from the center of the detector due to refocusing is apparent.

the resolving power of the spectrometer over the entire energy range due to a number of factors. In most cases the greatest detail and the features of interest will be located near the center of the spectral window, where the resolving power is highest. The loss in resolving power at the edges of the detector is proportional to the amount by which the detector is rotated. The degree of rotation can be kept low by providing only the spectral window required, minimizing resolving power losses. Finally, the energy ranges where the spectral window is smallest are the ranges with the highest resolving power so the sacrifices that need to be made to increase the spectral window

can be afforded.

8.2 Quantum Efficiency and Background Noise

Since the detectors operate on such different principles, their efficiency and noise characteristics need careful consideration. The quantum efficiency is the fraction of photons incident on a detector that are effectively converted into a usable signal. At normal incidence the behavior of these detectors is well known. MCPs typically see quantum efficiencies at normal incidence of, at best, 30%[37] whereas CCDs can achieve 50-80%[38] in the 100-1000 eV range. At grazing incidence, however, the performance of a CCD falls off much more quickly than it does for a MCP. This is because the penetration depth of soft X-rays is very low and at grazing angles the path length through the substrate material to the sensitive layers of a CCD becomes significant. At grazing incidence the quantum efficiency of a CCD is reduced to around 20% whereas the quantum efficiency of a MCP falls to about 15% making their relative performances quite comparable.[43]

MCPs tend to have very good signal to noise ratios. The number of electrons produced at the surface of the detector by a high energy (soft X-ray) photon results in an electron pulse on the anode that is significantly larger than that generated by thermal electrons or optical photons. This allows these source of noise be to easily filtered out by the detector electronics.[37] The disadvantage of MCPs is that since they operate in a single photon counting mode they can be more easily saturated. Modern electronics have pushed this limit past 100,000 counts/s[41] and this is not

typically a limiting factor for most soft X-ray emission studies.

CCDs, as integrating detectors, are much more sensitive to thermally generated electrons (dark current) since they build up over the duration of the exposure. This can be significantly reduced by cooling the CCD, either cryogenically or thermoelectrically. The latter is quite effective and is very easy to implement and maintain.[38] CCDs also offer no way of distinguishing between optical photons and soft X-rays. This requires that steps be taken to ensure that the detector housing admits as little stray light as possible.

8.3 Time Resolution and Source Synchronization

Synchrotron radiation is not produced in a continuous stream. The electrons that travel through the storage ring and produce the photons used by the experimental beamlines travel in a pulse-train, in groupings called bunches. These bunches are typically on the order of tens or hundreds of microseconds apart, depending on the operating mode of the synchrotron. The light that results from these discrete bunches arrives in structured pulses. This structure can be taken advantage of to further reduce noise and extraneous signals by only acquiring data while the sample is actually illuminated by the light from a passing pulse-train. MCPs are single-event-counting detectors which allows for easy activation and deactivation of the data acquisition with a timing signal from the synchrotron control systems. Because CCDs are integrating detectors and have lengthy readout times this approach is not feasible. This can substantially reduce the sensitivity to both dark currents

and visible light contamination by keeping the detector "off" while not acquiring meaningful data.

An additional use of the signal structure of this source is to conduct time resolved experiments. The travel time around the ring for a bunch is on the order of $\sim$500 μs. With only one bunch in the synchrotron ring a light pulse is produced with that periodicity. This can allow the excitation-decay process of systems that have relaxation times on the order of $\sim$500 μs to be studied when the facility is operated in a single-bunch mode. Experiments of this nature may be of interest in the future once the CLS has refined its control systems to the point where a clean single-bunch can be produced and maintained. CCD encoding electronics can be designed to allow the CCD array to be electronically "shuttered" by continuously bleeding the accumulated signal (noise) off the detector until triggered when a pulse train passes. Because of this, either detector system may be capable of the shuttering necessary to accomplish this, though the time resolution of a MCP detector may be superior.

8.4 Other Considerations

At the time this document was written, CCDs cost substantially more than MCPs, typically at least twice as much. This can become a significant concern when the delicate nature of these detectors is considered. Damage and wear in the course of normal operation is a real possibility and replacement may be occasionally required. MCPs have an advantage in that they have independently replaceable detector head where as the entire CCD camera would need to be replace if it were damaged.

CCD detectors are considerably more bulky than MCPs, as the detector and electronics are packaged together (see Fig. 8.6. This can make mechanical integration more difficult and it restricts grazing incidence use. As can be seen in Fig. 8.6, a standard packaged PI-SX CCD cannot be used at grazing incidence at all. Specially modified versions of this detector, with the CCD mounted flush to the flange, are available but the structure of the CCD chip itself can still interfere at very low incidence angles.[38]

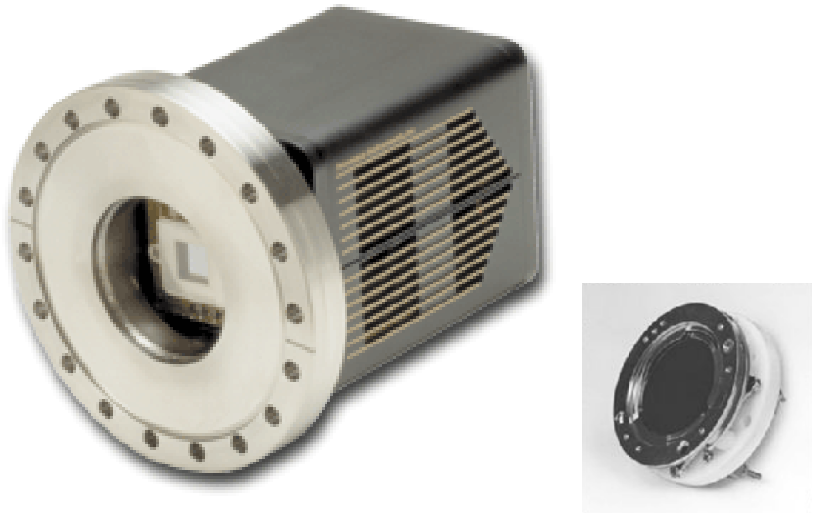

Figure 8.6: A typical CCD and MCP detector, shown roughly to scale. Left: a Princeton Instruments PI-SX CCD camera.[38] Right: a Quantar 3300 Series MCP Detector Head.[41]

8.5 Conclusion

CCDs are superior to MCPs in terms of resolution and quantum efficiency. MCPs have advantages in terms time resolution and spectral window size. CCDs suffer from a reduced spectral window due to their small detector areas, though this is not a concern over most of the spectral range of this instrument. MCPs are better able to

filter out unwanted noise and signals from visible photons. CCDs require the added complication of a cooling systems reduce noise due to dark currents. MCPs are easily capable of source synchronization whereas CCDs, practically, are not. With all of these factors in mind, and considering the better cost point of MCP detectors, an MCP detector will be used for this system.

Chapter 9

Mechanical Design

9.1 UHV Design Issues

A key factor in the design will be the necessity that the components be UHV-compatible. This will impose severe limitations on both the types of materials used and the mechanical design. Many common construction materials and electrical components, even some metals, are not UHV compatible due to their high vapor pressures. This can result in the components degassing (releasing gaseous particles into the chamber) and compromising the vacuum. A number of the components in the system, including the grating manipulator stage, can be purchased from UHV supply companies. Determining the exact specifications required for these components and selecting the most economical and flexible commercially available solution will be an involved task. The mechanical design of the custom components must take into account the UHV environment since improper design can result in trapped gas pockets that leak into the vacuum and significantly increase the time required to pump a chamber down to UHV. Finally, the mechanical components must function without lubricants as these would vaporize and compromise the vacuum as well.

This will require stringent component tolerances, and careful design and it will make reliability more difficult to achieve. Due to the time required to pump a chamber down to UHV, any failure that requires the chamber to be opened for repairs results in significant loss of operating time, making reliability a chief concern.

9.2 Grating Motion Stage

Because precise grating alignment and optimization are critical to ensure acceptable performance of the spectrometer, careful attention will be paid to the grating mounting system. This task will most likely be completed in collaboration with a mechanical engineering firm. Some preliminary research has been completed into possible mounting methods for the gratings. Dr. Giacomo Ghiringhelli of Politecnico di Milano Technical University has recently completed commissioning a specialty soft X-ray spectrometer. On his advice we have investigated a series of UHV motion stages from MICOS GbmH[44], a selection of which are pictured in see Fig. 9.1. In order to ensure repeatable and precise optimization and alignment of each grating, some combination of precision motion stages allowing two or three degrees of translational positioning and one or two degrees of rotational motion will be required. Motion stages are available with a variety of drive motors and control systems to achieve almost any level of alignment precision that may be required. This will allow for easy grating selection and optimization in vacuum.

Figure 9.1: MICOS UHV precision motion stage that can be combined for any required number of degrees of freedom.[44] Left to right: Goniometer stage, Linear stage, Lifting Stage

9.3 Additional Tasks

Additional tasks that need to be completed include the design of a vacuum chamber to house the gratings, selection or design of an adjustable entrance slit and design of the vacuum bellows and motion system for positioning of the detector. Design of the vacuum chamber will be a relatively simple task once the demands of the entrance slit and motion stages are known. Any one of a number of vacuum design firms should be able to handle the engineering of a chamber to meet our specifications. Preliminary research is underway into available entrance slit designs. Negotiations are currently underway to have the design of the grating and detector motion stages completed with the assistance of an engineering firm in an industrial collaboration.

Part V

Conclusion

Chapter 10

Conclusion

The goal of this project was to select or design a soft X-ray emission spectrometer for the REIXS beamline at the Canadian Light Source. The parameters of this project required a spectrometer with superior resolving power and good efficiency throughout an energy range of 90 eV - 1100 eV. Specific attention was to be paid to particular emission energies of interest (Si $L_{2,3}$ at 92 eV, C $K_{1,2}$ at 280 eV, N $K_{1,2}$ at 400 eV and O $K_{1,2}$ at 525 eV). Existing spectrometer designs were considered and analyzed before a decision was reached to design a spectrometer of our own to meet these requirements.

Careful analysis of the existing soft X-ray emission spectrometers and an understanding of the theory of their operation revealed and explained the strengths and weakness of each. This understanding was exploited to incorporate these strengths into our design while focusing on optimizing it to the particular requirements of the project. In so doing, significantly improved resolving powers were achieved while maintaining good diffraction efficiencies throughout the energy range of interest of the design. This was possible due to a software suite unique to our research group which allowed for the careful balancing of diffraction efficiency and resolving power

to achieve unprecedented performance. As a result, the originally targeted performance was significantly exceeded, not only at the specific energies of interest, but across the entire spectral range of the spectrometer.

Considerable knowledge was gained in designing a spectrometer to meet the requirements initially set out for this project. This led to the proposition of an experimental design that uses the third diffraction order to exploit performance peaks found in the optical characteristics of available materials. This design provides an effective way of trading diffraction efficiency to achieve resolving powers a factor of two to three times higher than our base design throughout the upper end of the energy range. No existing design comes close to providing such resolving powers for these soft X-ray energies.

This spectrometer will offer users a choice of two or more gratings and/or diffraction orders throughout most of the energy range of the design, allowing the selection of the best combination of efficiency and resolving power for a particular experiment. If the novel third order design is implemented it will be able to provide unheard of resolving power throughout the higher end of the spectral range of the design. If the gratings of the basic design have access to the detector motion required for the third order design this impressive performance will extend throughout the entire energy range.

Having successfully completed the initial goals of the project, research began into the selection of components required for this spectrometer to ensure that the predicted performance could be realized. Extensive discussions with suppliers of diffraction gratings and detectors provided the understanding and information re-

quired to choose appropriate technologies and manufacturing techniques. Based on the information gathered, the gratings, as described in this document, have been ordered. Work is underway on the mechanical design of the UHV chambers and mounting systems for the gratings and detector that will allow for the precise alignment required to achieve the predicted performance.

When completed, this instrument will provide the REIXS beamline at the Canadian Light Source with an endstation that sets the standard of performance for soft X-ray emission spectrometers.

Part VI

Appendices

Appendix A
Definition of Variables

Table A.1: Definition of Variables

ξ	Grating coordinate, perpendicular to the grating surface
ω	Grating coordinate, along the diffraction direction (meridional directional)
ℓ	Grating coordinate, perpendicular to the diffraction diffraction (sagittal direction)
x, y, z	Position with the coordinate system of the optical element
z	Sagittal offset of source ray relative to grating origin
x', y', z'	Position within the coordinate system of the focal plane
z'	Sagittal offset at focal plane relative to grating origin
N	Grating line density
N_0	Grating line density at the origin of a VLS grating
σ	Grating line spacing (N^{-1})
σ_0	Grating line spacing at the origin of a VLS grating(N_0^{-1})
k	Diffraction Order
λ	Incident wavelength
E	Incident energy
Ψ	Grating blaze angle
Ψ'	Grating anti-blaze angle
α	Grating incidence angle, w.r.t. surface normal
$\beta(E)$	Diffraction angle, w.r.t. surface normal
r	Source-grating distance
r'	Grating-focal plane distance
R	Grating radius
b_i	VLS polynomial coefficients
F_{nm}	Terms of the optical path function expansion
s	Entrance slit width
d	Detector pixel size

Appendix B

Detailed Performance Comparison Plots

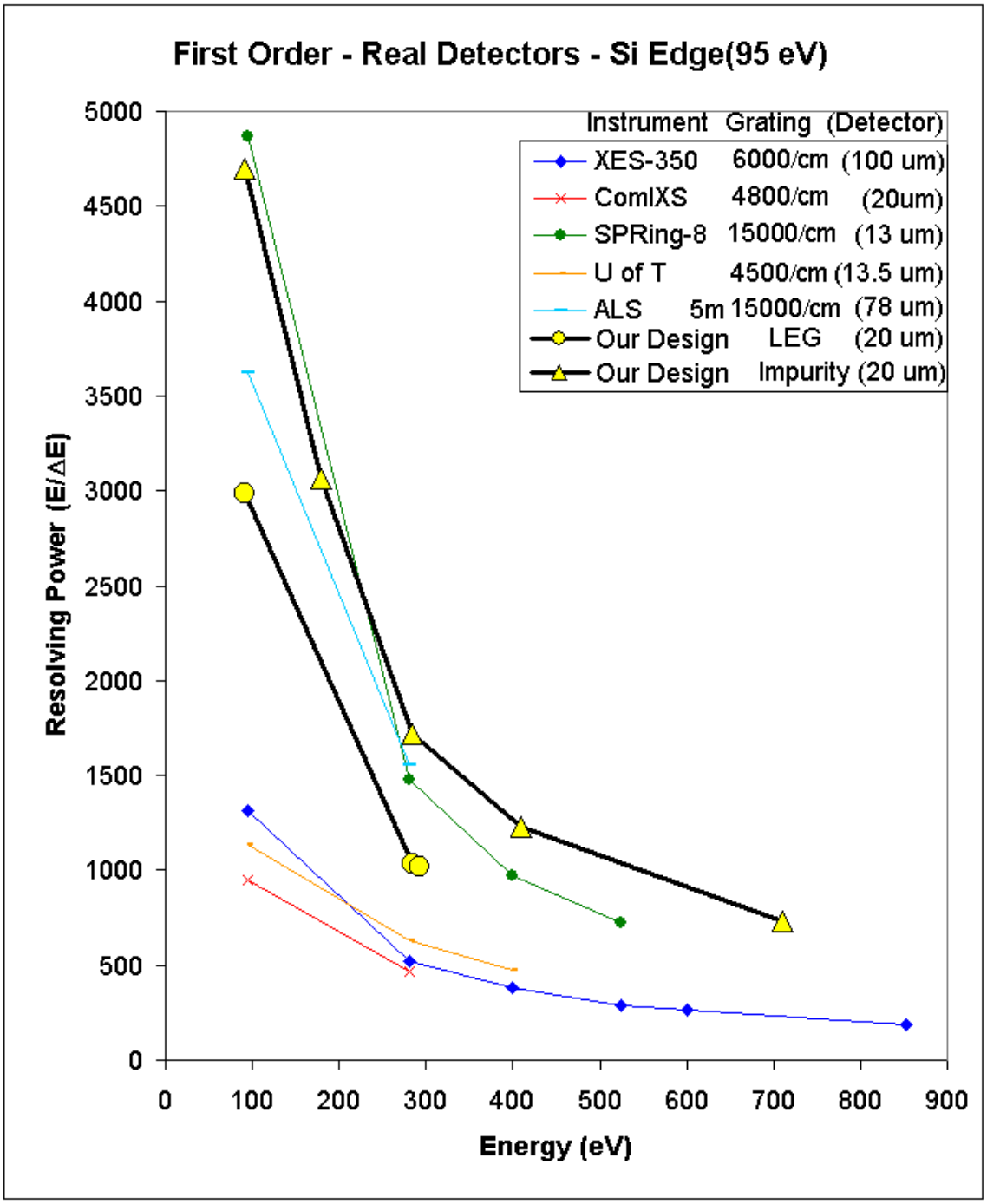

Figure B.1: Comparison of our design to existing spectrometer designs with their original detectors. Capabilities of each system are shown at the Si $L_{2,3}$ emission edge. The legend specifies the spectrometer, grating (size and/or line density) with the detector pixel size in parentheses.

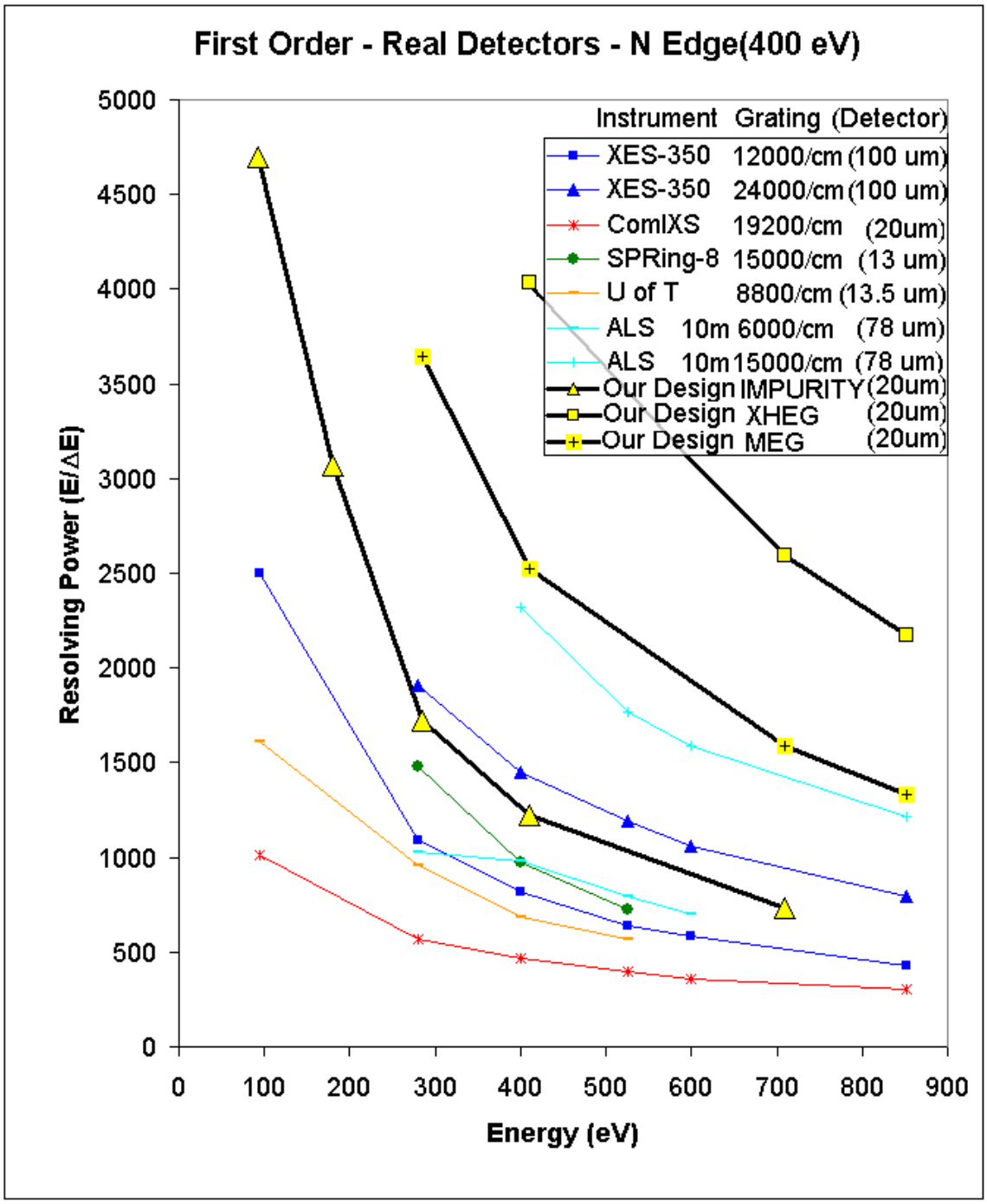

Figure B.1 ***(cont.)*****:** Comparison of our design to existing spectrometer designs with their original detectors. Capabilities of each system are shown at the N $K_{1,2}$ emission edge. The legend specifies the spectrometer, grating (size and/or line density) with the detector pixel size in parentheses.

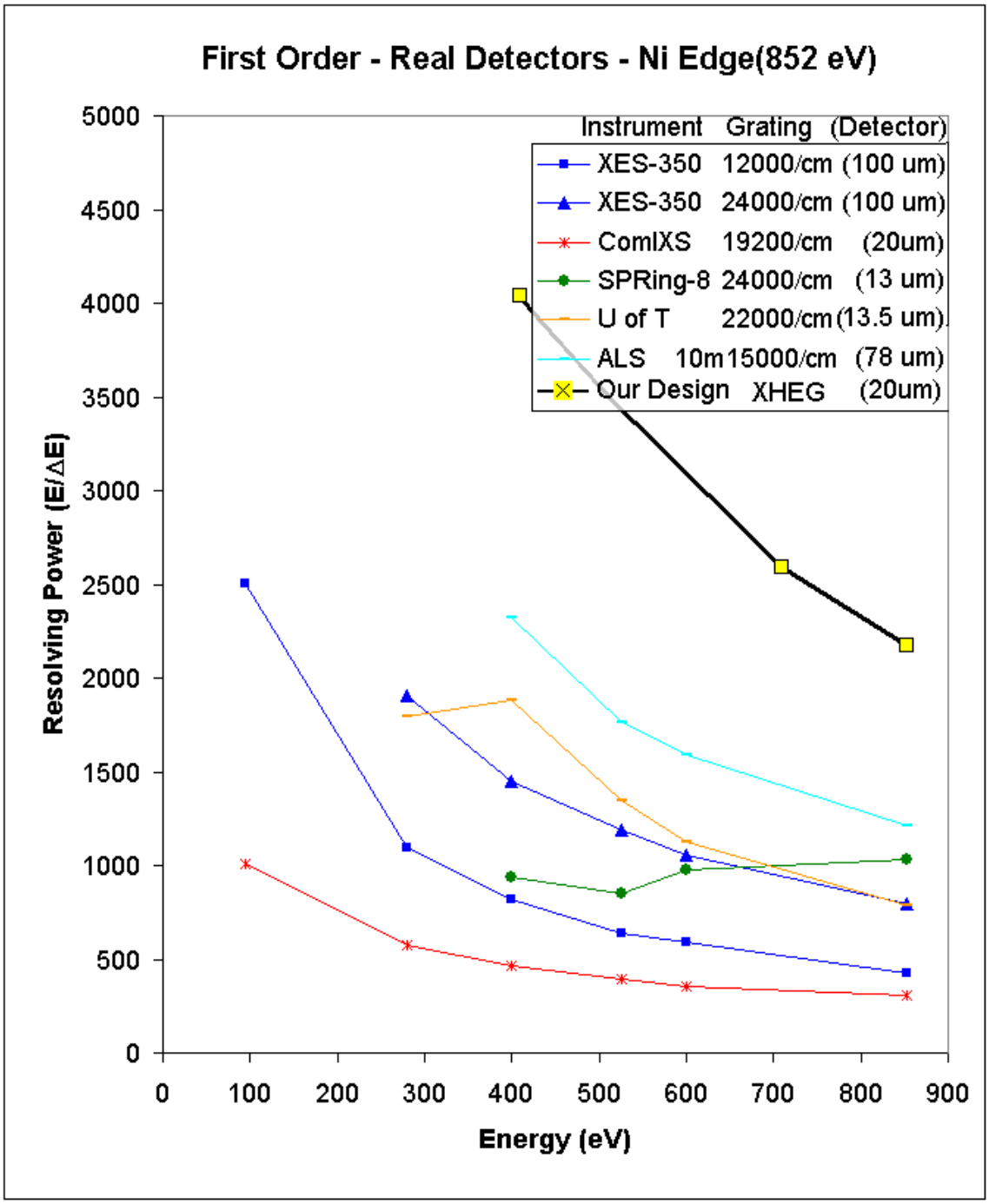

Figure B.1 ***(cont.)*****:** Comparison of our design to existing spectrometer designs with their original detectors. Capabilities of each system are shown at the Ni $L_{2,3}$ emission edge. The legend specifies the spectrometer, grating (size and/or line density) with the detector pixel size in parentheses.

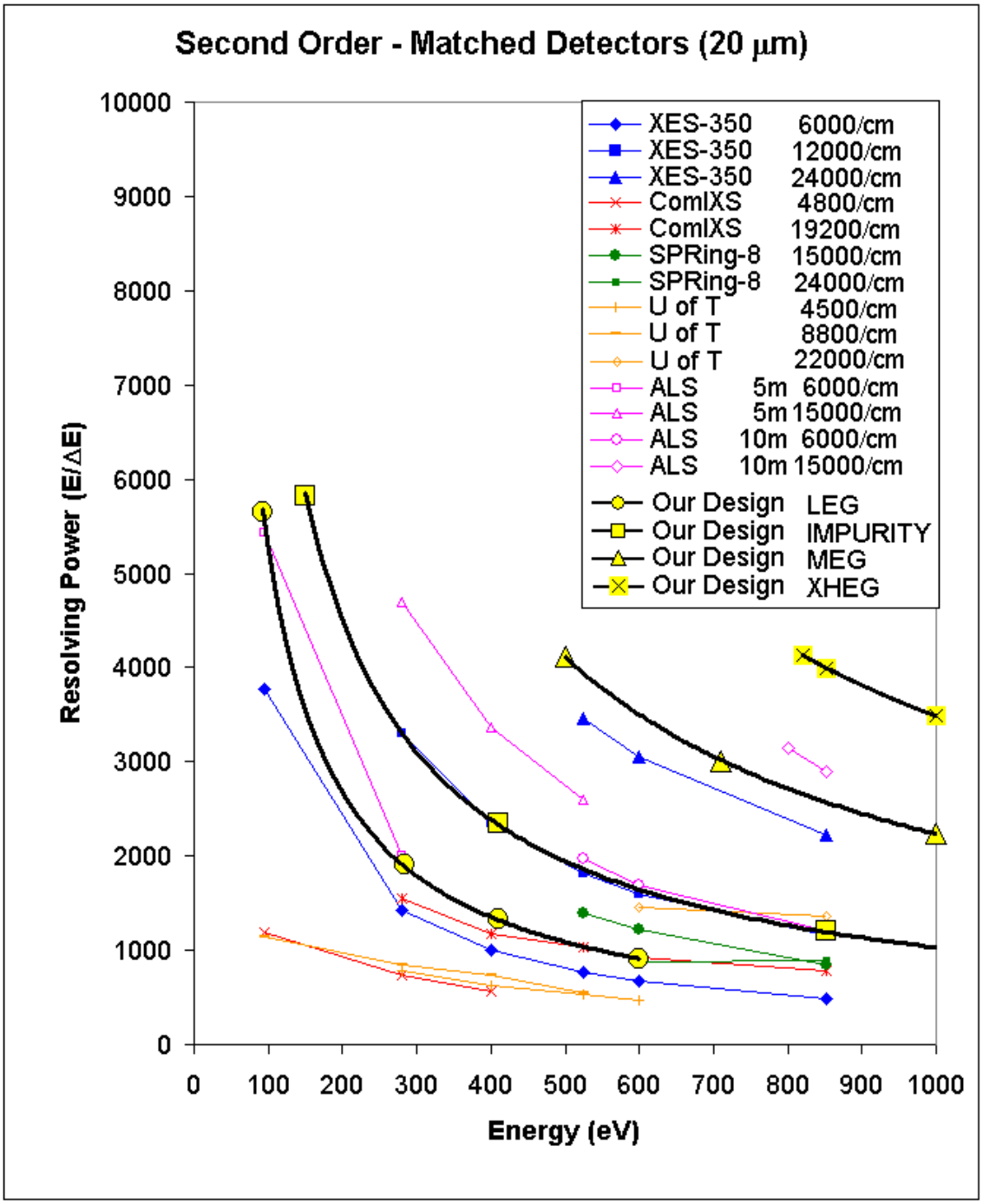

Figure B.2: Comparison of second diffraction order performance of our design to existing spectrometer designs calculated with all detectors having a 20 μm pixel size. The legend specifies the spectrometer, grating (size and/or line density)

Appendix C
Complete Optical Specifications of All Spectrometers

Table C.1: Specifications of the optical designs of all spectrometers

Spectrometer	Grating	Energy Range eV	Radius R, cm	Sample Grating r, cm	Groove density, variation coefficients N_0 (cm^{-1})	b_2	b_3	b_4	Incidence Angle 90° - α	Detector Pixel Size µm
XES-350	G3	18 -	500	16.525	6000	-	-	-	3.25	100µm
	G2	155-1600	500	22.356	12000	-	-	-	2.57	
	G1	250-1350	500	28.19	24000	-	-	-	1.9	
ALS BL 8	VLEG	40-110	500	34.88	6000	-	-	-	4	78µm
	LEG	90-270	500	34.88	15000	-	-	-	4	
	MEG	250-680	1000	34.88	6000	-	-	-	2	
	HEG	400-1000	1000	34.88	15000	-	-	-	2	
ComIXS	Grating 1	20-200	1433	63	4800	29.8	1055	-	2.6	20µm
	Grating 2	100-1200	1433	63	19200	29.8	1069	-	2.6	
SPring-8	Grating 1	250-450	706.7	25	15000	4.22	45.6	1612	3	13µm
	Grating 2	400-900	1124	25	24000	10.7	40.0	8290	2	
Callcott 's UofT	Grating 3	80-300	955	50	4500	12.8	345	9968	2	13µm
	Grating 2	120-480	1430	50	8800	22.0	849	41205	2	
	Grating 1	300-1200	1430	50	22000	22.0	849	40872	3	
Our Design	**Impurity**	**75-750**	**668.7**	**35**	**9000**	**-**	**-**	**-**	**3**	To be Deter-mined (~20µm)
	LEG	**30-300**	**501.7**	**35**	**6000**	**-**	**-**	**-**	**4**	
	MEG	**250-2500**	**1003**	**35**	**12000**	**-**	**-**	**-**	**2**	
	XHEG	**400-4000**	**1003**	**35**	**20000**	**-**	**-**	**-**	**2**	
3rd Order Gratings	**HRMEG**	**~285 - ...**	**1003**	**35**	**18000**	**-**	**-**	**-**	**2**	
	HRHEG	**~525 - ...**	**1146**	**35**	**26000**	**-**	**-**	**-**	**1.75**	

Appendix D

Example Spread Sheets

LEG

r (cm)= 35
R (cm)= 501.7
N (/cm)= 6000
alpha (deg)= 86
Pixel Size (um)= 20

Energy (eV)	r' (cm)	β (°)	E (eV)	Pixel (μm)	Resolving Power	Spectral Window (eV)
			92.10	231.00		
			92.20	536.00		
92	72.60	81.68	92.03082		2986	9.1
			200.20	62.00		
			200.40	231.00		
200	55.59	83.64	200.15030		1332	32.7
			285.30	31.00		
			285.60	171.00		
285	50.34	84.24	285.27643		1032	59.2
			293.30	25.00		
			293.60	157.00		
293	49.99	84.28	293.28864		1016	62.8
			410.70	49.00		
			411.40	216.00		
410	46.21	84.72	410.57844		710	115.9

Figure D.1: Example data from spread sheets used for calculation and interpolation of focal curves for ray-tracing, resolving power and spectral windows sizes.

IMPURITY

r (cm)= 35
R (cm)= 668.8
N (/cm)= 9000
alpha (deg)= 87
Pixel Size (um)= 20

Energy (eV)	r' (cm)	β (°)	E (eV)	Pixel (μm)	Resolving Power	Spectral Window (eV)
			92.05	175.00		
			92.10	430.00		
92	109.52	80.57	92.01961		4693	5.4
			180.40	601.00		
			180.80	1282.00		
180	82.13	82.95	180.05874		3066	16.2
			285.30	132.00		
			285.60	382.00		
285	68.67	84.11	285.16560		1722	33.2
			410.50	95.00		
			411.00	322.00		
410	60.44	84.81	410.33480		1226	60.9
			711.00	25.00		
			712.00	205.00		
710	51.26	85.60	710.97222		731	153.6

Figure D.1 ***(cont.)*****:** Example data from spread sheets used for calculation and interpolation of focal curves for ray-tracing, resolving power and spectral windows sizes.

MEG

r (cm)= 35
R (cm)= 1002.9
N (/cm)= 12000
alpha (deg)= 88
Pixel Size (um)= 20

Energy (eV)	r' (cm)	β (°)	E (eV)	Pixel (μm)	Resolving Power	Spectral Window (eV)
			92.02	125.50		
			92.04	318.50		
92	182.96	79.49	92.00907		10147	2.9
			285.10	57.50		
			285.20	229.50		
285	108.13	83.81	285.07820		3646	16.1
			410.20	57.00		
			410.40	253.00		
410	92.24	84.72	410.16224		2528	28.2
			710.50	41.00		
			711.00	241.00		
710	73.71	85.78	710.44750		1588	69.1

Figure D.1 ***(cont.)*****:** Example data from spread sheets used for calculation and interpolation of focal curves for ray-tracing, resolving power and spectral windows sizes.

XHEG

r (cm)= 35
R (cm)= 1002.9
N (/cm)= 20000
alpha (deg)= 88
Pixel Size (um)= 20

Energy (eV)	r' (cm)	β (°)	E (eV)	Pixel (μm)	Resolving Power	Spectral Window (eV)
			92.01	72.00		
			92.02	199.00		
92	233.84	76.52	92.00591		15580	2.2
			285.10	134.00		
			285.20	360.00		
285	136.53	82.18	285.04956		5752	12.2
			410.20	148.00		
			410.40	408.00		
410	115.53	83.38	410.10154		4039	21.3
			457.30	213.00		
			457.60	538.00		
457	110.02	83.70	457.12185		3752	25.5
			710.30	34.00		
			710.60	194.00		
710	90.74	84.81	710.27375		2595	51.8

Figure D.1 ***(cont.)*****:** Example data from spread sheets used for calculation and interpolation of focal curves for ray-tracing, resolving power and spectral windows sizes.

HR MEG

r = 35
R= 1002.9
n= 18000
alpha= 88
Pixel Size = 20
Varied Size= 20

Energy (eV)	r' (cm)	β (°)	E (eV)	Pixel (μm)	Resolve	Spectral Window (eV)
			285.05	133.00		
			285.10	323.00		
285	218.86	77.39	285.02026		14066	7.3
			410.10	150.00		
			410.20	367.00		
410	183.81	79.44	410.04009		10227	12.7
			525.10	75.00		
			525.20	227.00		
525	163.40	80.62	525.06382		8228	18.2
			710.20	101.00		
			710.40	289.00		
710	141.75	81.87	710.11383		6238	29.4
			852.20	49.00		
			852.40	192.00		
852	130.24	82.54	852.15944		5345	38.7

Figure D.1 ***(cont.)*****:** Example data from spread sheets used for calculation and interpolation of focal curves for ray-tracing, resolving power and spectral windows sizes.

HR HEG

r = 35
R= 1146.1
n= 26000
alpha= 88.25
Pixel Size = 20
Varied Size= 20

Energy (eV)	r' (cm)	β (°)	E (eV)	Pixel (μm)	Resolve	Spectral Window (eV)
			285.05	214.00		
			285.10	479.00		
285	298.03	74.93	285.01340		21276	5.2
			410.10	247.00		
			410.20	549.00		
410	249.87	77.41	410.02483		16510	9.2
			525.10	148.00		
			525.20	355.00		
525	221.70	78.85	525.03816		13757	13.4
			710.20	193.00		
			710.40	455.00		
710	191.70	80.37	710.06794		10452	21.1
			852.20	122.00		
			852.40	320.00		
852	175.68	81.18	852.09697		8787	27.9

Figure D.1 ***(cont.)*****:** Example data from spread sheets used for calculation and interpolation of focal curves for ray-tracing, resolving power and spectral windows sizes.

References

[1] A Hunt, D Muir, and A Moewes. Studying 4d4f transitions in er using resonant inelastic scattering. *Journal of Electron Spectroscopy and Related Phenomena*, 144147:573576, March 2005.

[2] Center of x-ray optics. (www-cxro.lbl.gov/optical_constants/), May 2006.

[3] A Michette. *Optical Systems for Soft X-rays*, chapter 2. Plenum, New York, 1986.

[4] S Singh. Diffraction gratings: aberrations and applications. *Optics And Laser Technology*, 31(3):195 – 218, 1999.

[5] M Burton. Unsw astrophysics postgraduate course. www.phys.unsw.edu.au/~mgb/pg_mod3_lec1.html, May 2006.

[6] J Underwood, editor. *Image properties and aberrations of spherical optics and nonspherical optics*, volume 31. Experimental Methods in the Physical Sciences, 1998.

[7] GR Fowles. *Introduction to Modern Optics*. Dover Publications, Inc, New York, 1989.

[8] A Thompson, D Vaughan, et al. X-ray data booklet. Lawrence Berkeley National Laboratory, 2001. 2nd Edition.

[9] C Welnak, GJ Chen, and F Cerrina. Shadow - a synchrotron-radiation and x-ray optics simulation tool. *Nuclear Instruments And Methods In Physics Research Section A*, 347(1-3):344 – 347, 1994.

[10] JH Halton. A retrospective and prospective survey of the monte carlo method. *SIAM Review*, 12(1):1–63, January 1970.

[11] RL Cook. Stochastic sampling in computer-graphics. *ACM TRANSACTIONS ON GRAPHICS*, 5(1):51–72, Jan 1986.

[12] E Hechy. *Optics*. Addison-Wesley Publishing Co, Reading, Ma, 1988.

[13] G Reichardt and Franz Schäfers. Laminar versus trapezoidial grating profiles: Afm-measurements and efficiency simulations. *Proceedings of SPIE*, 3150:121–129, November 1997.

[14] W Peatman. *Gratings, Mirrors and Slits*, chapter 3. Gordon and Breach Science, Australia, 1997.

[15] T Harada and T Kita. Mechanically ruled aberration-corrected concave gratings. *Applied Optics*, 19(23):3987 – 3993, 1980.

[16] WR Mckinney. Varied line-space gratings and applications. *Review Of Scientific Instruments*, 63(1):1410 – 1414, 1992.

[17] GammaData Scienta. Soft x-ray emission spectrometer, scienta xes 350. (www.gammadata.se/ULProductFiles/XES350_0412.pdf), September 2005. Product Brochure.

[18] JJ Jia, TA Callcott, et al. First experimental results from ibm/tenn/tulane/llnl/lbl undulator beamline at the advanced light-source. *Review Of Scientific Instruments*, 66(2):1394 – 1397, 1995.

[19] High resolution and flux for materialsand surface science - beamline 8.0.1. (www-als.lbl.gov/als/als_users_bl/8.0.1-Overview.pdf), September 2005. User Overview.

[20] D Cocco, M Matteucci, et al. Comixs: A compact inelastic x-ray spectrometer. unpublished, personal communication. See Also: www.elettra.trieste.it, 2004.

[21] Bl 8.2: Beamline for advanced dichroism (bach). (www.elettra.trieste.it/experiments/beamlines/docs/bach.pdf), September 2005. Beamline Overview.

[22] M Zangrando, M Finazzi, D Cocco, et al. Bach, the beamline for advanced dichroic and scattering experiments at elettra. *Review Of Scientific Instruments*, 72(2):1313 – 1319, 2001.

[23] Spring-8 bl27su evaluation report. (www.spring8.or.jp/e/user_info/bl_review /FY2003/BL27SU.pdf), September 2005.

[24] T Callcott. Properties of the university of tennessee vls spectrometer. Personal Communication, 2005.

[25] O Fuchs, L Weinhardt, and C Heske. Design of a soft x-ray emission spectrograph for the study of biologically relevant molecules. Personal Communication, 2005.

[26] R Reininger. Comments on the soft x-ray spectrometer for the reixs beamline. Scientific Answers and Solutions, LLC, October 2005.

[27] M Koike and T Namioka. High-resolution grazing-incidence plane grating monochromator for undulator radiation. *Review Of Scientific Instruments*, 66(2):2144–2146, Feb 1995.

[28] CT Chen. Concept and design procedure for cylindrical element monochromators for synchrotron radiation. *Nuclear Instruments & Methods In Physics Research Section A*, 256(3):595–604, May 1987.

[29] K Heidemann. Diffraction efficiency resolving power of xuv spectrometer gratings - personal communication. Carl Zeiss Optronics GmbH, April 2006.

[30] K Stevenson. Personal communication. Sales Associate, Gratings - Newport Corp, February 2006.

[31] E Bach. Personal communication. Bach Research Corp, April 2006.

[32] T Harada, T Kita, M Itou, and H Taira. Mechanically ruled diffraction gratings for synchrotron radiation. *Nuclear Instruments and Methods in Physics Research*, A246:272–277, 1986.

[33] A Seifert. Personal communication. Manager Optical Technology, Carl Zeiss Laser Optics GmbH, Janurary 2006.

[34] J Nordgren, G Bray, et al. Soft x-ray emision spectroscopy using monochromatized synchrotron radiation. *Review Of Scientific Instruments*, 60(7):1690, 1696 1989.

[35] TA Callcott, KL Tsang, CH Zhang, DL Ederer, and ET Arkawa. High-efficiency soft x-ray emission spectrometer for use with synchrotron radiation excitation. *Review Of Scientific Instruments*, 57(11):2680–2690, November 1986.

[36] BJ Brown and IJ Wilson. Holographic grating aberration correction for a rowland circle mount. *OPTICA ACTA*, 28(12):1587–1599, 1981.

[37] DL Ederer and ET Arakawa. Area detectors for x-ray spectroscopy. *Nuclear Instruments and Methods in Physics Research*, 266:578–585, April 1988.

[38] Princeton Instruments. High performance x-ray imaging solutions. Product Brochure, 2004.

[39] Building a charge-coupled device. www.microscopy.fsu.edu/primer/digitalimaging, May 2006.

[40] Andor Technology. *do* series product brochures. www.andor.com, Sept 2005.

[41] Quantar Technology. 3300/2400 series product brochures. www.quantar.com, January 2006.

[42] MR Mellon. Private communication. Quantar Technologies, January 2006.

[43] CH Skinner and JL Schwob. Charge-coupled-device detection of soft x-rays for grazing-incidence spectrometers. *Applied Optics*, 35(22):4321–4324, August 1996.

[44] Micos vacuum motion control catalog. www.micos.wws, January 2006.